RHEOLOGICAL MODELS FOR TISSUE RELAXATION AND FLUIDISATION

Nina Asadipour

Doctoral Thesis
Advisor: Jose Javier Muñoz Romero
Barcelona, February 2016

Departament de Matemàtiques
Programa de Doctorat en Matemàtica Aplicada

UNIVERSITAT POLITÈCNICA DE CATALUNYA
BARCELONATECH
Escola de Doctorat

Curs acadèmic: 2015-2016

Acta de qualificació de tesi doctoral

Nom i cognoms
Nina Asadipour

Programa de doctorat
MATEMÀTICA APLICADA

Unitat estructural responsable del programa

Resolució del Tribunal

Reunit el Tribunal designat a l'efecte, el doctorand / la doctoranda exposa el tema de la seva tesi doctoral titulada

_____

_____.

Acabada la lectura i després de donar resposta a les qüestions formulades pels membres titulars del tribunal, aquest atorga la qualificació:

☐ NO APTE ☐ APROVAT ☐ NOTABLE ☐ EXCEL·LENT

(Nom, cognoms i signatura) President/a	(Nom, cognoms i signatura) Secretari/ària	
(Nom, cognoms i signatura) Vocal	(Nom, cognoms i signatura) Vocal	(Nom, cognoms i signatura) Vocal

_____, _____ d'/de _____ de _____

El resultat de l'escrutini dels vots emesos pels membres titulars del tribunal, efectuat per l'Escola de Doctorat, a instància de la Comissió de Doctorat de la UPC, atorga la MENCIÓ CUM LAUDE:

☐ SÍ ☐ NO

(Nom, cognoms i signatura) President de la Comissió Permanent de l'Escola de Doctorat	(Nom, cognoms i signatura) Secretari de la Comissió Permanent de l'Escola de Doctorat

Barcelona, _____ d'/de _____ de _____

Abstract

Soft active tissues exhibit poroelastic behaviours, softening, hardening, and reversible fluidisation. The result of these non-linear behaviour is due to multiple processes taking part at different scales: active protein motors that actuate at the polymeric structure of the cell, (de)polymerisation and remodelling of the cytoskeleton, changes in the cytoplasm volume and cell-cell connectivity changes that take place at the tissue level. The main goal of the present work is to understand the mechanical properties of a soft tissue when undergoing fluidisation and stress relaxation. Toward this goal, we develop mathematical theory and simulation methods that reproduce the experimental observations.

We present a cell-centred model for the simulation of multicellular soft tissues that takes into account the underlying active process at the cytoskeletal level, and allows for active and passive cell-cell reorganisation and intercalation. In the cell centred model, each cell is treated as a discrete entity and adjacent cell centres are connected by bar elements holding the rheological properties of cell-cell interactions. Cell-cell connectivity is determined with Delaunay triangulation of the cell-centres (nuclei). We use Voronoi tessellation and barycentric tessellation in order to represent the cell domains.

We develop a viscoelastic bar element that can handle multiple rheological laws with non-linear elastic and non-linear viscous material models. The bar element is built by joining in series an elastic and viscous bar, constraining the middle node position to the bar axis with a reduction method, and statically condensing the internal degrees of freedom. Also, we develop a new rheological model based on dynamical changes of the resting length which mimics the viscoelastic response.

It has been experimentally observed that cells exhibit a fluidisation process when subjected to a transient stretch, with an eventual recovery of the mechanical properties upon removal of the applied deformation. This fluidisation process is characterised by a decrease of the storage modulus and an increase of the phase angle. We propose a rheological model which is able to reproduce this combined mechanical response. The model is described in the context of continua and adapted to a cell-centred particle system that simulates the cell-cell interaction. Mechanical equilibrium is coupled with two evolution laws: (i) one for the reference configuration, and (ii) another for the porosity or polymer density. The first

law depends on the actual elastic strain of the tissue, while the second assumes different remodelling rates during porosity increase and decrease. The theory is implemented on the particle based model and tested on a stretching numerical simulation, which agrees with the experimental measurements for different stretching magnitudes.

The rheological law is also applied to simulate the stress relaxation that suspended monolayers undergo when subjected to a constant stretch. The numerical model is here applied on in multiple branches, so that the response with different characteristic times is reproduced.

By using Delaunay triangulations and Voronoi tessellations, the model presented in this thesis also opens the possibility to test different combined rheological laws in cytoskeletal and cortical regions of cellular networks.

Acknowledgements

I would like to express my special appreciation and thanks to my advisor Professor Jose Muñoz, for the continuous support of my Ph.D study and research, for his patience, motivation, enthusiasm, and immense knowledge, you have been a tremendous mentor for me. Your advice on both research as well as on my career have been priceless.

I would especially like to thank the faculty of Departament de Matemàtica Aplicada III. I am truly thankful for the assistance of administrative staff, in particular Imma Rius, Anna Fabregas and the technical support of David Ortin.

During this research work, I have collaborated with many colleagues for whom I have sincere regards. I am indebted to all my colleagues in the group of LaCàN at Barcelona, specially Payman Mosaffa. A very special thanks to Nargess khalilgharibi, it has been a great experience to work with her and share her knowledge in many interesting technical discussions, and also her sincere friendship.

During these years I have shared great time with very important people, my outdoor friends, Golnaz, Negin and Behshid.

A special thanks to my family, especially my sister, Moona Asadipour , and her husband, Tom Creemers for supporting and encouraging me to pursue this degree. Words cannot express how grateful I am to my father for all of the sacrifices that he has made on my behalf. Finally, but by no means least, thanks to Enrique Garcia for almost unbelievable support. He has been a constant source of strength and inspiration. They are the most important people in my world and I dedicate this thesis to them.

I want to thank the support of the Ministry of Economy and Competitiveness through grant No. DPI2013-44727R, and the support of Universitat Politècnica de Catalunya (UPC) and the Consorci Escola Industrial de Barcelona (CEIB) through the grant UPC-FPI 2012, and the European Research Council under the European Community's 7th Framework Programme (FP7/2007-2013)/ERC Grant Agreement No.240487 and Generalitat de Catalunya through the grant No.2014-SGR-1471.

Contents

List of Figures

List of Tables

Nomenclature

Ω	Configuration domain.
α, β	Material properties.
$\boldsymbol{\gamma}$	Remodelling rate tensor.
δ	Phase angle.
η	Viscosity.
γ	Remodelling rate parameter.
λ	Internal variable.
ω	Angular frequency.
σ	Stress.
σ^e, σ^v	Elastic and viscous stresses.
θ	Average time step parameter.
ε^e, ε^v	Elastic and viscous strain.
k	Material stiffness.
Δt	Time step.
$\boldsymbol{C}^n$	Configuration of the geometry at time-step t^n.
$\boldsymbol{p}$	Set of material parameters.
$\boldsymbol{t}^i$	Elastic bar residual at node i.
$\boldsymbol{t}^i_{ij}$	Force at node i of bar between nodes i and j.
$\boldsymbol{T}^n$	Connectivity matrix at time-step t^n.
$\boldsymbol{X}^n$	Nodal positions at time-step t^n.
$\boldsymbol{E}^e$	Green-Lagrange elastic strain tensor.
$\boldsymbol{F}$	Total deformation gradient.

$\boldsymbol{F}^a$	Active deformation gradient.
$\boldsymbol{F}^e$	Elastic deformation gradient.
$\mathbf{L}$	Active length tensor.
$\boldsymbol{C}$	Cauchy Green tensor.
$\boldsymbol{S}$	Second Piola-Kirchhoff stress tensor.
$\boldsymbol{x}_i$	Current position of node i.
c_1, c_2, c_3	Material constant.
D	Damage parameter.
G'	Storage modulus.
G''	Loss modulus.
J^a	Active deformation.
J_0^a	Initial active configuration.
J^e	Elastic deformation.
L	Resting length.
l	Current length.
l^e, l^v	Elastic and viscous current length.
L_0	Initial length.
P	Polymer porosity.
R	Radius of the circumcircle (circumradius).
r	In-radius.
t	Time.
tol_R	Tolerance for filtering skinny triangles on the boundaries.
$U^e(\boldsymbol{C})$	Strain energy.
U_{ij}	Elastic potential energy between nodes i and j.

Chapter 1

Introduction

1.1 Motivation and background

Cells, the smallest units of life which can exist on its own, are dynamic and ever changing entities composed of numerous components with distinct mechanical, chemical and biological properties. They are active materials that can respond to external mechanical stimuli and interact with their surrounding through cytoskeletal re-organization and force generation. They perform a variety of biological functions many of which directly depend on their shape and structural stiffness. They are able to detect substrate mechanical properties by actively generating contractile forces and use this information to migrate and proliferate [Trepat et al., 2009]. They are stabilized by the cytoskeleton, a highly active contractile polymeric network which is able to (de)polymerise and reinforce [Gardel et al., 2004].

This cytoskeletal activity renders cells with a complex rheological response, exhibiting stiffening [Gardel et al., 2004, Storm et al., 2005, Fernández and Ott, 2008] and softening [Wolff et al., 2012]. It has been observed that upon stretching, the fluid contribution of the response increases while the solid part decreases, which is measured by a reduction of the phase angle between the storage and loss modulus. It is thus considered that cells fluidise, either individually [Krishnan et al., 2009] or when forming a soft tissue [Trepat et al., 2007]. Furthermore, recent experimental evidence suggests that cell rheology can be described by a poroelastic model, in which the cytoplasm is treated as a biphasic material consisting of a porous elastic solid meshwork (cytoskeleton, organelles, macromolecules) bathed in an interstitial fluid (cytosol) [Moeendarbary et al., 2013].

The study of cell dynamics is fundamental for understanding biological phenomena such as embryology, tissue repair, and most importantly, tumors. Up to a decade ago, biochemistry and genetics have been the main discipline employed to study such processes, with undeniable success. There is, however, growing awareness that mechanics also plays a crucial role in these dynamical processes. Since the classical work of Young [Young, 1959] and later Eaves [Eaves, 1973],

the mechanical effects on tumors have been widely studied. For example, in the key work of Helmlinger [Helmlinger et al., 1997] experimental evidence was provided to support the idea that the growth of multicellular tumor is controlled by pressure. More surprisingly, their findings are demonstrated regardless of host species, tissue of origin, or differentiation state. These results motivate the study of single cell mechanics, multiple cell mechanical interactions, and their effect on the global dynamics of growing ensembles.

1.1.1 Mechanical response of cells

Recently, it has become well established that critical insights into diverse cellular processes can be gained by understanding the role of mechanical force. The mechanical phenomena are critical to the proper functioning of several basic cell processes and that mechanical loads can serve as extracellular signals that regulate cell function [Vogel and Sheetz, 2006, Brugués et al., 2014]. For instance, the health of several tissues, particularly tissues of the skeleton (bone and cartilage) and of the cardiovascular system (the heart and arteries), is heavily dependent on mechanical loading, which in turn comes from physical activity and the environment [Malandrino et al., 2011]. There is therefore a need to predict how forces are transmitted throughout the cell, as well as the way in which local forces produce conformational change. To the extent that a theoretical model can capture the stress or strain distribution within the cell, it can help us to relate the biological influences of various types of force application, while at the same time, guide us to a better understanding of cell mechanics.

Cells are known to exhibit complex constitutive behaviour, in which stress may depend on both strain and strain rate as well as strain history [Fung, 1993]. These characteristics suggest a behaviour that combines the properties of elastic solids and viscous fluids, and therefore cells are generally known to respond in a viscoelastic manner to mechanical perturbations [Jamison et al., 1968]. Rheological models like Kelvin-voigt and Maxwell have traditionally been the popular choice to characterise the viscoelastic behaviour and properties of soft tissues. In Kelvin-Voigt model (Figure 1.1, a), a spring and a dashpot are connected in parallel where the stress is additive and the strain is equal in each element. In Maxwell model (Figure 1.1, b), a spring and a dashpot are connected in series, the strain is additive and the stress is equal in each element. The former is best suited for modelling creep in a stress controlled test, while the latter is able to reproduce stress relaxation in a displacement controlled test. Standard linear solid model (Figure 1.1, c) is a combination of the two models, and gathers the advantages of both. It is therefore better suited for fitting general viscoelastic materials.

The characterization of the viscoelastic response of materials in one dimension has been well studied [Findley et al., 1989, Belytschko et al., 2000]. Its extension to multiple dimensions and its finite element implementations in the

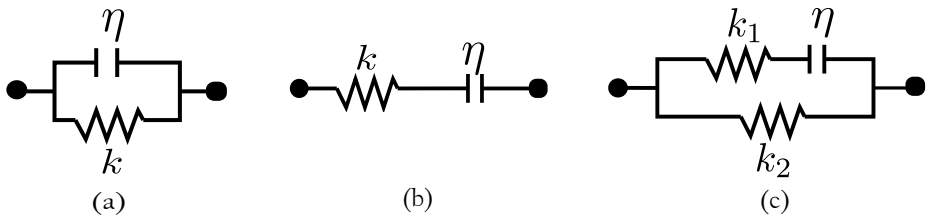

Figure 1.1: Representation of (a) Kelvin-Voigt model, (b) Maxwell model, (c) Standard linear solid model.

linear regime were originally developed more than thirty years ago [Zienkiewicz, 1975, Hughes and Taylor, 1978]. However, when extending these formulations to finite elasticity, some internal variables and evolution laws must be hypothesised and numerically solved [de Buhan and Frey, 2011, Holzapfel, 2000, Simo, 1987]. Such constitutive models may be written as a function of the principal stretches [Bonet, 2001], or in materials with fibres, in terms of the preferred material directions [Holzapfel and Gasser, 2001]. In these formulations, the elastic and viscous stresses are numerically solved in a robust monolithic manner by using linear viscoelastic constitutive models. Although this procedure may be advantageous in a finite element context, it makes the resolution of problems with more complex non-linearities highly dependent on the rheological law at hand.

In this thesis, Maxwell and other rheological laws are implemented on one dimensional bars which are able to rotate. This allows us to simulate general viscoelastic behaviours of cells in a simple manner. Also, an alternative model based on an extension of a Maxwell-like law that uses an adaptive resting length will be developed, which mimics the apparent measured viscosity [Muñoz and Albo, 2013].

1.1.2 Modelling in tissue biology

Cell modelling has enjoyed a long history in applied mathematics and biology. Up to now, several approaches have been investigated to understand the mechanics of cell structure. These approaches developed so far for the analysis of multicellular systems and single cells can be classified into continuum based models [Muñoz et al., 2007, Ramasubramanian and Taber, 2008] and discrete models [Macklin et al., 2010].

Continuum approaches treat the tissue as comprising materials with continuous material properties and deformations. From experimental observations, the appropriate constitutive material models and the associated parameters are then derived. In such models the tissue is assumed to be uniform in terms of cell density, and without gaps. While these approaches allow studying a complete tissue, they can not provide enough details of the mechanical effects at the micro scale, since cell units are smeared out and are not represented.

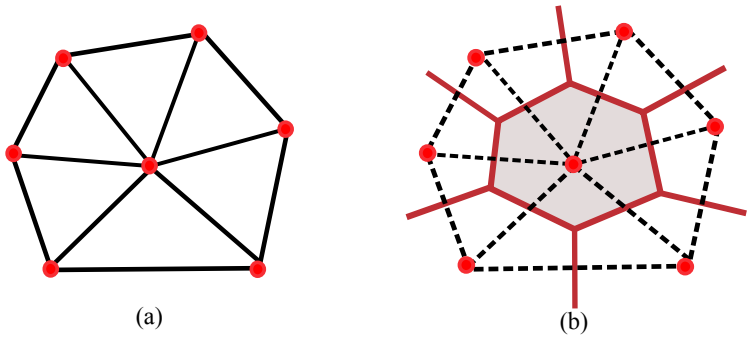

Figure 1.2: A schematic view of the cell-centred model: (a) The Delaunay triangulation method of defining connectivities, spheres represent cell nuclei and the lines cell-cell contact. (b) The Voronoi tessellation corresponding to the Delaunay triangulation in (a) represents the boundary of the cell.

Discrete models may be in turn subdivided into vertex models [Honda et al., 2004, Nagai and Honda, 2001, Okuda et al., 2013, Spahn and Reuter, 2013], Potts models [Merks and Glazier, 2005], cell-centred models [Drasdo and Holme, 2005, Mirams et al., 2013, Muñoz et al., 2013, Pathmanathan et al., 2009], or subcellular models [Escribano et al., 2014], where particles do not represent cells, but material points of the cell. These models treat cells as discontinuous matter *ab initio*. Today, discrete cell modelling has advanced to study a broad swath of cancer biology, spanning carcinogenesis, tumor growth, invasion, and angiogenesis [Macklin et al., 2010].

1.2 Objectives

In this thesis we aim to simulate the cellular mechanical behaviour of tissues when undergoing fluidisation and stress relaxation process. We will allow cells to adopt a large variety of shapes in response to mechanical interactions. Motivated by the need to represent hundreds or even thousands of cells, and the self-organisation of the tissue when undergoing topological changes, we resort to the cell-centred model (Figure 1.2). Our choice aims to simplify the definition of the two and three dimensional geometry when cell neighbours are dynamically changing, a task that is significantly simpler for cell-centred models. This model aims to reconstruct tissue dynamics from the collective behaviour of the individual cells where, the location of a cell is given by a single point, its centre, and the total force on any cell is a function of the set of cell centres. In such models, there are two components that need to be specified:

(i) A definition of cell-cell connectivity, which, given a set of cell-centre locations, defines which cells are in contact. We resort to Delaunay triangulation (Figure 1.2, a), which involves meshing the domain with triangles and using the cell centres to define cell-cell connectivity while cell shapes are determined by a

Voronoi tessellation (Figure 1.2, b) or other suitable tessellation.

(ii) A definition of the force between two cells in contact. For cell-centred models, the cell-cell interaction force is a function of (at least) the distance between the cell centres, and nearly always acts in the direction of the vector connecting the two cell centres. The force law can be different depending on whether the cells are in compression or in tension. There are a wide range of force laws that have been used in the literature, ranging from simple linear laws [Osborne et al., 2010], to much more complex non-linear models [Fernández et al., 2006]. In this thesis we adopt generalised Maxwell models and develop an equivalent rheological model based on an evolution of the resting length. We further extend this model with a porous-like variable in order to simulate tissue fluidisation.

1.3 Outline of the thesis

The structure of the thesis is as follows:

In Chapter 2, a cell-centred model for the simulation of multicellular soft tissues is presented. Section 2.1 depicts a brief introduction in dynamic topology of cell structures. Sections 2.2, 2.3, 2.4 and 2.5 describe the ingredients of the computational model: the bar elements being employed, the equations to be solved and the definition of the cell-cell connectivity and cell boundary. Section 2.6 displays an application of the methods described in the previous sections to study real tissue geometry. Parts of Sections 2.2, 2.3, 2.4 and 2.5 have been published as a journal paper in *Computational Particle Mechanics* [Mosaffa et al., 2015].

In Chapter 3, Maxwell and active rheological models are presented. The classical solution of the Maxwell model as well as the Maxwell element formulation are introduced in Section 3.2. In this section, by developing a new representation of the bar element, the corresponding stiffness matrices and elemental residuals are obtained through null-space projection and static condensation. The linear and non-linear constitutive laws for elastic and viscous materials are studied also in Section 3.2. Parts of Sections 3.2 and 3.5 have been published as a journal paper in *Mechanics Research Communications* [Muñoz et al., 2013]. In Section 3.3 an evolution law of the macroscopic remodelling process is presented, which mimics the apparent measured viscosity. This evolution law is able to reproduce the viscoelastic response at small strains. The process of resting length recovery of the active model is given also in Section 3.3. The resting length changes is combined with a purely linear elastic law, and the resulting active model is compared against a linear Maxwell model in Section 3.5.

In Chapter 4, a rheological model based on dynamical changes of the resting

length that exploits the changes in cell porosity is presented. Section 4.1 depicts a brief introduction in rheological models for tissue softening and stiffening. In this chapter we aim to simulate reversible softening that has been experimentally observed in bio-mechanical tests performed on epithelial lung cell monolayers [Trepat et al., 2007]. Section 4.2 describes this experimental work. Section 4.3 presents a continuum model where the evolution law for the resting length regulated by porosity. Also, in this section we introduce an evolution law for the polymer density. The continuum model will be adapted to a particle based model in Section 4.4. Finally, the numerical result of the experimental simulation is presented in Section 4.5. The results of this chapter has been submitted in *Mechanics and Physics of Solids* jornal.

In Chapter 5, we introduce Generalised Maxwell model and Generalised active model in order to simulate the cellular mechanical behaviour when undergoing stress relaxation process. Section 5.1 describes the experimental work done by experimentalists at University College London (UCL), Department of Cell and Developmental Biology, London, United Kingdom, where they report a biphasic behaviour of cells during stress relaxation process. A material fitting methodology is presented in Sections 5.2. We test these rheological models under a constant and an incremental strain in Section 5.3 and 5.4.

Finally in Chapter 6 we summarise the conclusions achieved during the previous chapters and discuss the future work that can be pursued as a consequence of the developments described in this thesis.

Chapter 2

Dynamic topology of cell structures

2.1 Computational model for cell topology

In this chapter we aim to simulate global embryogenetic cell shape changes such as invagination or germ-band extension [Costa et al., 1993]. Motivated by the need to represent thousands of cells (Drosophila fly embryo for instance is formed by around 6000 cells during gastrulation), and the self-organisation of the tissue when undergoing topological changes, we resort to a cell-centred model, where each cell is represented by a particle, and each cell-cell interaction is modelled through a bar element connecting two particles. This element carries all the interactions at the junctions between the cells, and also the internal active and passive forces produced by the cytoskeleton. Since topological changes are commonly observed during embryo development, and may determine the global tissue deformations [Lecuit and Lenne, 2007], the proposed model aims to handle these changes in a robust manner.

2.2 Model definition

We will henceforth consider that the cellular system satisfies the following assumptions:

(a) Cells are packed with no extracellular space in between.

(b) Cell centres are considered as dimensionless points (later mentioned as nodes) which define the location of each cell in space.

(c) Contact between two cells i and j is defined by the presence of a one-dimensional bar element connecting the two cell centres, providing a connected graph as a whole.

(d) The total number of cells (nodes) N is constant.

Assumptions (a)-(c) are considered to simplify the computations, while assumption (d) is consistent with the fact that when cells undergo drastic deformations, no proliferation takes place, that is, the number of cells remains approximately constant [Leptin and Grunewald, 1990].

The configuration of the model at each time-step t^n, denoted by $\boldsymbol{C}^n$, is defined by the nodal position of the N nodes, $\boldsymbol{X}^n = \{\boldsymbol{x}_1^n, \boldsymbol{x}_2^n, ..., \boldsymbol{x}_N^n\}$, and the connectivity between the nodes, indicated by a connectivity matrix, $\boldsymbol{T}^n$ that represent the topology of the N_E^n bars. The two sets of variables, $\boldsymbol{X}^n$ and $\boldsymbol{T}^n$ may vary between time-steps, and are computed from the previous variables $\boldsymbol{C}^n$ according to the following scheme:

1. Compute nodal coordinates $\boldsymbol{X}^{n+1}$ by finding mechanical equilibrium between the particles, while keeping the connectivity $\boldsymbol{T}^n$ constant.

2. Update the connectivities $\boldsymbol{T}^{n+1}$ resorting to a Delaunay triangulation of the new positions $\boldsymbol{X}^{n+1}$.

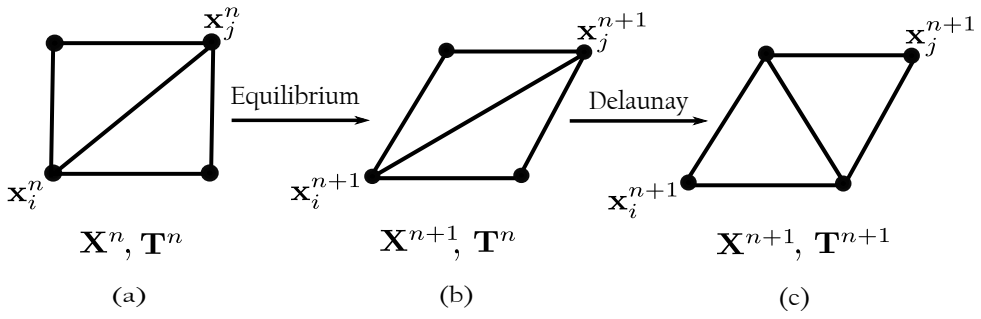

Figure 2.1: A schematic view of Delaunay triangulation for a set of four nodes. (a) Delaunay triangulation at time t^n. (b) Equilibrated positions $\boldsymbol{X}^{n+1}$ using a constant connectivity $\boldsymbol{T}^n$. (c) Delaunay triangulation $\boldsymbol{T}^{n+1}$ associated to positions $\boldsymbol{X}^{n+1}$.

Figure 2.1 shows the two-step update process. Note that according to the scheme above, equilibrium at time t^{n+1} is computed for the connectivity defined at time t^n. The connectivity at $\boldsymbol{T}^n$ may not comply with the definition of the Delaunay triangulation for the new positions $\boldsymbol{X}^{n+1}$, and for this reason the cell-cell contacts are updated, yielding a new connectivity $\boldsymbol{T}^{n+1}$. This staggered update process is employed in order to avoid redefining the connectivity while computing the equilibrated positions, which would lead to a non-smooth problem, and therefore also potential convergence difficulties. We will next describe in detail the two steps: mechanical equilibrium (Section 2.3) and connectivity definition (Section 2.4).

2.3 Mechanical equilibrium

The connectivity matrix $\boldsymbol{T}^n$ at time t^n defines a set of N_E^n elements $E^n = \{1, \ldots, e_{N_E^n}\}$, each one connecting a pair of nodes i and j. In order to ease the notation, we will drop in this section the superscript n. For each element e we have used the following elastic potential U_{ij}:

$$U_{ij} = \frac{1}{2} k \left(\varepsilon_{ij}^e\right)^2, \tag{2.1}$$

with k a material parameter representing the material stiffness, and ε_{ij}^e the scalar elastic strain between nodes i and j, and given by:

$$\varepsilon_{ij}^e = \frac{(l_{ij} - L_{0,ij})}{L_{0,ij}}.$$

Here, $l_{ij} = ||\boldsymbol{x}_i - \boldsymbol{x}_j||$ is the current length between nodes i and j, and $L_{0,ij}$ is the initial length between the two nodes. The scalar elastic force at the two ends of element ij is given by $\sigma^e = \partial U_{ij}/\partial \varepsilon_{ij}^e = k\varepsilon_{ij}^e$, while the elastic vectorial contribution to the bar residual denoted respectively by $\boldsymbol{t}_{ij}^i$ and $\boldsymbol{t}_{ij}^j$ are obtained as,

$$\boldsymbol{t}_{ij}^i = \frac{k}{l_{ij}} \varepsilon_{ij}^e (\boldsymbol{x}_i - \boldsymbol{x}_j) \tag{2.2}$$

$$\boldsymbol{t}_{ij}^j = \frac{k}{l_{ij}} \varepsilon_{ij}^e (\boldsymbol{x}_j - \boldsymbol{x}_i). \tag{2.3}$$

The global equilibrium of the system is computed by assembling at each node all the confluent forces, that is solving the following set of equations:

$$\boldsymbol{t}^i := \sum_{ik \in I_i} \boldsymbol{t}_{ik}^i = \boldsymbol{0}, \quad i = 1, \ldots, N \quad , \tag{2.4}$$

where $I_i \subset E$ denotes the subset of elements connected to node i. We will resort to a Newton-Raphson scheme for finding the solution of the N equations in (2.4).

2.4 Cell-cell connectivity

2.4.1 Connectivity definition

We resort to Delaunay triangulation (D) [Barber et al., 1996] of the set of nodes $\boldsymbol{X}^{n+1}$ obtained from the mechanical equilibrium described in the previous section. This triangulation connects the nodes in such a way that the circumcircle of any triangle does not contain any other node in it, providing triangles with optimal aspect ratio [Barber et al., 1996, Okabe et al., 1992]. Figure 2.2 illustrates a schematic view of this triangulation for a set of four nodes (cell centres).

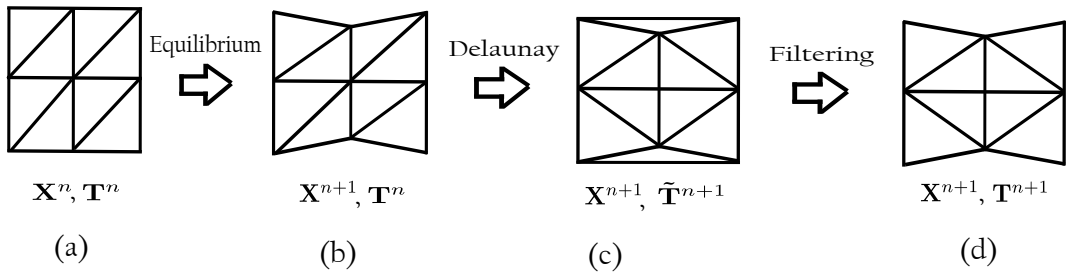

Figure 2.2: Filtering process of Delaunay triangulation: (a) Configuration at time t_n. (b) Nodal positions at time t_{n+1}, in equilibrium while holding the Delaunay triangulation at t_n. (c) Delaunay triangulation updated for the new positions, with unrealistic connectivities on concave edges. (d) Unrealistic connectivities being filtered.

One of the properties of the Delaunay's algorithm is that the union of all the simplexes of the triangulations yields the convex hull of the points. Therefore, a basic Delaunay triangulation $\tilde{\boldsymbol{T}}^{n+1} = D(\boldsymbol{X}^{n+1})$ of the cell centres may invariably lead to distant boundary cells being unrealistically connected, i.e. covering non-convex boundaries (see Figure 2.2c). In order to overcome this problem, those elements with very high aspect ratio are eliminated by defining a filtering process described in the following section.

2.4.2 Filtering of Delaunay triangulation at domain boundaries

The ratio of in-radius, r, to circumradius, R, of each triangle in 2D problem (see Figure 2.3) has been considered as an appropriate criterion to filter undesirable simplexes. Other criteria such as weighted α-shape [Edelsbrunner et al., 1983] could be adopted. We implemented the criteria described here due to its simplicity.

In 2D Euclidean geometry, in-radius, r, of a triangle is the radius of the circle tangential to the sides of the triangle. Given a, b and c the lengths of the sides, the in-radius may be expressed as [Weisstein, 2016a],

$$r = \frac{1}{2}\sqrt{\frac{(b+c-a)(c+a-b)(a+b-c)}{a+b+c}}. \tag{2.5}$$

The circumradius R of a triangle is the minimum radius of the circle in which the triangle can be inscribed. Given the above lengths of the sides of the triangle, the circumradius R reads [Weisstein, 2016b],

$$R = \frac{abc}{\sqrt{(a+b+c)(b+c-a)(c+a-b)(a+b-c)}}. \tag{2.6}$$

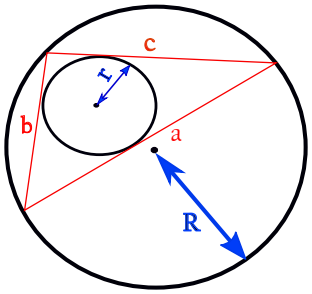

Figure 2.3: A schematic view of the in-circle and circumcircle with their radii r and R, respectively.

The ratio in-radius/circumradius, is a criterion of a triangle aspect ratio or flatness, i.e. the lower the ratio, the flatter the triangle,

$$\frac{r}{R} = \frac{1}{2}\frac{(b+c-a)(c+a-b)(a+b-c)}{abc\sqrt{a+b+c}}. \tag{2.7}$$

In our case, we have used a tolerance $tol_R = 0.2$ and imposed that wherever $\frac{r}{R} < tol_R$, the triangle is removed (see Figure 2.2d).

2.5 Cell boundary

In most circumstances, we will represent the cell boundaries by employing a Voronoi tessellation. Due to some disadvantages that will be commented later, we will also use a tessellation using the barycentre of the triangle elements. We will explain both types of tessellations later.

2.5.1 Voronoi tessellation

To represent the cells boundaries, we resort in most of the cases to standard Voronoi tessellation algorithm of the set of nodes $\boldsymbol{X}^{n+1}$: each Voronoi face is perpendicular to the connecting line of the Delaunay triangulation, and splits in half this line [Barber et al., 1996].

However, when it comes to constructing the boundaries associated with the cells at the boundary of the cell aggregate, Voronoi faces (edges in 2D) form unbounded regions closing at infinity. In order to obtain a bounded cell region for each node, a set of off-set nodes were added to the original set of nodes at the boundary of the filtered Delaunay triangulation. Each edge at the boundary was duplicated by adding nodes at a constant off-set distance.

The steps followed to form the Voronoi tessellation are:

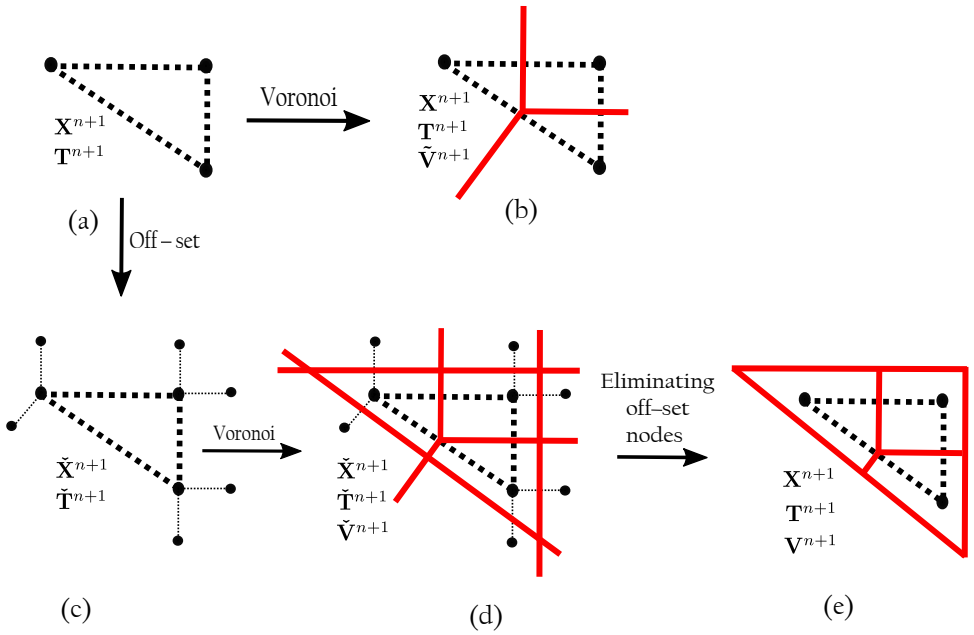

Figure 2.4: Voronoi tessellation: (a) Delaunay triangulation of original set of nodes, (b) open Voronoi tessellation, (c) setting up off-set nodes, (d) Voronoi vertices set on original nodes and off-set nodes and (e) closed Voronoi boundaries for surface nodes after eliminating off-set nodes followed by removal of Voronoi vertices at infinity.

1. Form layer of off-set nodes $\boldsymbol{x}^{\mu}_{off-set}$. The external normal $\boldsymbol{n}^{\mu}$ to each boundary μ is computed, and the new set of nodes $\boldsymbol{x}^{\mu}_{off-set}$ is built according to,

$$\boldsymbol{x}^{\mu}_{off-set} = \boldsymbol{x}^{\mu} + \epsilon \boldsymbol{n}^{\mu}. \tag{2.8}$$

   The new set of nodes is denoted by $\check{\boldsymbol{T}}^{n+1}$, which includes $\boldsymbol{X}^{n+1}$ and the nodes of the off-set layer $\boldsymbol{x}^{\mu}_{off-set}$ (see Figure 2.4c). In our numerical results we have used the value $\epsilon = 1$, which gives a reasonable cell shape for the cells at the boundaries in our examples, where the cells have an averaged siza of a unit. We note that, in general, the choice of this parameter should be made dependent on the actual size of the cell, and other values such as one half of the cell-to-cell distance. In our current implementation, where the Voronoi vertices are not included in the mechanical equilibrium, the value of ϵ does not affect the deformed configurations, but just the aspect of the cell region.

2. Build a new Delaunay triangulation from $\check{\boldsymbol{X}}^{n+1}$, *i.e.* $\check{\boldsymbol{T}}^{n+1} = D(\check{\boldsymbol{X}}^{n+1})$ (see Figure 2.4c).

3. Build Voronoi tessellation of $\check{\boldsymbol{T}}^{n+1}$, that is $\check{\boldsymbol{V}}^{n+1} = Voronoi(\check{\boldsymbol{T}}^{n+1})$ (see Figure 2.4d).

4. Remove Voronoi vertices connected to vertex at infinity (see Figure 2.4e) and remove nodes of the off-set layer.

In summary, the Voronoi tessellation was constructed taking into account the original and the additional off-set nodes, ensuring the formation of bounded regions for the original nodes of the monolayer. Figure 2.4a illustrates a schematic view of a set of three nodes primarily connected by a Delaunay triangulation. Figure 2.4b shows the unbounded regions created by directly applying a Voronoi tessellation. Figure 2.4c indicates the off-set nodes with smaller circles, while Figure 2.4d shows the Voronoi regions formed by this extended set of nodes, which after removing the unbounded regions and the off-set nodes results in the final Voronoi regions of the cells for the original set of nodes (Figure 2.4e). The off-set nodes are finally removed. In this thesis the construction of the Voronoi tessellation is used only for the visualisation purposes.

We note that we could have alternatively applied the Voronoi tesselation on the internal nodes, which would guarantee no unbounded Voronoi regions. This alternative procedure would avoid creating the off-set nodes, but with a subset of cells being created, leaving the external nodes without associated tessellation.

2.5.2 Barycentric tessellation

Algorithm for the Voronoi tessellation are well developed and available. However, after stretching the tissue, the cell-cell connectivity T^n does not necessarily obey the rules of the Delaunay triangulation for the deformed positions x^{n+1}. Therefore, the Voronoi tessellation may lead to unrealistic boundaries with some crossovers (see Figure 2.5). Due to this reason, we have resorted to an alternative definition for cell boundaries described in this section.

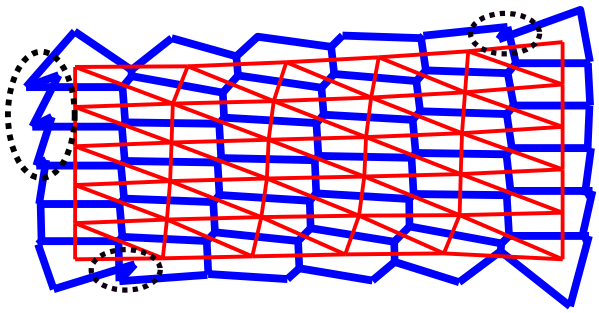

Figure 2.5: Delaunay triangulation and Voronoi tessellation, with crossovers indicated with dashed lines.

Barycentric coordinates of a triangle is a method of defining a location inside a triangle as a combination of the weight of the three vertices. We will apply the same filtering procedure described for the Voronoi tessellation, but obtaining the

vertices positions through the following interpolation:

$$V(\boldsymbol{\xi}) = \sum_{i \in Triangle} N_i(\boldsymbol{\xi}) \boldsymbol{x}_i, \qquad \boldsymbol{\xi} = (\frac{1}{3}, \frac{1}{3}), \tag{2.9}$$

where $N_i(\boldsymbol{\xi})$ are the standard Finite Element shape functions. This alternative generation of the cell boundaries will be used in Chapter 5, when analysing the stress relaxation of suspended monolayers. Although we do not aim here to assign mechanical properties to the bars of the boundaries, we do aim to have a realistic representation for future mechanical analyses where both networks carry mechanical properties. Figure 2.6 shows the cell boundaries (thick lines) obtained from Voronoi and barycentric tessellations for a 5 by 5 Cartesian mesh. The barycentric tessellation method is more robust than the Voronoi tessellation method and the cells shape obtained by this method is more realistic (see Figure 2.6b), since regular rectangular cell shapes are avoided in the former..

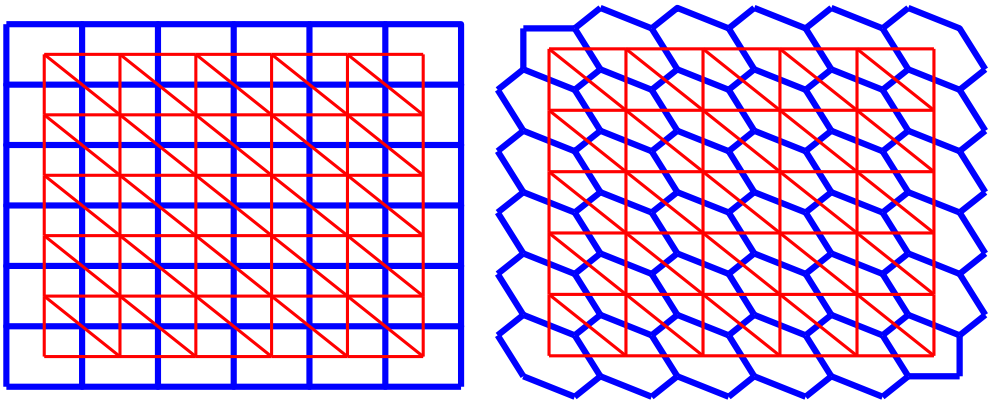

(a) (b)

Figure 2.6: Graphical representation of a 5 by 5 Cartesian mesh using (a) Voronoi tessellation (thick lines) and (b) barycentric tessellation (thick lines).

2.6 Application to real tissues

Here we apply the methods described in the previous sections to an image of real cells obtained by the group of Guillaume Charras at University College London (UCL).

Figure 2.7a shows an image of Madin-Darby Canine Kidney (MDCK) cells. MDCK cells image were obtained using a confocal microscope (Olympus IX-81 with an FV-1000 confocal head). Packing Analyzer [Aigouy et al., 2010] was used to segment the image (Figure 2.7b). Matlab (Mathworks, 2012) was used to binarise the images and find the positions of cell boundaries and centroids (Figure 2.7b). The Voronoi tessellation (thick lines in Figure 2.7b) of the cell

centres (dots) showing a good agreement with the experimental image (white line).

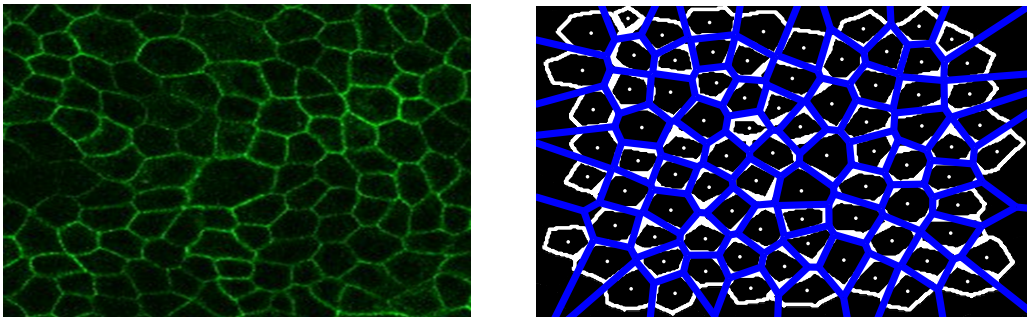

(a) (b)

Figure 2.7: (a) MDCK cells phase contrast image. (b) Tracking the boundaries and cell centres using the Packing Analyzer (white lines and dots). Thicker lines are the Voronoi tessellation of the cell centres (dots).

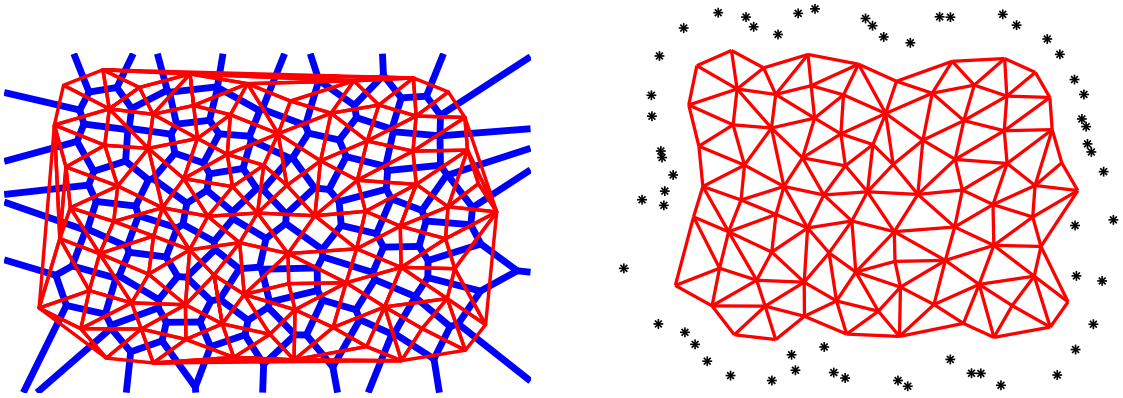

(a) (b)

Figure 2.8: (a) The cell-cell connectivities and the cell boundaries obtained from the real cell image. (b) Filtering the undesirable simplexes in Delaunay triangulation and adding the off-set nodes.

The cell-cell connectivity (thin lines) and the cell boundaries (thick lines) obtained from the experimental image are shown in Figure 2.8a. As we discussed in Section 2.4, Delaunay triangulation of a set of points results in a triangulation of the convex hull of the points with distant boundary cells being unrealistically connected. Therefore, after applying the filtering condition, the unrealistic elements on the boundary were removed (thin lines in Figure 2.8b).

The thick lines in Figure 2.8a show the bounded Voronoi regions for the internal nodes, and the unbounded regions for the external nodes. According to the method presented in Section 2.5, first a set of off-set nodes were added to

the original set of nodes at the boundary (see the stars in Figure 2.8b) and then a Voronoi tessellation was applied over the original and off-set nodes (see Figure 2.9a, thick lines). Finally, the geometry of all the cell boundaries is obtained by removing the off-set nodes as shown in Figure 2.9b.

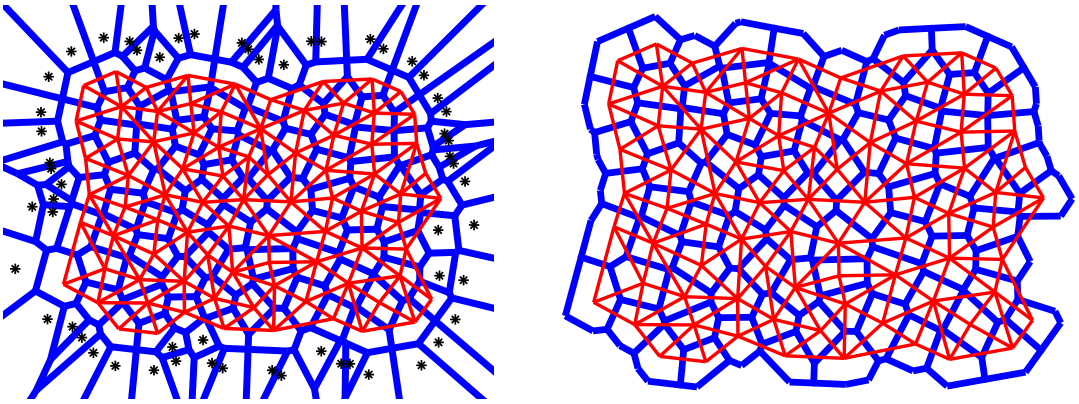

(a) (b)

Figure 2.9: (a) Applying a Voronoi tessellation on the original set of nodes and the off-sett nodes. (b) Final geometry after removing the off-set cells and nodes.

Figure 2.10a shows the experimental image (white lines and dots) with a superimposed barycentric tessellation (thick lines). After using the same construction of the off-set nodes, and applying the barycentric tessellation, the final cell geometry shown in Figure 2.10b is obtained.

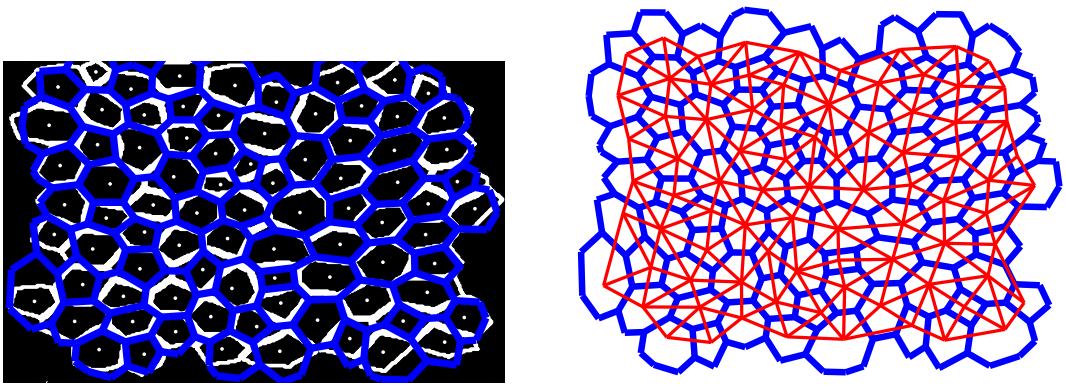

(a) (b)

Figure 2.10: (a) Tracking the boundaries and cell centres using the Packing Analyzer (white lines and dots). Thicker lines are the barycentric tessellation of the cell centres (dots). (b) Final geometry using barycentric tessellation. Thick lines and thin lines represent the cell boundaries and cell-cell connectivity, respectively.

While the two methodologies give a similar outlook of the cell distribution,

the junctions of the barycentric tessellation do not joint four cells, as experimental images also reflect, while this energetically costly distribution is frequently present in Voronoi tessellations. In addition, barycentric distribution ensures that no crossovers are generated.

Chapter 3

Rheological models for active cellular tissues

3.1 Introduction

We here describe some classical and new rheological models for viscoelastic tissues. Since we aim to apply those models to truss systems, we restrict the explanation to one-dimensional rheology and apply this to bar elements that form the truss system representing the tissue.

We present first in Section 3.2 a classical Maxwell element, using a well-known monolithic formulation that we recast, and also a novel formulation based on null-space projection and static condensation. Section 3.3 introduces an active model, that mimics the viscoelastic response, but interpreted as a change of resting length. Special attention is paid for the cases when remodelling occurs due to changes in the network topology. Section 3.5 presents some representative numerical results where the non-linear elastic response is used to simulate the fluidisation process, and also gives some analytical comparison between the Maxwell and active model.

3.2 Maxwell rheological model

3.2.1 Monolithic solution

The main assumption of the linear Maxwell model is that the viscous and elastic stresses are equal, i.e. $\sigma^e = \sigma^v = \sigma$ and are given by

$$\sigma^e = k\varepsilon^e \quad , \quad \sigma^v = \eta\dot{\varepsilon}^v, \tag{3.1}$$

with k and η the material stiffness and viscosity, respectively. On the other hand, the strains must satisfy the following kinematic constraint:

$$\dot{\varepsilon} = \dot{\varepsilon}^e + \dot{\varepsilon}^v, \tag{3.2}$$

with ε the total strain. By combining equations (3.1) and (3.2), we obtain the following linear evolution law,

$$\dot{\sigma} = k\left(\dot{\varepsilon} - \frac{\sigma}{\eta}\right),$$

which after using the time-discretisation $\sigma(t_n) \approx \sigma_{n+\theta} = (1-\theta)\sigma_n + (\theta)\sigma_{n+1}$ and $\dot{\sigma} \approx \frac{\Delta\sigma}{\Delta t}$ with $\Delta(\bullet) = (\bullet)_{n+1} - (\bullet)_n$, allows us to express current stresses σ_{n+1} as,

$$\sigma_{n+1} = \left(1 + \frac{k\theta\Delta t}{\eta}\right)^{-1}\left(k\Delta\varepsilon + \left(1 + \frac{k\Delta t(\theta-1)}{\eta}\right)\sigma_n\right). \tag{3.3}$$

The extension of the outlined procedure to multidimensional finite-strain viscoelasticity is usually achieved by replicating the linear evolution law in equation (3.3) with stress-like internal variables [Lubliner, 2008, Valanis, 1972], or for the analysis on a continuous spectrum and using quasi-linear viscoelasticity [Fung, 1993], numerically approximating the convolution integral [Puso and Weiss, 1998]. However, in some situations, the linear evolution law in equation (3.3) may not be sufficient to simulate the viscoelastic response of living tissues. These kind of non-linearities in the viscous contribution have motivated the methodology presented in this thesis.

3.2.2 Maxwell model as a two element formulation

A two noded bar element is deduced here with viscoelastic properties which in the linear case (no large rotations) is equivalent to the monolithic rheological model described in the previous section. The advantage of such an element is that it can handle any elastic and viscous constitutive laws, and can be employed in analyses with large deformations and displacements.

The configuration of a bar element is defined by the positions of the two end points. At the initial (stress-free) and current configurations, they are respectively given by the pairs $(\boldsymbol{X}_1, \boldsymbol{X}_2)$ and $(\boldsymbol{x}_1, \boldsymbol{x}_2)$.

Kinematics

The key idea in this formulation consists in splitting the elastic and viscous components of a viscoelastic bar in a series of two distinct elements, in the same manner as it is done in equation (3.2). More specifically, the whole viscoelastic element, that joints nodes $\boldsymbol{x}_1$ and $\boldsymbol{x}_2$, has an additional intermediate node $\boldsymbol{x}_3$ that determines the elastic component (between nodes $\boldsymbol{x}_1$ and $\boldsymbol{x}_3$), and the viscous component (between nodes $\boldsymbol{x}_3$ and $\boldsymbol{x}_2$) (see Figure 3.1a). The elastic and viscous elements are allowed to have any general constitutive law, which is so far left unspecified.

As shown in Figure 3.1b, node $\boldsymbol{x}_3$ is constrained to move along the line joining nodes 1 and 2, and its position is thus determined by an internal variable λ

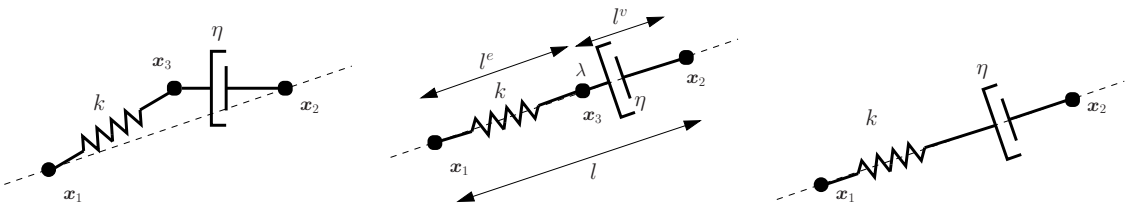

Figure 3.1: Representation of construction process of Maxwell element: (a) initial 2 elements, (b) constrained 2 elements where node 3 is enforced to move along line between nodes 1 and 2, and (c) final element after static condensation of internal degree of freedom (dof) λ.

as follows:

$$\boldsymbol{x}_3 = \boldsymbol{x}_1 + \lambda(\boldsymbol{x}_2 - \boldsymbol{x}_1). \tag{3.4}$$

The total initial (stress-free) and total current lengths of the bar are obtained as $L_0 = \|\boldsymbol{X}_2 - \boldsymbol{X}_1\|$ and $l = \|\boldsymbol{x}_2 - \boldsymbol{x}_1\|$, respectively, while the elastic and viscous lengths of the bar will be denoted by $l^e = \|\boldsymbol{x}_1 - \boldsymbol{x}_3\|$ and $l^v = \|\boldsymbol{x}_2 - \boldsymbol{x}_3\|$. In agreement with the rheological splitting, the scalar elastic and viscous strains are defined by,

$$\varepsilon^e = \frac{l^e - L_0^e}{L_0} \quad , \quad \varepsilon^v = \frac{l^v - L_0^v}{L_0}. \tag{3.5}$$

As it can be verified, these definition satisfy the relation $\varepsilon = \varepsilon^e + \varepsilon^v$, with $\varepsilon = (l - L_0)/L_0$. It should be noted that these strain measures are evaluated along the arbitrary bar direction, and also that the relation between the length measures l^e and l^v, and the nodal positions $\boldsymbol{x}_i$ is non-linear. Therefore, the strain measures correspond to non-linear co-rotated strains which can handle large bar displacements and rotations.

Null-space projection

We will assume that the global equilibrium of the elastic and viscous part of a viscoelastic bar may constructed by assembling the following two general nodal residuals corresponding to the elastic and viscous contribution, denoted by $\hat{\boldsymbol{g}}^e$ and $\hat{\boldsymbol{g}}^v$, respectively:

$$\hat{\boldsymbol{g}}^e = \left\{ \begin{array}{c} \hat{\boldsymbol{g}}_1^e \\ \hat{\boldsymbol{g}}_3^e \end{array} \right\} \quad , \quad \hat{\boldsymbol{g}}^v = \left\{ \begin{array}{c} \hat{\boldsymbol{g}}_3^v \\ \hat{\boldsymbol{g}}_2^v \end{array} \right\}, \tag{3.6}$$

where the subscripts denote the node to which each component is associated.

After assembling, the following global residual $\hat{\boldsymbol{g}}$ and corresponding Jacobian $\hat{\mathbf{K}}$ are obtained,

$$\hat{\boldsymbol{g}} = \left\{ \begin{array}{c} \boldsymbol{g}_1^e \\ \boldsymbol{g}_3^e + \boldsymbol{g}_3^v \\ \boldsymbol{g}_2^v \end{array} \right\} = \left\{ \begin{array}{c} \hat{\boldsymbol{g}}_1 \\ \hat{\boldsymbol{g}}_3 \\ \hat{\boldsymbol{g}}_2 \end{array} \right\} \tag{3.7}$$

$$\hat{\mathbf{K}} = \left[\begin{array}{ccc} \mathbf{K}_{11}^e & \mathbf{K}_{13}^e & \mathbf{0} \\ \mathbf{K}_{31}^e & \mathbf{K}_{33}^e + \mathbf{K}_{33}^v & \mathbf{K}_{32}^v \\ \mathbf{0} & \mathbf{K}_{23}^v & \mathbf{K}_{22}^v \end{array} \right] = \left[\begin{array}{ccc} \hat{\mathbf{K}}_{11} & \hat{\mathbf{K}}_{13} & \hat{\mathbf{K}}_{12} \\ \hat{\mathbf{K}}_{31} & \hat{\mathbf{K}}_{33} & \hat{\mathbf{K}}_{32} \\ \hat{\mathbf{K}}_{32} & \hat{\mathbf{K}}_{23} & \hat{\mathbf{K}}_{22} \end{array} \right], \tag{3.8}$$

which are conjugate to the virtual displacement vector $\{\delta\boldsymbol{x}_1^T, \delta\boldsymbol{x}_3^T,\ \delta\boldsymbol{x}_2^T\}$. The total virtual work (elastic and dissipated in the viscous element) is then expressed as:

$$\delta\mathcal{W} = \{\delta\boldsymbol{x}_1^T\ \delta\boldsymbol{x}_3^T\ \delta\boldsymbol{x}_2^T\}\hat{\boldsymbol{g}}. \tag{3.9}$$

On the other hand, the kinematic constraint in equation (3.4) induces the following relation between the virtual counterparts:

$$\delta\boldsymbol{x}_3 = (1-\lambda)\delta\boldsymbol{x}_1 + (\boldsymbol{x}_2 - \boldsymbol{x}_1)\delta\lambda + \lambda\delta\boldsymbol{x}_2. \tag{3.10}$$

This equation allows us to write the following relation between the unconstrained dof $\delta\{\boldsymbol{x}_1^T\ \lambda\ \boldsymbol{x}_2^T\}$ and the constrained dof $\delta\{\boldsymbol{x}_1^T\ \boldsymbol{x}_3^T\ \boldsymbol{x}_2^T\}$:

$$\delta \left\{ \begin{array}{c} \boldsymbol{x}_1 \\ \boldsymbol{x}_3 \\ \boldsymbol{x}_2 \end{array} \right\} = \left[\begin{array}{ccc} \mathbf{I} & \mathbf{0} & \mathbf{0} \\ (1-\lambda)\mathbf{I} & \boldsymbol{x}_2 - \boldsymbol{x}_1 & \lambda\mathbf{I} \\ \mathbf{0} & \mathbf{0} & \mathbf{I} \end{array} \right] \delta \left\{ \begin{array}{c} \boldsymbol{x}_1 \\ \lambda \\ \boldsymbol{x}_2 \end{array} \right\} = \mathbf{N}\delta \left\{ \begin{array}{c} \boldsymbol{x}_1 \\ \lambda \\ \boldsymbol{x}_2 \end{array} \right\}.$$

The total virtual work in (3.9) may be now re-expressed as,

$$\delta\mathcal{W} = \left\{\delta\boldsymbol{x}_1^T\ \delta\lambda\ \delta\boldsymbol{x}_2^T\right\}\mathbf{N}^T\hat{\boldsymbol{g}} = \left\{\delta\boldsymbol{x}_1^T\ \delta\lambda\ \delta\boldsymbol{x}_2^T\right\}\tilde{\boldsymbol{g}},$$

where matrix $\mathbf{N}^T$ *projects* the residual $\hat{\boldsymbol{g}}$ onto the new residual $\tilde{\boldsymbol{g}} := \mathbf{N}^T\hat{\boldsymbol{g}}$ which is conjugate to a reduced set of (unconstrained) variables, $(\delta\boldsymbol{x}_1,\ \delta\lambda,\ \delta\boldsymbol{x}_2)$. In fact, the first and third block columns of matrix $\mathbf{N}$ belong to the null-space of $\nabla\boldsymbol{\phi}$, with

$$\phi := \boldsymbol{x}_3 - \boldsymbol{x}_1 - \lambda(\boldsymbol{x}_2 - \boldsymbol{x}_1) = \mathbf{0}.$$

the kinematic constraint in (3.4). In other words, we have that,

$$\mathbf{N}^T(\nabla\boldsymbol{\phi})^T = \left\{ \begin{array}{c} \mathbf{0} \\ \boldsymbol{x}_2 - \boldsymbol{x}_1 \\ \mathbf{0} \end{array} \right\},$$

which allows us to solve the constrained system of equations $\hat{\boldsymbol{g}} = \mathbf{0}$ as the following unconstrained system which contains a reduced set of variables:

$$\tilde{\boldsymbol{g}} := \mathbf{N}^T \hat{\boldsymbol{g}} = \mathbf{0}.$$

The second block of equations in $\mathbf{N}^T\hat{\boldsymbol{g}}$, conjugate to $\delta\lambda$, corresponds to solving the equation $(\boldsymbol{x}_2 - \boldsymbol{x}_1)^T(\boldsymbol{g}_3^e + \boldsymbol{g}_3^v) = 0$, which imposes equilibrium of forces along the direction $\boldsymbol{x}_1 - \boldsymbol{x}_2$. Other applications of the null-space method to solve constrained systems of equations in the context of contact and multibody dynamics can be found in [Muñoz and Jelenić, 2004, Betsch, 2005].

The Jacobian of the reduced residual $\tilde{\boldsymbol{g}}$ is equal to:

$$\tilde{\mathbf{K}} = \mathbf{N}^T \hat{\mathbf{K}} \mathbf{N} + \mathbf{K}_N, \tag{3.11}$$

where $\mathbf{K}_N$ stems from the linearisation of matrix $\mathbf{N}$ and is equal to:

$$\mathbf{K}_N = \begin{bmatrix} \mathbf{0} & -\hat{\boldsymbol{g}}_3 & \mathbf{0} \\ -\hat{\boldsymbol{g}}_3^T & 0 & \hat{\boldsymbol{g}}_3^T \\ \mathbf{0} & \hat{\boldsymbol{g}}_3 & \mathbf{0} \end{bmatrix},$$

and $\hat{\mathbf{K}}$ is the matrix defined in (3.8). We note that we could alternatively define a constraint function solely dependent on $\boldsymbol{x}_1$, $\boldsymbol{x}_2$ and $\boldsymbol{x}_3$ such as,

$$\hat{\boldsymbol{\phi}} := \left(\mathbf{I} - \frac{(\boldsymbol{x}_3 - \boldsymbol{x}_1) \otimes (\boldsymbol{x}_2 - \boldsymbol{x}_1)}{\|\boldsymbol{x}_3 - \boldsymbol{x}_1\| \, \|\boldsymbol{x}_2 - \boldsymbol{x}_1\|} \right) (\boldsymbol{x}_3 - \boldsymbol{x}_1),$$

and construct an alternative matrix $\hat{\mathbf{N}}$ such that $\hat{\mathbf{N}}^T(\nabla\hat{\boldsymbol{\phi}})^T = \mathbf{0}$. In this manner, we would eliminate the equation conjugate to $\delta\lambda$ and avoid using an additional variable λ. We have instead kept this variable and used the reduction of the two bar system described above to ease the expression of $\mathbf{N}$ and better deduce from λ the elastic and viscous parts of the displacements. Furthermore, since the variable λ is internal to each viscoelastic element, it can be statically condensed [Muñoz et al., 2013], as it will be described next.

Static condensation of variable λ

Since the variable λ is internal to each viscoelastic element, it can be statically condensed. By using the following notation:

$$\tilde{\boldsymbol{g}} = \begin{Bmatrix} \tilde{\boldsymbol{g}}_1 \\ \tilde{g}_\lambda \\ \tilde{\boldsymbol{g}}_2 \end{Bmatrix}$$

$$\tilde{\mathbf{K}} = \begin{bmatrix} \tilde{\mathbf{K}}_{11} & \tilde{\mathbf{K}}_{1\lambda} & \tilde{\mathbf{K}}_{12} \\ \tilde{\mathbf{K}}_{\lambda 1} & \tilde{K}_{\lambda\lambda} & \tilde{\mathbf{K}}_{\lambda 2} \\ \tilde{\mathbf{K}}_{21} & \tilde{\mathbf{K}}_{2\lambda} & \tilde{\mathbf{K}}_{22} \end{bmatrix},$$

the static condensation may be achieved by eliminating from the second block of rows of equation

$$\tilde{\mathbf{K}} D \left\{ \begin{array}{c} \boldsymbol{x}_1 \\ \lambda \\ \boldsymbol{x}_2 \end{array} \right\} = -\tilde{\boldsymbol{g}}, \tag{3.12}$$

the variable $D\lambda$ as follows:

$$D\lambda = \tilde{K}_{\lambda\lambda}^{-1} \left(-\tilde{g}_\lambda - \tilde{\mathbf{K}}_{\lambda 1} D\boldsymbol{x}_1 - \tilde{\mathbf{K}}_{\lambda 2} D\boldsymbol{x}_2 \right). \tag{3.13}$$

Replacing this expression back into (3.12) yields the following reduced system of equations:

$$\mathbf{K}\ D \left\{ \begin{array}{c} \boldsymbol{x}_1 \\ \boldsymbol{x}_2 \end{array} \right\} = -\boldsymbol{g},$$

where the vector $\boldsymbol{g}$ and Jacobian $\mathbf{K}$ are given by:

$$\boldsymbol{g} = \left\{ \begin{array}{c} \tilde{\boldsymbol{g}}_1 - \tilde{K}_{\lambda\lambda}^{-1} \tilde{\mathbf{K}}_{1\lambda} \tilde{g}_\lambda \\ \tilde{\boldsymbol{g}}_2 - \tilde{K}_{\lambda\lambda}^{-1} \tilde{\mathbf{K}}_{2\lambda} \tilde{g}_\lambda \end{array} \right\} \tag{3.14}$$

$$\mathbf{K} = \left[\begin{array}{cc} \tilde{\mathbf{K}}_{11} - \tilde{K}_{\lambda\lambda}^{-1} \tilde{\mathbf{K}}_{1\lambda} \tilde{\mathbf{K}}_{\lambda 1} & \tilde{\mathbf{K}}_{12} - \tilde{K}_{\lambda\lambda}^{-1} \tilde{\mathbf{K}}_{1\lambda} \tilde{\mathbf{K}}_{\lambda 2} \\ \tilde{\mathbf{K}}_{21} - \tilde{K}_{\lambda\lambda}^{-1} \tilde{\mathbf{K}}_{2\lambda} \tilde{\mathbf{K}}_{\lambda 1} & \tilde{\mathbf{K}}_{22} - \tilde{K}_{\lambda\lambda}^{-1} \tilde{\mathbf{K}}_{2\lambda} \tilde{\mathbf{K}}_{\lambda 2} \end{array} \right]. \tag{3.15}$$

Note that from equation (3.13) we can update λ from the iterative values $D\boldsymbol{x}_1$ and $D\boldsymbol{x}_2$ as $\lambda^{k+1} = \lambda^k + D\lambda$. In summary, we have proposed viscoelastic constitutive laws that aim to model the observed mechanical response of living tissue, associated with both the active and passive interaction of all the structural elements in the cytoskeleton (actin fibers, myosin, cross-links, intermediate and apical filaments, microtubules, etc). We have determined such non-linear constitutive laws for our bar element by modifying their linear counterpart respectively. The equation governing the Maxwell bar element for living tissues is finally obtained by combining the viscous and elastic non-linear components as detailed above.

3.2.3 Constitutive laws for Maxwell element

Elastic element with linear law

The total elastic energy of a bar of total initial length L is determined in this case by the following quadratic potential energy,

$$U = \frac{L_0}{2} k (\varepsilon^e)^2, \tag{3.16}$$

with ε^e the elastic strain defined in equation (3.5). It is to note that since $L_0 = \|\boldsymbol{X}_1 - \boldsymbol{X}_2\| \neq L_0^e = \|\boldsymbol{X}_1 - \boldsymbol{X}_3\|$, the elastic strain ε^e differs from the total strain, and also from the standard strain of the reduced element between node

$\boldsymbol{x}_1$ and $\boldsymbol{x}_3$, which is given by $\varepsilon^* = (l^e - L_0^e)/L_0^e$. However, the relation between the latter and ε^e may be deduced as

$$\varepsilon^e = \frac{l^{e,n+1} - L_0^e}{L_0} = \lambda_0 \frac{l^{e,n+1} - L_0^e}{L_0^e} = \lambda_0 \varepsilon^*,$$

where $\lambda_0 = L_0^e/L_0$ is the value of parameter λ at the initial time t^0. The value of λ_0 does not affect the resulting elastic and viscous strains and stresses, as we have numerically verified. In our numerical tests we use $\lambda_0 = 0.5$. For clarity, in the remaining expressions, we will remove the superscript $n+1$.

The elastic stress is given by $\sigma^e = \partial U/\partial \varepsilon^e = k\varepsilon^e$, while the elastic contribution to the bar residual is explicitly given by,

$$\boldsymbol{g}^e = k\varepsilon^e \boldsymbol{e}_{13}, \tag{3.17}$$

where we have defined the vector $\boldsymbol{e}_{ij}$ as

$$\boldsymbol{e}_{ij} = \frac{1}{\|\boldsymbol{x}_i - \boldsymbol{x}_j\|} \left\{ \begin{array}{c} \boldsymbol{x}_i - \boldsymbol{x}_j \\ \boldsymbol{x}_j - \boldsymbol{x}_i \end{array} \right\}.$$

Elastic element with exponential law

Experiments on soft tissues have shown that the stiffness follows a exponential law with respect to the strains [Trepat et al., 2007]. In order to account for the phenomenology of this biological scenario we have adopted an elastic potential of the type:

$$U = \frac{k_0}{2\alpha}\left(1 - e^{-\alpha(\varepsilon^e)^2}\right), \tag{3.18}$$

with $\alpha > 0$ a parameter that depends on the material properties. The corresponding elastic stress is in this case given by,

$$\sigma_{el} = \frac{\partial U}{\partial \varepsilon^e} = k_0 \varepsilon^e e^{-\alpha(\varepsilon^e)^2}, \tag{3.19}$$

so that the elastic stress does not monotonically increase, but is eventually reduced as ε^e increases. At a given strain, the non-linear effective stiffness of the material can be computed as $k = k_0 e^{-\alpha\varepsilon^2}(1 - 2\alpha\varepsilon^2)$ which decreases as the elastic strain increases. The contribution to the residual of an elastic bar with nodal ends in $\boldsymbol{x}_1$ and $\boldsymbol{x}_3$ is therefore,

$$\boldsymbol{g}^e = k_0 \varepsilon^e e^{-\alpha(\varepsilon^e)^2} \boldsymbol{e}_{13}.$$

When comparing the quadratic and exponential elastic potentials in (3.16) and (3.18), it can be deduced that while in the former case the stored elastic energy is unbounded, in the latter case function U is bounded. Figure 3.2a shows the two kind of functions U, and in the exponential case, for two values of α, which shows that the larger is α, the lower is the maximum stored elastic energy. Figure 3.2b shows the corresponding stresses derived from the potential functions. As it can be observed, the limitation on the maximum value of U also implies that the elastic stress does not monotonically increase, but is eventually reduced as ε^e increases.

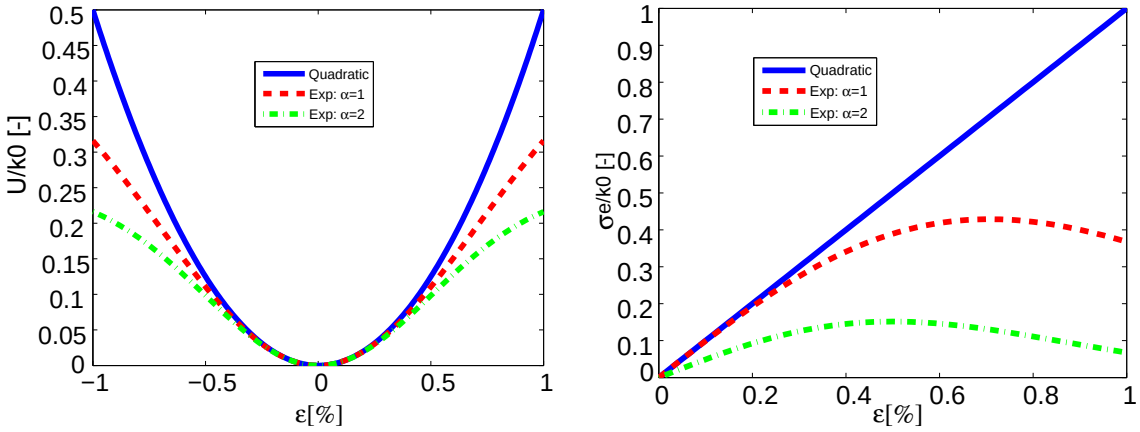

(a) (b)

Figure 3.2: (a) Elastic potential: quadratic function and exponential function with $\alpha = 1, 2$. (b) Corresponding stresses σ^e.

Viscous element with linear law

The residual stress of the viscous element with viscosity η is equal to $\sigma^v = \eta\dot{\varepsilon}^v$, which acts along the direction $\boldsymbol{x}_2 - \boldsymbol{x}_3$, and with $\varepsilon^{v,n+1} = \frac{l^{v,n+1} - L_0^v}{L_0}$ the viscous strain. The viscous contribution to the total residual is then given by,

$$\boldsymbol{g}^v = \eta\dot{\varepsilon}^v \boldsymbol{e}_{32}. \tag{3.20}$$

This contribution will be discretized in time by employing the time-step size $\Delta t = t^{n+1} - t^n$ and the following time-stepping,

$$\boldsymbol{g}^{v,n+\theta} = \eta \frac{l^{v,n+1} - l^{v,n}}{L\Delta t} \boldsymbol{e}_{32}^{n+\theta} = \lambda_0 \eta \frac{l^{v,n+1} - l^{v,n}}{L^v \Delta t} \boldsymbol{e}_{32}^{n+\theta}, \tag{3.21}$$

where

$$\begin{aligned} l^{v,n+\theta} &= \|\boldsymbol{x}_2^{n+\theta} - \boldsymbol{x}_3^{n+\theta}\| \\ l^{v,n} &= \|\boldsymbol{x}_2^{n} - \boldsymbol{x}_3^{n}\| \\ \boldsymbol{g}^{v,n+\theta} &= (1-\theta)\boldsymbol{g}^{v,n} + \theta \boldsymbol{g}^{v,n+1} \\ \boldsymbol{e}_i^{n+\theta} &= (1-\theta)\boldsymbol{e}_i^{n} + \theta \boldsymbol{e}_i^{n+1}, \end{aligned}$$

with $\theta \in [0, 1]$ an algorithmic parameter. From equation (3.21), it follows that the viscous force contribution at time t^{n+1}, to be assembled together with the elastic part deduced above, reads

$$\boldsymbol{g}^{v,n+1} = \frac{\theta - 1}{\theta} \boldsymbol{g}^{v,n} + \frac{\eta}{\theta L} \frac{l^{v,n+1} - l^{v,n}}{\Delta t} \boldsymbol{e}_{32}^{n+\theta}. \tag{3.22}$$

Viscous element with exponential law

Similarly to the elastic case, it has been experimentally observed that the material viscosity may decrease after an imposed stretching process [Trepat et al., 2007]. In order to mimic such a behaviour at the micro-scale level, we have suggested the following non-linear viscous law:

$$\boldsymbol{g}^v = \eta_0 e^{-\beta(\varepsilon^v)^2} \dot{\varepsilon}^v \boldsymbol{e}_{32}. \tag{3.23}$$

In this case, the factor $\eta = \eta_0 e^{-\beta(\varepsilon^v)^2}$ has the role of strain-dependent effective viscosity that decreases as the viscous strain increases. The time integration of the previous equation is resolved resorting again to a $\theta-$averaged time-stepping,

$$\boldsymbol{g}^{v,n+\theta} = \eta_0 e^{-\beta(\varepsilon^{v,n+\theta})^2} \frac{\Delta\varepsilon^v}{\Delta t} \boldsymbol{e}_{32}^{n+\theta}.$$

3.3 Active rheological model

3.3.1 Introducing a variable resting length

The actin cytoskeleton is a network of protein-polymers that are responsible for the mechanical stability of cells and, due to its remodelling and (de)polymerisation of the actin filaments, may strongly affect cell rheology. Indeed, it has been shown that inhibition of the actomyosin cytoskeleton increases the tissue viscosity [Azevedo et al., 2011, Ma et al., 2009].

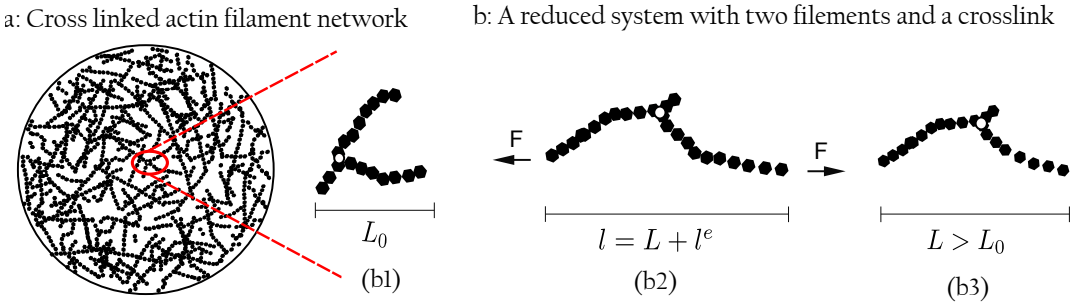

Figure 3.3: (a) Schematic of network of actin filaments connected by flexible cross-links. (b) Schematic of strain induced changes in the resting length L of a reduced system with two filaments and a cross-link (white circle). (b1) Initial configuration with resting length equal to L_0. (b2) Configuration under an applied load. (b3) New unstrained configuration with modified resting length $L > L_0$.

From the physical perspective, when a set of cross-linked actin filaments in the cytoskeleton is subjected to a macroscopic strain, it stretches mainly as a

result of two combined phenomena: (i) a reversible (elastic) deformation and a (ii) non-reversible remodelling and lengthening, due to the remodelling of the cross-links and (de)polymerisation process of the filaments. Figure 3.3 illustrates schematically this two combined effects for a pair of cross-linked polymers under a stretching process.

Consistent with this observation, we propose the following evolution law for the resting length L_{ij}[1] between two connected cells i and j,

$$\dot{L}_{ij} = \gamma \varepsilon^e_{ij} L_{ij} = \gamma (l_{ij} - L_{ij}), \tag{3.24}$$

that is, the relative changes of the resting length L_{ij} are proportional to the elastic strain $\varepsilon^e = \frac{(l_{ij}-L_{ij}),}{L_{ij}}$, which we point out that is different from the *apparent strain* $\varepsilon_{ij} = \frac{(l_{ij}-L_{0,ij})}{L_{0,ij}}$, with $L_{0,ij} = l_{0,ij}$, the initial length. The parameter γ will be called the *remodelling rate*, and represents the ability of the network to adapt its resting length when subjected to stress. It has been shown that this evolution law is equivalent to a Maxwell like rheological model [Muñoz and Albo, 2013]. This comparison will be also included in Section 3.5 for completness reasons.

The evolution law in (3.24) is combined with a purely linear elastic constitutive law in (2.1). Equation (3.24) is solved by using a θ-weighted scheme [Isaacson and Keller, 1966]:

$$L^{n+1}_{ij} - L^n_{ij} = \Delta t \gamma (l^{n+\theta}_{ij} - L^{n+\theta}_{ij}), \tag{3.25}$$

with $(\bullet)^{n+\theta} = (1-\theta)(\bullet)^n + \theta(\bullet)^{n+1}$. The elemental active length L_{ij} can be statically condensed, so that only displacement degrees of freedom are globally solved. We do not describe this static condensation process here, but in Chapter 4 we explain an extension of this process, when it is further combined with additional elemental variables.

3.3.2 Extension to tissues undergoing remodelling

From endocytosis to crawling motility, a vast array of cellular functions require the cytoskeleton to organize and remodel the intracellular space and surrounding membranes. In the previous section we proposed an evolution law for the cytoskeleton remodelling (intracellular changes). However, if the cell-cell connectivity changes and need to be recomputed as explained in the previous chapter, some new elements are created for which no information is available regarding the active length at the previous time step. We propose in the next paragraphs a methodology for finding the active length for the newly created elements.

[1]When describing the active length model, it will become convenient to explicitly write in the subscript the two nodes, i and j, to which the length variable L refers to.

Update of active length

The time discretisation of the evolution law in (3.24) requires the evaluation of the active length at times t^{n+1} and t^n, respectively, denoted by L_{ij}^{n+1} and L_{ij}^n. However, due to the redefinition of the cell-cell connectivity, it may well be that the element ij exists at time t^{n+1} but not at time t^n. For this reason, we compute a nodal *Active Length Tensor* $\mathbf{L}^i$, which will allow to compute the active length along direction $\boldsymbol{n}_j$ as,

$$L_{ij} = \boldsymbol{n}_j \cdot \mathbf{L}^i \boldsymbol{n}_j. \tag{3.26}$$

This relation allows for interpreting tensor $\mathbf{L}^i$ as a strain tensor, where the quantity $\boldsymbol{n}_j \cdot \mathbf{L}^i \boldsymbol{n}_j$ corresponds to the stretching along $\boldsymbol{n}_j$. Since the skew part of $\mathbf{L}^i$ does not affect the value of $\mathbf{L}^{ij}$ in (3.26), and in order to keep the similarity between $\mathbf{L}^i$ and a deformation tensor, we will assume that $\mathbf{L}^i$ is symmetric.

It is clear that for a given node i, the existence of an active length tensor $\mathbf{L}^i$ satisfying exactly the relationship in (3.26) for all current cell-cell connections ij may not be possible. Therefore, the tensor $\mathbf{L}^i$ is computed by minimising the following quadratic error function:

$$E_i = \frac{1}{2} \sum_{j=1}^{N} ||\mathbf{L}^i \boldsymbol{n}_j - L_{ij} \boldsymbol{n}_j||^2. \tag{3.27}$$

Due to the symmetry of $\mathbf{L}^i$, we will write this tensor in the following forms, for $2D$ and $3D$ analyses,

$$\bar{\mathbf{L}}^i_{2D} = \{L_{xx}, L_{yy}, L_{xy}\}^T \quad , \quad \bar{\mathbf{L}}^i_{3D} = \{L_{xx}, L_{yy}, L_{zz}, L_{xy}, L_{xz}, L_{yz}\},$$

so that $\mathbf{L}^i \boldsymbol{n}_j = \mathbf{N}_j \mathbf{L}^i$, with $\mathbf{N}_j$ a matrix that contains the components of the unit vector $\boldsymbol{n}_j$. Then, the error E_i reads:

$$E_i = \frac{1}{2} \sum_{j=1}^{N} ||\mathbf{N}_j \bar{\mathbf{L}}^i - L_{ij} \boldsymbol{n}_j||^2,$$

and its derivative with respect to each one of the components of $\mathbf{L}^i$ gives rise to the following system of equations:

$$\mathbf{A} \bar{\mathbf{L}}^i = \mathbf{b}, \tag{3.28}$$

with,

$$\mathbf{A} = \sum_{j=1}^{N} \mathbf{N}_j^T \mathbf{N}_j \quad , \quad \mathbf{b} = \sum_{j=1}^{N} L^{ij} \mathbf{N}_j^T \boldsymbol{n}_j.$$

The error measure E_i in (3.27) is a quadratic function that has a unique minimiser as far as the vectors $\boldsymbol{n}_j$ span $\mathbb{R}^{n_{sd}}$, with n_{sd} the number of space

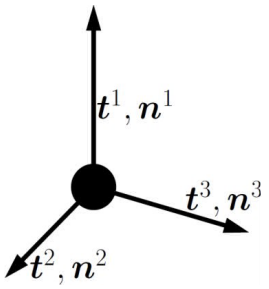

Figure 3.4: Schematic view of a node in equilibrium under traction and compression by connecting elements.

dimensions. Appendix A gives a proof of this fact. The symmetry of $\mathbf{L}^i$ is not required in the proof of uniqueness, which opens the possibility for considering a non-symmetric tensor $\mathbf{L}^i$. However, in this case, the system of equation in (3.28) would contain more unknowns, without any qualitative improvement in the retrieved active lengthening $L_{ij} = \boldsymbol{n}_j \cdot \mathbf{L}^i \boldsymbol{n}_j$.

3.4 Stress recovery

Here, we aim to compute a nodal distribution of the stress field of the tissue, from the tractions at the bar elements.. There are two options to obtain the stress values:

(**i**) Using the nodal displacement u: Having obtained the nodal displacement for each bar element, stress values can be calculated from the derivatives of the displacement (strains), which in our case would be discontinuous. In this case, we would require to compute a continuous strain field $\epsilon(u)$, and retrieve the stress field from an assumed strain-stress relationship for the solid elements formed by the triangulation. Therefore, due to the non-linearities of the material which is modelled with bar elements, it is not easy to deduce a valid strain-stress relationship.

(**ii**) Using elemental traction $\boldsymbol{t}$: We assume that the tractions result from a nodal stress, i.e $\boldsymbol{t} = \boldsymbol{\sigma n}$. This relation may not be satisfied for all elements connected to the node. Hence, we will use the following definition of the error between the nodal stress $\hat{\boldsymbol{\sigma}}$ and all elemental tractions $\boldsymbol{t}^i$ acting on a node,

$$E = \sum_{i=1}^{n} ||\boldsymbol{N}^i \hat{\boldsymbol{\sigma}} - \boldsymbol{t}^i||^2, \tag{3.29}$$

where $\boldsymbol{N}$ contains the components of the normal vector and $\hat{\boldsymbol{\sigma}}$ is nodal stresses which are supposed to be determined, n is the number of bar element connected to the node and $\boldsymbol{t}$ is the known traction for each bar element. For a 2D bar

element, $\boldsymbol{N}$ and $\hat{\boldsymbol{\sigma}}$ can be expressed as,

$$\boldsymbol{N} = \begin{bmatrix} n_x & n_y & 0 \\ 0 & n_x & n_y \end{bmatrix}$$
$$\hat{\boldsymbol{\sigma}} = \begin{bmatrix} \sigma_{xx} \\ \sigma_{xy} \\ \sigma_{yy} \end{bmatrix}.$$

The nodal stresses $\hat{\boldsymbol{\sigma}}$ may be achieved by minimizing the error function in (3.29),

$$\boldsymbol{A}\hat{\boldsymbol{\sigma}} = \boldsymbol{b}, \tag{3.30}$$

where,

$$\boldsymbol{A} = \sum_{i=1}^{n} \boldsymbol{N}^{i^T} \boldsymbol{N}^i$$
$$\boldsymbol{b} = 2\sum_{i=1}^{n} \boldsymbol{N}^{i^T} \boldsymbol{t}^i.$$

The solution of the equation (3.30) is unique, if the directors $\boldsymbol{n}^i$ of the elements connected to the node span the space $\mathbb{R}^d$, with d the space dimension (See appendix.B).

3.5 Numerical results

3.5.1 Stress relaxation of single non-linear Maxwell element

In the subsequent examples the non-linear equations are solved using a fully Newton-Raphson method with $\theta = 0.5$, which has ensured numerically stable results. In all cases, we have used the reference value $k_0 = 1$, and in the one bar example in Section 3.5.1, we have used the value $\eta_0 = 4$, which agrees with the relation $\eta_0/k_0 = 4$ measured experimentally in [Trepat et al., 2007]. We have fixed the left boundary and prescribed the displacements at the right boundary according to the function $\bar{u}$ shown in Figure 3.5a.

We have first analysed the Maxwell element in Figure 3.5a with the values $\alpha = 1, 10, 20, 30$ and $\beta = 0$. As indicated in equation (3.19), the effective stiffness $k = k_0 e^{-\alpha(\varepsilon^e)^2}(1 - 2\alpha(\varepsilon^e)^2)$ decreases as ε^e increases, and this reduction is more pronounced as the material parameter α increases. For $t > 2$ the global bar element remains undeformed while the stress recovers asymptotically to its original value after approximately one time unit.

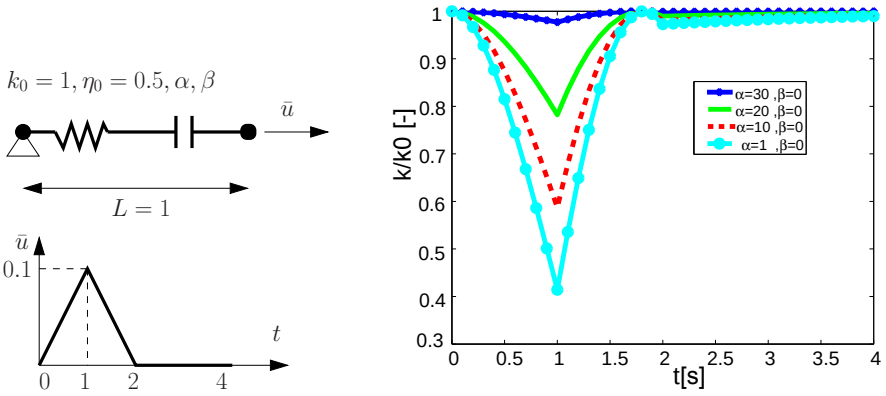

(a) (b)

Figure 3.5: 1 bar element with constrained displacements. (a) Geometry, material properties and boundary conditions. (b) Value of the effective stiffness $k = k_0 e^{-\alpha(\varepsilon^e)^2}\,(1 - 2\alpha(\varepsilon^e)^2)$.

In order to also model the reversible drop in the viscosity, we applied the non-linear viscous law given in (3.20) with $\beta = 0$ (linear viscosity) and $\beta = 100$, while using $\alpha = 30$ in both cases. Figure 3.6 shows the evolution of the effective stiffness and viscosity. When $\beta = 100$, the viscosity is reduced by more than 50% with respect to the analysis with $\beta = 0$. More importantly, the variation of β has minimal effects on the evolution of the effective stiffness, which allows us to fit the parameters α and β independently.

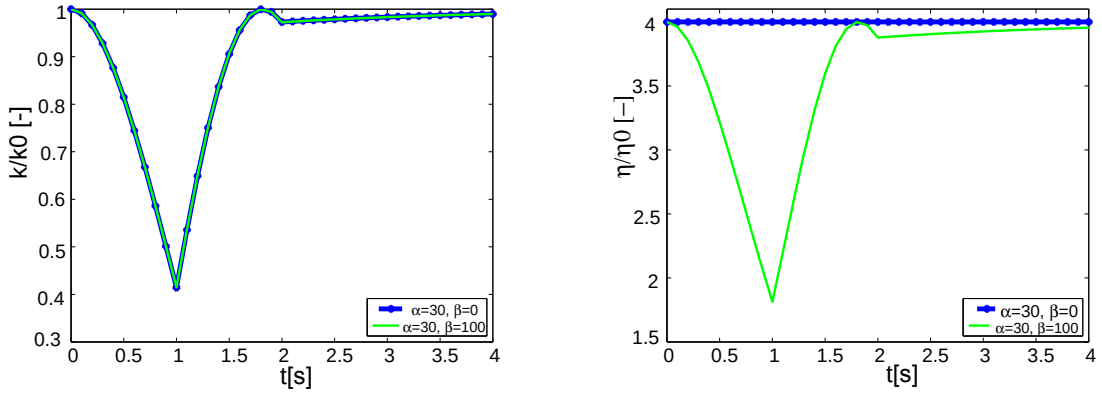

(a) (b)

Figure 3.6: 1 bar element with non-linear viscosity. Evolution of (a) the effective stiffness $k = k_0 e^{-\alpha(\varepsilon^e)^2}\,(1 - 2\alpha(\varepsilon^e)^2)$ and (b) the effective viscosity $\eta = \eta_0 e^{-\beta(\varepsilon^v)^2}$.

We have also attempted to reproduce the evolution of the phase angle $\delta = \tan^{-1}(k/\eta)$ for the Maxwell element, and for different values of the maximum displacement. Figure 3.7a shows the measured evolution , while Figure 3.7b shows the evolution after applying the strain during the first 2 units of time (no experimental data is available for the evolution of δ while the material is stretched). We have used the parameters $\alpha = 10$ and $\beta = 400$, with the same values of k and

η_0 previously employed. It can be observed that the numerical and experimental curves exhibit similar trends, although in our numerical experiments the recovery time is much shorter. Furthermore, the evolution of the material stiffness, which during the experiment was undergoing a softening process, is not properly captured with the present model. A more complete model that captures both, δ decrease and softening, that is, a fluidisation process, is developed in the next chapter.

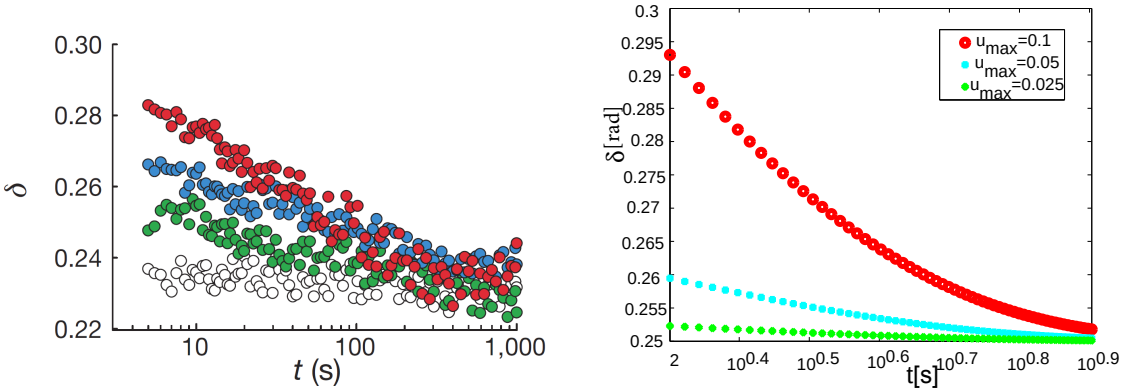

(a) (b)

Figure 3.7: Experimental evolution of the phase angle (radian) after applying the stretch cycle, and numerical results when using one element for different values of maximum displacement.

3.5.2 Stress relaxation of 3D tissues

By embedding of the Maxwell bar element in 3D networks, the simulation of non-linear response of 3D domains of tissues under large strains and rotations is facilitated. In this section, nodes will not be considered as cells, but rather as a suitable discretisation of the monolayer, here described by tow layers of nodes, and linked through the truss system. Cellular tissues modelled as networks of bars may be thought of as a simplified version of generalised continua [Altenbach et al., 2011], where bending stiffness is disregarded and no rotational degree of freedom is accounted for. However, use of a truss system shows essential differences compared to the use of a continuum. In isotropic linear elasticity, for instance, continua are characterised by two material parameters whereas only one is necessary to fully assign constitutive behaviour of any truss system. Moreover, the Poisson effect in truss systems strongly depends on the topology of the network (e.g. [Hahn et al., 2010]), in the same way as the mechanical response depends on its interconnectivity and topology. Thus truss systems are particularly appealing for analysing polymer-like networks (e.g. [Kim et al., 2009, Cyron and Wall, 2010]), especially if one takes into account the ease and efficiency with which general non-linear laws of both elasticity and viscosity may be combined in the Maxwell bar element detailed in this chapter.

With these ideas in mind we built a 3D system of non-linear Maxwell elements that aims to emulate the global cytoskeletal actino-myosin network spreading across epithelial tissues through cell-cell junctions. The exponential law in (3.23) with elemental parameter $\alpha = 100$ has been adopted for each single bar element in the network (see Section 3.5.1). The epithelial cell patch is assumed to have generic dimensions $1.0 \times 1.0 \times 0.0625$ and formed by $E = 2473$ bars (Figure 3.8a). We have run two analyses, one with prescribed displacements $\bar{u}_x = \bar{u}$ and another with $\bar{u}_x = \bar{u}/2$.

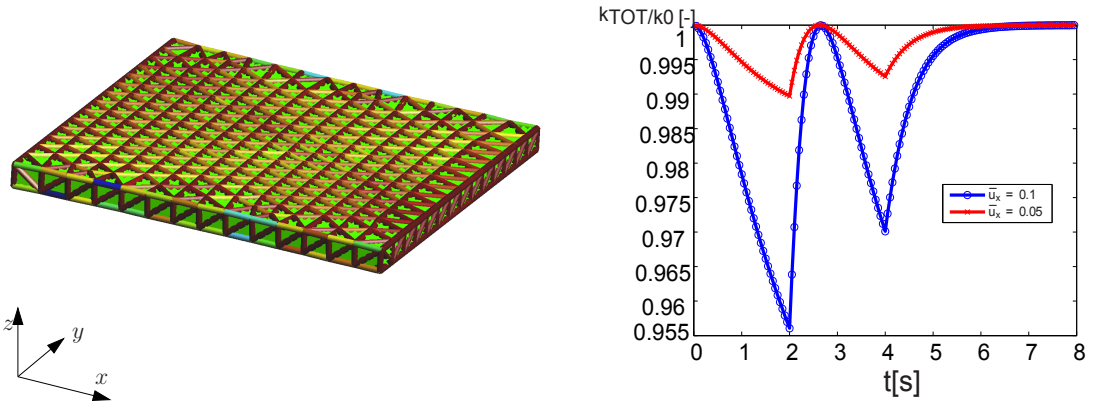

(a) (b)

Figure 3.8: (a) Deformed configuration at $t = 1$, with values of $k = k_0 e^{-\alpha(\varepsilon^e)^2}$ (b), where dark red indicates $k = 1$ and dark blue indicates $k \approx 0.5$. (b) Evolution of total effective stiffness k_{TOT}.

Due to the stretching, the epithelium undergoes a softening effect in the x direction. Figure 3.8a shows the contour plot of the values of the effective stiffness $k = k_0 e^{-\alpha(\varepsilon^e)^2}(1 - 2\alpha(\varepsilon^e)^2)$. As expected, those bars aligned to the x direction have their effective stiffness further reduced than those aligned to the y or z direction.

Figure 3.8b shows for the two values of the prescribed displacements, the evolution of the averaged total effective stiffness k_{TOT}, computed for N_E elements as $\bar{k}_{TOT} = \left(\sum_{i=1}^{N_E} k^i\right)/N_E$, with k^i the effective stiffness of bar i. Although the boundary conditions are similar to those in the previous example, the reduction in $\bar{k}_{TOT}$ is far smaller in the present case. This is due to the fact that the effective stiffness is averaged among all bars, regardless of their orientation, while the applied strain is highly anisotropic. In fact, during the stretching process, some bars have their effective stiffness reduced by 49%, while the stiffness of other bars, mostly perpendicular to the stretch, remains nearly unaffected.

3.5.3 Analytical comparison between Maxwell and Active rheological models

Here, we compare the response of the Active and Maxwell models to a sudden stretch (stress relaxation) and a constant load (creep). In these two cases, a single one-dimensional element with initial length L_0 and prescribed displacement at the right end was used.

Creep experiments

In the creep experiment, the element is submitted to a constant load σ_0 . In the Active model, by combining the evolution law in equation (3.24) with the equilibrium equation of a purely elastic element yields the following differential equation:

$$\frac{\dot{L}}{L} = \frac{\sigma_0}{k}\gamma. \tag{3.31}$$

After integrating this equation with the initial condition $L(t=0) = L_0$, we obtain the following expressions of the apparent strain, and resting and total lengths for Active model:

$$\begin{aligned} \varepsilon(t) &= (\frac{\sigma_0}{k} + 1)e^{\frac{\sigma_0\gamma t}{k}} - 1 \\ L(t) &= L_0 e^{\frac{\sigma_0\gamma t}{k}} \\ l(t) &= L_0(\frac{\sigma_0}{k} + 1)e^{\frac{\sigma_0\gamma t}{k}}. \end{aligned} \tag{3.32}$$

Instead, in a linear Maxwell element, the governing equation reads,

$$\dot{\varepsilon} = \frac{\dot{\sigma}}{k} + \frac{\sigma}{\eta}. \tag{3.33}$$

Then, the apparent strain and total length are given as follows,

$$\begin{aligned} \varepsilon(t) &= \frac{\sigma_0}{k}(1 + \frac{k}{\eta}t) \\ l(t) &= L_0(1 + \frac{\sigma_0}{k}(1 + t\frac{k}{\eta})). \end{aligned} \tag{3.34}$$

As can be observed in Figure 3.9a, the growth of both models is monotonically increasing to an unbounded value when subjected to a constant load. Regarding the corresponding equations of both models, a linear and an exponential growth is obtained for the Maxwell and Active models, respectively. While the elastic strain is the same and equal to σ_0/k for the Active and Maxwell element, the inspection of equations (3.34) and (3.32) reveals that close to the initial configuration $t \to 0$ and for small elastic strains $\sigma_0/k \to 0$, the apparent length are equal in the two elements if γ is replaced by k/η, as the plot of the evolution of l in Figure 3.9a confirms.

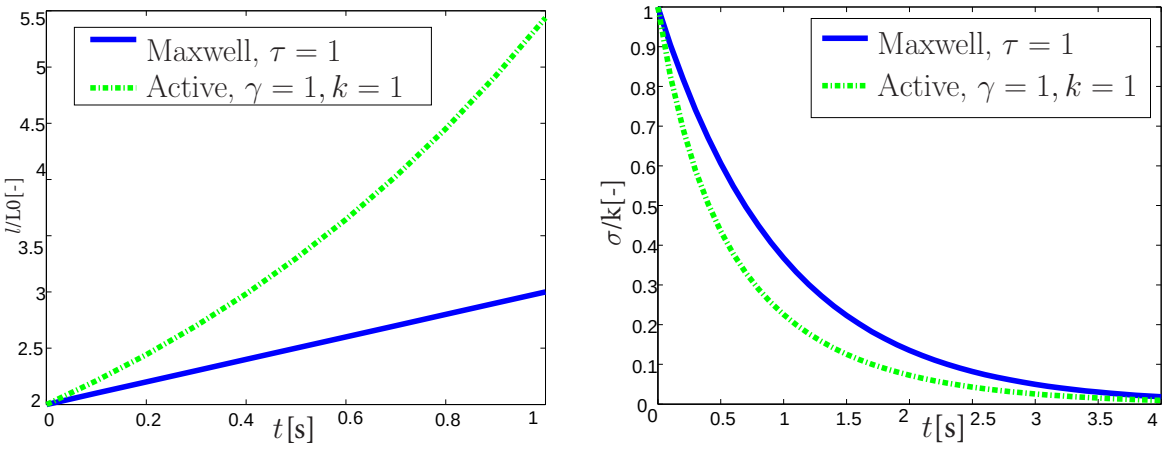

(a) (b)

Figure 3.9: Comparison between the Maxwell and Active model. (a) Evolution of the apparent length l on a creep test. (b) Evolution of the stress σ on a stress relaxation test.

Stress relaxation

In the stress relaxation experiment, the elements are stretched first by applying an increasing linear displacement during a short period of time and then with a constant displacement.

For the Active model, the following law for the total length was imposed,

$$l(t) = L_0 + ct. \tag{3.35}$$

Integrating equation (3.24) yields the following resting length L, elastic strain ε^e and stress σ,

$$\begin{aligned} L(t) &= L_0 + ct - \frac{c}{\gamma}(1 - e^{-\gamma t}) \\ \varepsilon(t) &= \frac{l(t) - L(t)}{L(t)} = \frac{1 - e^{-\gamma t}}{\frac{\gamma}{c}L_0 + \gamma t - (1 - e^{-\gamma t})} \\ \sigma(t) &= k\frac{1 - e^{-\gamma t}}{\frac{\gamma}{c}L_0 + \gamma t - (1 - e^{-\gamma t})}. \end{aligned} \tag{3.36}$$

The evolution of $L(t)$ after applying constant stretch is then given by the solution of (3.24) with $l(t) = L_1$, which yields,

$$\begin{aligned} L(t) &= L_1 - (L_1 - L_0)e^{-\gamma t} \\ \sigma(t) &= k\frac{(L_1 - L_0)e^{-\gamma t}}{L_1 - (L_1 - L_0)e^{-\gamma t}}. \end{aligned} \tag{3.37}$$

The comparison of the last expression with the stress evolution after applying the same experiment to a Maxwell element

$$\sigma(t) = \varepsilon_0 k e^{-\frac{k}{\eta}t}, \tag{3.38}$$

	G'	G''	$\tan\delta$
Kelvin-Voigt	k	$\eta\omega$	$\frac{\eta}{k}\omega$
Maxwell	$\frac{k\eta^2\omega^2}{k^2+\eta^2\omega^2}$	$\frac{k^2\eta\omega}{k^2+\eta^2\omega^2}$	$\frac{k}{\eta}\omega^{-1}$

Table 3.1: Values of storage modulus G', loss modulus G'' and tangent of phase angle for Kelvin-Voigt and Maxwell rheological models.

reveals that although the values of $\sigma(t)$ for $t = 0$ and $t \to \infty$ are the same in both cases, their evolutions are slightly different. However, for the particular case of small strains $\varepsilon << 1$, the stress relaxation curves approach each other. The plot of the stress evolution in Figure 3.9b shows the similarity of the two cases for $\varepsilon_0 = 1.0$.

3.5.4 Oscillatory displacements and stresses

In order to mimic standard rheology analysis of tissues with oscillatory boundary conditions at variable frequencies, we will analyse the behaviour of the active element for such conditions. When the element is subjected to the displacement boundary condition $l(t) = L_0(1 + \varepsilon_0 \sin(\omega t))$, the current active lengthening $L(t)$ is given by the solution of the differential equation in (3.24):

$$L(t) = L_0 + \frac{L_0\varepsilon_0}{\gamma^2+\omega^2}\left(\gamma\omega e^{-\gamma t} + \gamma^2\sin(\omega t) - \gamma\omega\cos(\omega t)\right)$$

It follows that the elastic strain is equal to,

$$\varepsilon^e(t) = \frac{\frac{\varepsilon_0}{\gamma^2+\omega^2}\left(\gamma\omega e^{-\gamma t} + \gamma^2\sin(\omega t) - \gamma\omega\cos(\omega t)\right)}{1 + \frac{\varepsilon_0}{\gamma^2+\omega^2}\left(\gamma\omega e^{-\gamma t} + \gamma^2\sin(\omega t) - \gamma\omega\cos(\omega t)\right)}$$

By assuming small strains, and a linear elastic relationship $\sigma = k\varepsilon^e$, the steady state response of the stresses at $t \to \infty$ has the following expression:

$$\sigma(t) \overset{t\to\infty}{=} k\varepsilon_0\frac{\omega^2\sin(\omega t) + \gamma\omega\cos(\omega t)}{\gamma^2+\omega^2+\varepsilon_0\gamma^2\sin(\omega t) - \varepsilon_0\gamma\omega\cos(\omega t)},$$

Due to the small strains assumption, ($|\varepsilon^e| << 1$), we can then compute the dynamic moduli and phase angle δ as,

$$\begin{aligned} G' &= \frac{k\omega^2}{\omega^2+\gamma^2} \\ G'' &= \frac{k\gamma\omega}{\omega^2+\gamma^2} \\ \delta &= \arctan(\gamma\omega^{-1}) \end{aligned} \tag{3.39}$$

It can be verified that if we apply the oscillatory stress $\sigma(t) = \sigma_0 \sin(\omega t)$ instead of an oscillatory strain, the equilibrium condition $k\varepsilon(t)^e = \sigma(t)$, together with the evolution law in (3.24) with $L(t = 0) = L_0$, we obtain the same expressions of the dynamic moduli and the phase angle for $|\sigma_0/k| << 1$. By comparing the expressions in (3.39) with the relations in Table 3.1, we have that again, the active element behaves like the Maxwell element but replacing γ by $k/\eta = \tau^{-1}$.

Chapter 4

Porous-based rheological model for tissue fluidisation

4.1 Introduction

Cells are complex structures consisting of a wide number of binding proteins and other solid and fluid constituents. Due to a reduction of the phase angle upon stretching, it is considered that cells undergo fluidisation. We here extend the rheological model with an evolving active length for mimicking such softening and fluidisation process, which is also able to simulate the eventual recovery upon removal of the applied stretch.

Material fluidisation has been associated to apoptotic events and cell division [Ranft et al., 2008]. We instead restrict our attention to tissues with a constant number of cells and no connectivity changes, as it has been observed in *in vitro* experiments [Trepat et al., 2007, Krishnan et al., 2009]. Other experiments have revealed the reversibility of the softening and stiffening *during* a stretch cycle, and explained this behaviour through the presence of motor proteins [Chaudhuri et al., 2007] or the geometrical orientation of the fibers [Kollmannsberger and Fabry, 2009]. We focus instead on the delayed recovery of the material properties *after* the stretch cycle. This response has been already explained in the context of soft glassy framework using a Glassy Wormlike Chain model (GWLC) [Gardel et al., 2004], which has been extended for modelling material softening [Wolff et al., 2012]. These authors propose a model based on a non-linear form of the GWLC model based on crosslinked biopolymer networks, where bond fraction kinetics is accounted for.

Since we aim to implement the softening behaviour on arbitrary multicellular systems, and include the resulting rheological law on general cell topologies, we present here an alternative model based on an extension of a Maxwell-like law presented in the previous chapter, which uses an adaptive resting length [Muñoz and Albo, 2013]. We complement the model with a suitable evolution of an additional variable that represents the polymer density. This porous-like variable

mediates the mechanical response of the cell and controls the effective stress that cells can exert, in a similar manner to the damage variable in damage mechanics. The modulation of softening with damage-like variables has already been formulated in [Peña, 2011a,b]. Our model bridges the delayed softening with cell porosity.

The relevance of porosity in living tissues has already been considered in early models of cardiac muscle [Yang and Taber, 1991]. More recently, it has been applied in [Wang and Hong, 2012] for polymeric materials, or when assuming a biphasic material consisting of a porous elastic solid mesh [Moeendarbary et al., 2013]. Other continuous models for rubbers took into account the fraction of soft versus stiff material or molecular chain density [Qi and Boyce, 2004], or the fiber and matrix contributions through internal variables [Calvo et al., 2011]. These phase transition or damage based models consider only irreversible softening, which is not the case in the experiments modelled here.

We will present first in Section 4.2 a summary of the experimental findings, and then describe the extension of the model in the context of continuum mechanics. In order to reduce the number of tensorial parameters that the continuum description involves, we will recast the same ideas for one-dimensional elasticity in Chapter 3, which will allow us to implement the theory in a truss system where each bar represents a cell-cell interaction. The comparison and fitting of the model with the experimental results is carried out in Section 4.5, where a single elements and a whole truss system is considered.

4.2 Experimental set-up

In 2007, a novel experimental system is developed for measuring the viscoelastic behaviour of a tissues when subject to a short stretch cycle [Trepat et al., 2007]. The adherent human airway smooth muscle (HASM) cells were cultured onto flexible elastic substrate, which was stretched for 4 second, and returning to a zero strain, as illustrated in Figure 4.1. After the stretching, small local oscillatory strains were applied on magnetic beads attached to the tissue during 1000 seconds with frequency $2\pi\omega = 0.75Hz$ in order to measure the evolution of the storage and loss modulus, G' and G''. The authors reported that the living cell under stretch promptly fluidises and then slowly re-solidises.

The complex modulus of the cells was computed using optical magnetic twisting cytometry before and after application of the single transient stretch. The stiffness after stretch relative to stiffness of the same cell immediately before was denoted G'_n.

As shown in Figure 4.2a, when no stretch was applied, this fractional stiffness did not change, but immediately after cessation of a single transient stretch, G'_n

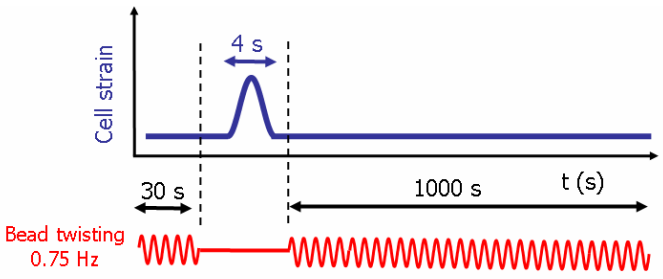

Figure 4.1: Experimental protocol for rheology

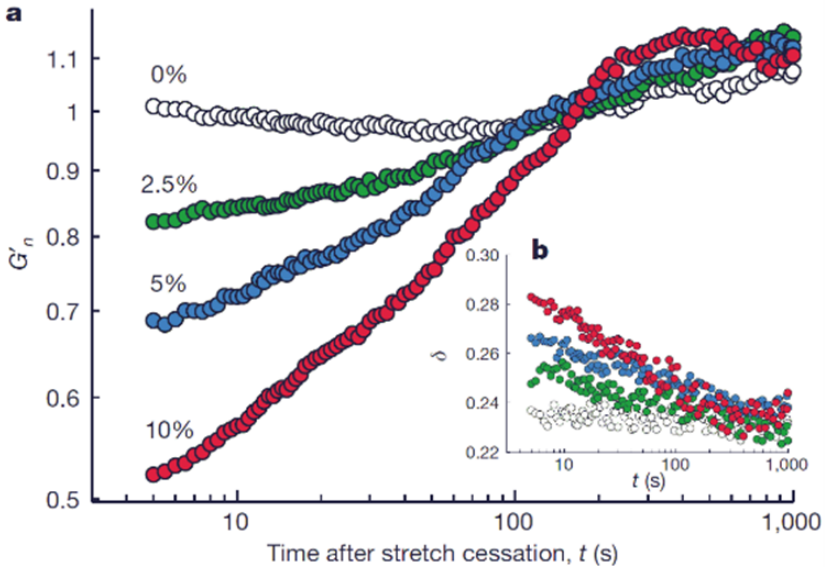

Figure 4.2: (a) Evolution of normalized G_n of HASM cells after a single transient stretch of 0% (no stretch, open circles), 2.5% (green), 5% (blue) and 10% (red). (b) Evolution of the phase angle (radian) after stretch application (from [Trepat et al., 2007]).

promptly decreased and then slowly recovered. The phase angle $\delta = \tan^{-1}(G''/G')$ promptly increased and then slowly recovered (Fig 4.2b), where for a hookean solid $\delta = 0$ and for a newtonian fluid $\delta = \pi/2$. In the living cell $0.15 < \delta < 0.50$, thus placing the living cell closer to the solid-like state. These experiments will be here referred to as fluidisation process. In order to obtain the mentioned characteristics of the living cells, a rheological model will be present in the following sections.

4.3 Continuum model

The explicit modelling of the filaments in the cytoskeleton would render the resulting model computationally expensive if not prohibitive for analysing multicellular systems. For this reason, we idealise first in this section the observed domain $\Omega \in \mathbb{R}^3$ as a continuum, whose shape is the result of an active and an elastic deformation. Computationally, we express these two contributions by decomposing the deformation gradient [Muñoz et al., 2007], where each material point $\boldsymbol{X}_0 \in \Omega_0$ moves to a new position $\boldsymbol{x} \in \Omega(t) \in \mathbb{R}^3$. The total deformation gradient $\boldsymbol{F} = \frac{\partial \boldsymbol{x}}{\partial \boldsymbol{X}_0}$ is decomposed in an active and an elastic deformation, respectively denoted by $\boldsymbol{F}^a = \frac{\partial \boldsymbol{x}^a}{\partial \boldsymbol{X}_0}$ and $\boldsymbol{F}^e = \frac{\partial \boldsymbol{x}}{\partial \boldsymbol{x}^a}$, and such that $\boldsymbol{F} = \boldsymbol{F}^e \boldsymbol{F}^a$. The vector $\boldsymbol{x}^a \in \Omega^a$ denotes the position of the material points prior to any elastic deformation, with Ω^a a relaxed configuration, not necessarily observed or compatible with the material impenetrability assumption. We use the configuration Ω^a to represent the remodelling and internal reorganisation of the biologically active material.

The description of the cell activity is represented in this chapter as a function of a parameter P that represents the polymer porosity or void content. The resulting model is based on three basic ingredients:

- Mechanical equilibrium of the observed domain Ω.
- Evolution law for the reference configuration Ω^a, as a function of the elastic deformation $\boldsymbol{F}^e$ and polymer porosity P.
- Evolution law for the polymer porosity P.

The second ingredient reflects the ability of cells to adapt to the imposed deformations, while the third ingredient aims to mimic the evolution of the network without explicitly representing the elements of the cytoskeleton. We will next detail each one of the three ingredients given above.

4.3.1 Mechanical equilibrium

Similarly to the damage models, we consider a free energy function which is mediated through a damage-like parameter D,

$$U(\boldsymbol{C}, D) = (1 - D)\, U^e(\boldsymbol{C}). \tag{4.1}$$

where $U^e(\boldsymbol{C})$ is the strain energy function. The latter is assumed to depend on the right Cauchy Green tensor $\boldsymbol{C} = \boldsymbol{F}^{eT} \boldsymbol{F}^e$, with $\boldsymbol{F}^e = \frac{\partial \boldsymbol{x}}{\partial \boldsymbol{x}^a}$ the deformation gradient tensor. The parameter D depends on a porosity variable P as,

$$D = c_1 \frac{P - P_0}{P_0}. \tag{4.2}$$

with c_1 a positive material constant. Variable P represents the porosity or void content of the cross-linked network of the cytoskeleton, and P_0 is a reference

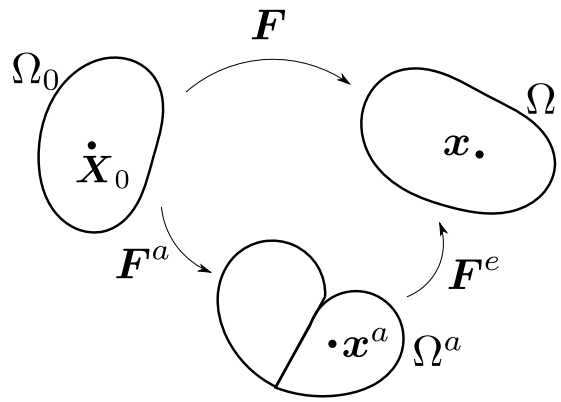

Figure 4.3: Schematic of the multiplicative decomposition of the total deformation gradient, $\boldsymbol{F}$, in a growth component, $\boldsymbol{F}^a$, and elastic component, $\boldsymbol{F}^e$, i.e. $\boldsymbol{F} = \boldsymbol{F}^e\boldsymbol{F}^a$.

value. P may be interpreted as the inverse of the polymer density or entanglement of the cytoskeleton. We will assume that both P and P_0 are non-negative, i.e. $P, P_0 \geq 0$, and also that $0 \leq P \leq P_0(1 + c_1)/c_1$. Therefore, and unlike damage models, D may have negative values, and $-c_1 \leq D \leq 1$. The case $D \leq 0$ represents stiffening due to increased entanglement or increase in polymer density.

The equilibrium equations of the continuum Ω are given by Cauchy equation [Holzapfel, 2000]:

$$\nabla \cdot ((J^e)^{-1}\boldsymbol{F}^e\boldsymbol{S}\boldsymbol{F}^{eT}) = \boldsymbol{0}, \forall x \in \Omega, \tag{4.3}$$

where $\boldsymbol{S}$ is the second Piola-Kirchhoff stress tensor, and $J^e = \det(\boldsymbol{F}^e)$. The relation between $\boldsymbol{S}$ and $U(\boldsymbol{C}, D)$ follows from the Clausius-Duhem inequality [Marsden and Hughes, 1994],

$$\frac{1}{2}\boldsymbol{S} : \dot{\boldsymbol{C}} - \dot{U} \geq 0.$$

The rate of free energy can be attributed the variations of P and $\boldsymbol{C}$, but for living materials, also to other energy sources such as production of ATP, which are here denoted by s. In this case, the inequality above implies that,

$$\boldsymbol{S} = 2\frac{\partial U}{\partial \boldsymbol{C}} = 2(1 - D)\frac{\partial U^e}{\partial \boldsymbol{C}}$$
$$s + \frac{\partial U}{\partial P}\dot{P} \leq 0.$$

Note that from the expression of U in (4.1), (4.2), the previous inequality reads,

$$c_1\frac{\dot{P}}{P_0}U^e(\boldsymbol{C}) \geq s.$$

Since $c_1, P_0 > 0$ and $U^e(\boldsymbol{C}) \geq 0$, we have that $\dot{P} \geq s$ when the tissue is deformed ($U^e > 0$). For a dead material ($s = 0$), P may only increase, but for a living material, this is not necessarily so, and $\dot{P}$ can change sign. We will propose an evolution law for P in Section 4.3.3 that actually allows for positive and negative rates of porosity.

The variations on the stress response has effects on the strain energy, which is modulated by this porous-like variable. We assume that the available energy of the active material ("metabolic" energy) is unbounded [Cox and Smith, 2014], so that cell activity is energetically unconstrained.

4.3.2 Evolution of active configuration

The actin cytoskeleton is a composite intracellular biopolymer network made of actin filaments that can actively vary their length and entanglement. Since these changes may strongly affect cellular rheology, our model includes an evolution law for the active deformation of the polymers. This deformation may be due to multiple phenomena such as transient domain unfolding [Fantner et al., 2006], remodelling of cytoskeletal filaments [Chen et al., 2010], un/rebinding of sticky contacts [Semmrich et al., 2007], activity of crosslinking molecules [Lieleg et al., 2009, Xu et al., 2000], forming of actin-myosin cross bridges [Kollmannsberger and Fabry, 2009], or (de)polymerisation [Azevedo et al., 2011, Ma et al., 2009].

The evolution law in equation (3.24) of Section 3.3 is here rewritten in terms of active deformation $\boldsymbol{E}^a$. We will not detail the specific causes behind the changes in the polymer lengths, which we mechanically identify with a time-varying active deformation $\boldsymbol{E}^a$ that satisfies the following evolution law:

$$\dot{\boldsymbol{E}}^a = \boldsymbol{\gamma} : \boldsymbol{E}^e, \tag{4.4}$$

with $\boldsymbol{E}^e$ the Green-Lagrange elastic strain tensor. Tensor $\boldsymbol{\gamma}$ represents the resistance of the network to adapt its relaxed configuration to the current elastic strain and will be called the *remodelling rate*.

The physical picture behind the evolution law in (4.4) is similar to the one in Figure 3.3 introduced in Section 3.3, where a network of cross-linked actin filaments (Figure 4.4a) subjected to a macroscopic strain stretches mainly as a result of two combined phenomena: (i) a reversible (elastic) deformation and a (ii) non-reversible remodelling and lengthening, due to the (de)polymerisation process of the filaments.

In addition, filament density has been also identified as an important parameter in mechanical weakening [Semmrich et al., 2008]. This dependence is mathematically described with the following simple relationship,

$$\boldsymbol{\gamma} = P\boldsymbol{\gamma}_0, \tag{4.5}$$

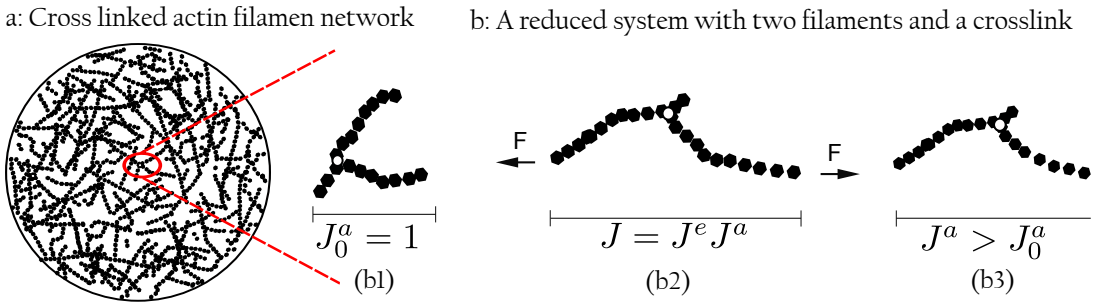

Figure 4.4: (a) Schematic of network of actin filaments connected by flexible cross-links. (b) Schematic of strain induced changes in the active deformation $J^a = det(\boldsymbol{F}^a)$ of a reduced system with two filaments and a cross-link (white circle). (b1) Initial configuration with active deformation $J_0^a = 1$. (b2) Configuration under an applied load. (b3) New unstrained configuration with modified active deformation $J^a > J_0^a$.

where $\boldsymbol{\gamma}_0$ is considered a constant remodelling rate. Figure 4.5 illustrates this dependence. As the porosity P increases (or cell density decreases), the cytoskeleton adapts more easily its resting configuration, and conversely, as the porosity decreases, more filaments resist to adapt the resting configuration.

The relations in (4.4)-(4.5) are simple linear laws, but without further experimental evidence, it seems as yet unnecessary to test more complicated relations. The main implications of the proposed laws are,

(i) No internal remodelling occurs if the filament is not subjected to stretch,

(ii) The filament tends to reduce the amount of elastic strain energy.

(iii) The remodelling rate increases as the polymer density and entanglement decreases.

4.3.3 Cell porosity evolution

Since we do not aim to explicitly model the polymer network, but to characterise this network through its porosity and resting length, we propose here the following relation for the evolution of P,

$$\dot{P} = c_2^{\pm} \left(P_0 - \frac{P}{(J^a)^{c_3}} \right), \tag{4.6}$$

with $J^a = det(\boldsymbol{F}^a)$, and P_0 a reference homeostatic value of the porosity, at which no further changes on P are induced. Equation (4.6) represents a self-regulation of the void content, where the material constants $c_2^{\pm}$ and c_3 determine how strongly this self-regulation takes place, and how strongly $\dot{P}$ depends on the active deformation J^a. We further hypothesise that $c_2^{\pm}$ may take different values

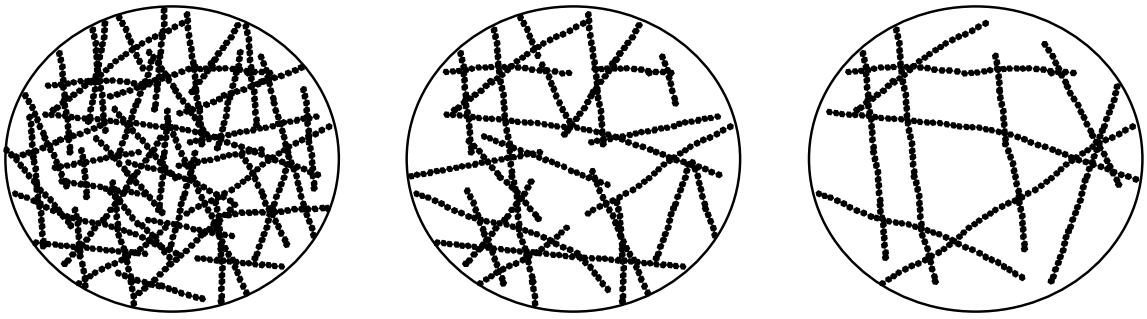

(a) $J^a < 1$, $P < P_0$, $D < 0$, $\boldsymbol{\gamma} < P_0\boldsymbol{\gamma}_0$

(b) $J^a = 1$, $P = P_0$, $D = 0$, $\boldsymbol{\gamma} = P_0\boldsymbol{\gamma}_0$

(c) $J^a > 1$, $P > P_0$, $D > 0$, $\boldsymbol{\gamma} > P_0\boldsymbol{\gamma}_0$

Figure 4.5: Physical illustration of equations (4.2), (4.5) and (4.6): (a) by decreasing the resting volume ($J^a < 1$), the material stiffens and the porosity decreases ($\dot{P} < 0$) due to the reduction of J^a, and eventually increases when $P_0 - P/(J^a)^{c_3} > 0$. (b) Initial configuration of a system of actin filaments with resting volume equal to $J_0^a = J_0 = 1 = det(\boldsymbol{F}^e)$. (c) When the resting volume increases ($J^a > 1$), the material softens and the porosity increases ($\dot{P} > 0$), and eventually diminishes when $P_0 - P/(J^a)^{c_3} < 0$.

dependent on whether P is increasing ($c_2^{\pm} = c_2^+$) or P is decreasing ($c_2^{\pm} = c_2^-$), with $c_2^+ > c_2^-$. The physical hypotheses in (4.6) are the following:

- Networks with larger resting configurations induce an increase of the porosity (filaments tend to stay farther from each other) while smaller resting domains render the polymeric network denser. This is illustrated in Figure 4.5. The dependence of $\dot{P}$ on J^a is plotted in Figure 4.6a.

- When the porosity is below the homeostatic state $P_0(J^a)^{c_3}$, the porosity will tend to increase, and vice-versa. Figure 4.6b illustrates this dependence.

- Unsymmetrical polymer remodelling: porosity recovers its reference value $P_0(J^a)^{c_3}$ much easily when P is increasing than when it is decreasing.

4.3.4 Summary of the model

The continuum model described so far can be summarised in the three equations (4.3), (4.4) and (4.6), which may be gathered in a system of PDEs:

$$\begin{cases} \nabla \cdot \left((J^e)^{-1} \boldsymbol{F}^e \boldsymbol{S} \boldsymbol{F}^{eT} \right) = \boldsymbol{0}, \forall \boldsymbol{x} \in \Omega \\ \dot{\boldsymbol{E}}^a = P \boldsymbol{\gamma}_0 : \boldsymbol{E}^e \\ \dot{P} = c_2^{\pm} \left(P_0 - \frac{P}{(J^a)^{c_3}} \right) \end{cases} \tag{4.7}$$

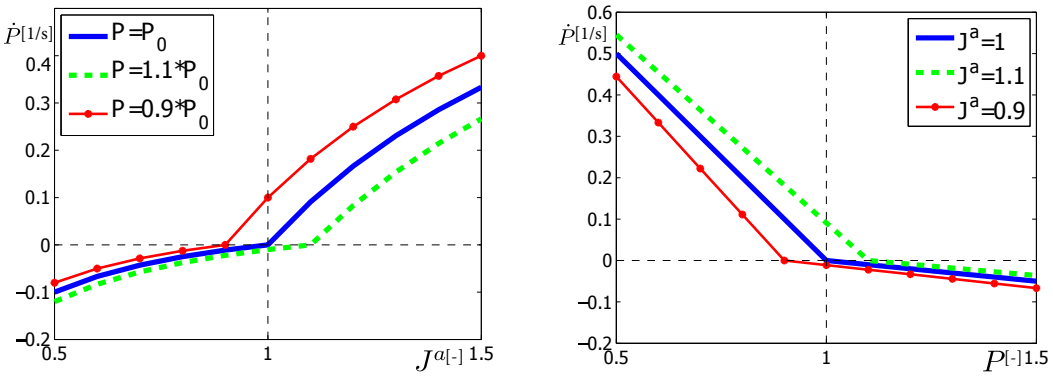

Figure 4.6: Evolution of P according to equation (4.6) with $c_3 = 1$, and $c_2^+/c_2^- = 10$. (a) Rate of cell porosity, $\dot{P}$, against the resting J^a, for $P_0 = 1$, and different values of P. $\dot{P}$ decreases when the resting volume decreases ($J^a < 1$). (b) Rate of cell porosity, $\dot{P}$, as a function of P for $P_0 = 1$, and different values of J^a.

where

$$\boldsymbol{S} = 2\frac{\partial U}{\partial \boldsymbol{C}} \quad , \quad U(\boldsymbol{F}) = (1-D)\,U^e(\boldsymbol{F}) \quad , \quad D = c_1\frac{P-P_0}{P_0} \tag{4.8}$$

According to the expression of the damage factor $1-D = 1+c_1-c_1\frac{P}{P_0}$ and the evolution of $\dot{\boldsymbol{E}}^a$, if the porosity increases while keeping the elastic deformation $\boldsymbol{E}^e$ constant , the stress $\boldsymbol{S}$ will decrease but the active strains $\boldsymbol{E}^a$ will increase. Indeed, and as depicted in Figure 4.5c, if the density of filaments is lower, then the total stress that the cell can bear is also lower, and the cell should adapt more easily to the current elastic deformation. Conversely, a reduction in cell porosity causes an increase in the effective stresses and a decrease of the active strains (see Figure 4.5a).

We note that we are not modelling fluid flow in the porous biological material, and so this is not a poroelastic model. However, porosity is taken into account and modulates the effective stress, but without considering the transfer of stresses between fluid and solid phases.

The formulation in (4.7) formally satisfies the physical hypothesis in (i), (ii) and (iii), but it has no straight forward implementation. The values in the fourth-order tensor $\boldsymbol{\gamma}_{ijkl}$, which represent the rate of a given active strain in the components ij when subjected to an elastic strain along kl component cannot be easily measured experimentally. For this reason we present in the next section a one dimensional version that can be implemented in a truss model of the tissue. The bar elements to be used next, do not represent individual filaments, but an element that carries the net force between two connected cells.

4.4 Computational implementation on cell-centred model

The equations of the continuum model described in the previous section are here adapted to the cell-centred model described in Chapter 2 and in [Mosaffa et al., 2015] in order to simplify the evolution law for $\dot{\boldsymbol{E}}^a$. By including the porous-based rheological law presented here, we aim to extend the cell-centred model with fluidisation capabilities.

4.4.1 Equilibrium equations

We remind that in the cell-centred model the connection between two cell centres is defined by the presence of a one-dimensional bar element. The decomposition of the deformation gradient is now rewritten as a function of the current length of a bar element between cells i and j, denoted by $l^{ij} = ||\boldsymbol{x}^j - \boldsymbol{x}^i|$, its active (or relaxed length) L^{ij}, and its initial length $L_0^{ij} = ||\boldsymbol{X}_0^j - \boldsymbol{X}_0^i|$. Note that the positions $\boldsymbol{x}^a$ after the active deformation will not be computed, and just the active length L^{ij} will be included in the model.

In parallel with the elastic potential in Section 4.3.1, we define the following elastic potential,

$$U^{ij} = \frac{1}{2}k\left(1 - c_1\frac{P^{ij} - P_0}{P_0}\right)\left(\varepsilon^{e,ij}\right)^2, \tag{4.9}$$

where $\varepsilon^{e,ij}$ is the elastic strain between cells i and j along direction,

$$\boldsymbol{e}^{ij} = (\boldsymbol{x}^j - \boldsymbol{x}^j)/l^{ij},$$

and k represents the stiffness of the filament. The factor $c_1\frac{P^{ij}-P_0}{P_0}$ represents the damage-like variable, which modulates the elastic energy through the porosity variable P^{ij}. In our implementation we will use the following strain measure,

$$\varepsilon^{e,ij} = \frac{l^{ij} - L^{ij}}{L^{ij}}. \tag{4.10}$$

The elastic force along the direction $\boldsymbol{x}^i - \boldsymbol{x}^j$ is derived from the gradient of the elastic potential U^{ij} for a constant resting length L^{ij} as,

$$\mathbf{g}^{ij} = k\left(1 - c_1\frac{P^{ij} - P_0}{P_0}\right)\varepsilon^{e,ij}\boldsymbol{e}^{ij}. \tag{4.11}$$

The global equilibrium of the system is achieved by equalising the resultant of all the elastic forces at each cell-centre to zero, that is,

$$\sum_j \mathbf{g}^{ij} = \mathbf{0}, \quad i = 1, \ldots, N. \tag{4.12}$$

4.4.2 Active length evolution

The evolution law of the active strain in (4.4) is here rewritten in terms of the active length variable L as:

$$\dot{L}^{ij} = P^{ij}\gamma_0 \varepsilon^e L^{ij} = P^{ij}\gamma_0 (l^{ij} - L^{ij}). \tag{4.13}$$

The tensor like character of the active deformations is thus replaced by a scalar lengthening rate $\dot{L}^{ij}$, which is regulated by a scalar remodelling rate, $\gamma^{ij} = P^{ij}\gamma_0$, not necessary the same for each element ij. This elemental internal remodelling rate of the cytoskeleton has the same meaning as its tensor counterpart, but along the direction of the cell-cell contact. We will consider the value of γ_0 as constant and homogeneous throughout the cellular system.

4.4.3 Porosity evolution

The evolution for the proposity takes in the bar system the following form,

$$\dot{P}^{ij} = c_2^{\pm} \left(P_0 - \frac{P^{ij}}{\left(L^{ij}/L_0^{ij}\right)^{c_3}} \right). \tag{4.14}$$

This corresponds to equation 4.6, but replacing J^a by its one-dimensional counterpart L/L_0.

4.4.4 Summary of the computational model

The particle based model is described by gathering the three equations in (4.12), (4.13) and (4.14), which may be jointly written as,

$$\boldsymbol{f}(\boldsymbol{x}, L^a, P) = \boldsymbol{0}, \tag{4.15}$$

with,

$$\boldsymbol{f}(\boldsymbol{x}, L^a, P) = \left\{ \begin{array}{ll} \sum_j k \frac{1}{L^{ij}} \left(1 - c_1 \frac{P^{ij} - P_0}{P_0}\right) \varepsilon^{e,ij} \boldsymbol{e}^{ij}, & i = 1, \ldots, N \\ \dot{L}^{ij} - \gamma_0 P^{ij} \varepsilon^{e,ij}, & ij = 1, \ldots, N_e \\ \dot{P}^{ij} - c_2^{\pm} \left(P_0 - \frac{P^{ij}}{\left(L^{ij}/L_0^{ij}\right)^{c_3}} \right), & ij = 1, \ldots, N_e \end{array} \right\}. \tag{4.16}$$

After replacing the continuum model by a particle based model, we have turned the system of PDEs in (4.7) into the system of ODEs given above. This system is discretised on time in the following section using a weighting parameter θ. The resulting non-linear system of equations that allows us to find the new set of $N \times 2 \times N_e$ unknowns: $\boldsymbol{x}^i_{n+1}$, L^{ij}_{n+1} and P^{ij}_{n+1} is solved using a Newton-Raphson scheme.

Due to the elemental character of the active lengths and porosities, these variables can be statically condensed, giving rise to a non-linear system of solely N unknowns, $\boldsymbol{x}^1, \ldots, \boldsymbol{x}^N$. Next section explains the static condensation procedure and the system of linear equations to be solved at each Newton-Raphson iteration.

4.4.5 Time discretisation and static condensation

The time discretisation of the evolution laws in (4.13) and (4.14) using a θ-scheme yield

$$L^{ij}_{n+1} = L^{ij}_n + \Delta t \gamma_0 P^{ij}_{n+\theta}(l^{ij}_{n+\theta} - L^{ij}_{n+\theta})$$
$$P^{ij}_{n+1} = P^{ij}_n + \Delta t c_2^{\pm}\left(P_0 - \frac{P^{ij}_{n+\theta}}{(L^{ij}_{n+\theta}/L^{ij}_0)^{c_3}}\right),$$

with $(\bullet)_{n+\theta} = (1-\theta)(\bullet)_n + \theta(\bullet)_{n+1}$. At each time-step t_{n+1}, the set of unknowns $\boldsymbol{x}_{n+1} = \{\boldsymbol{x}^1_{n+1}, \ldots, \boldsymbol{x}^N_{n+1}\}$, $P_{n+1} = \{P^1_{n+1}, \ldots, P^{N_e}_{n+1}\}$ and $L_{n+1} = \{L^1_{n+1}, \ldots, L^{N_e}\}$ may be found by solving the following system of equations,

$$\boldsymbol{f}(\boldsymbol{x}_{n+1}, L_{n+1}, P_{n+1}) = \boldsymbol{0}$$

with,

$$\boldsymbol{f}(\boldsymbol{x}_{n+1}, L_{n+1}, P_{n+1}) = \left\{ \begin{array}{ll} \sum_j k \frac{1}{L^{ij}_{n+1}}\left(1 - c_1 \frac{P^{ij}_{n+1} - P_0}{P_0}\right)\varepsilon^{e,ij}_{n+1}\boldsymbol{e}^{ij}_{n+1}, & i = 1, \ldots, N \\ L^{ij}_{n+1} - L^{ij}_n - \Delta t \gamma P^{ij}_{n+\theta}(l^{ij}_{n+\theta} - L^{ij}_{n+\theta}), & ij = 1, \ldots, N_e \\ P^{ij}_{n+1} - P^{ij}_n - \Delta t c_2^{\pm}\left(P_0 - \frac{P^{ij}_{n+\theta}}{\left(L^{ij}_{n+\theta}/L_0\right)^{c_3}}\right), & ij = 1, \ldots, N_e \end{array} \right\}. \tag{4.17}$$

The solution of the system of equations in (4.17) may be found by using a full Newton-Raphson method. In this case, at each iteration k, the system of linear equations reads,

$$\mathbf{K}^k \left\{ \begin{array}{c} \delta\boldsymbol{x} \\ \delta L \\ \delta P \end{array} \right\} = - \left\{ \begin{array}{c} \boldsymbol{f}_x \\ \boldsymbol{f}_L \\ \boldsymbol{f}_P \end{array} \right\}^k_{n+1}. \tag{4.18}$$

The vectors $\boldsymbol{f}_x$, $\boldsymbol{f}_L$ and $\boldsymbol{f}_P$ denote the block of equations in vector $\boldsymbol{f}$ related to the mechanical equilibrium and the evolutions laws for L and P. The Jacobian matrix is decomposed as follows,

$$\mathbf{K} = \left[\begin{array}{ccc} \mathbf{K}_{xx} & \mathbf{K}_{xL} & \mathbf{K}_{xP} \\ \mathbf{K}_{Lx} & \mathbf{K}_{LL} & \mathbf{K}_{LP} \\ \mathbf{K}_{Px} & \mathbf{K}_{PL} & \mathbf{K}_{PP} \end{array} \right] = \left\{ \begin{array}{ccc} \partial_{\boldsymbol{x}}\boldsymbol{f}_x & \partial_L \boldsymbol{f}_x & \partial_P \boldsymbol{f}_x \\ \partial_{\boldsymbol{x}}\boldsymbol{f}_L & \partial_L \boldsymbol{f}_L & \partial_P \boldsymbol{f}_L \\ \partial_{\boldsymbol{x}}\boldsymbol{f}_P & \partial_L \boldsymbol{f}_P & \partial_P \boldsymbol{f}_P \end{array} \right\}. \tag{4.19}$$

From the second and third block of rows in equation (4.18), the variables δL and δP can be computed as follow,

$$\left\{ \begin{array}{c} \delta L \\ \delta P \end{array} \right\} = -\mathbf{J}^{-1}_{LP}\left(\boldsymbol{f}_{LP} + \left[\begin{array}{c} \mathbf{K}_{Lx} \\ \mathbf{K}_{Px} \end{array} \right] \delta\boldsymbol{x}\right), \tag{4.20}$$

with $\mathbf{J}_{LP} = \begin{bmatrix} \mathbf{K}_{LL} & \mathbf{K}_{LP} \\ \mathbf{K}_{PL} & \mathbf{K}_{PP} \end{bmatrix}$ and $\boldsymbol{f}_{LP} = \begin{Bmatrix} \boldsymbol{f}_L \\ \boldsymbol{f}_P \end{Bmatrix}$. Replacing the expression in (4.20) back into (4.18), yields the following reduced system of equations:

$$\hat{\mathbf{K}}_x \delta \boldsymbol{x} = -\hat{\boldsymbol{f}}_x, \tag{4.21}$$

where the vector $\hat{\boldsymbol{f}}_x$ and the Jacobian $\hat{\mathbf{K}}_x$ are given by,

$$\begin{aligned} \hat{\boldsymbol{f}}_x &= \boldsymbol{f}_x - \begin{bmatrix} \mathbf{K}_{xL} & \mathbf{K}_{xp} \end{bmatrix} \mathbf{J}_{LP}^{-1} \boldsymbol{f}_{LP} \\ \hat{\mathbf{K}}_x &= \mathbf{K}_{xx} - \begin{bmatrix} \mathbf{K}_{xL} & \mathbf{K}_{xp} \end{bmatrix} \mathbf{J}_{LP}^{-1} \begin{bmatrix} \mathbf{K}_{Lx} \\ \mathbf{K}_{px} \end{bmatrix}. \end{aligned} \tag{4.22}$$

The condensed system of equation in (4.21) can be now solved by Newton-Raphson method. Note that since variables L and P are elemental, matrix $\mathbf{J}_{LP}$ is formed by N_e uncoupled matrices with dimensions 2×2, and therefore the products in (4.22) are computationally cheap.

4.5 Simulation results

4.5.1 Tests with one bar element

In order to validate our model, we have simulated the fluidisation process by applying the stretch history given in Figure 4.7 to a single bar element.

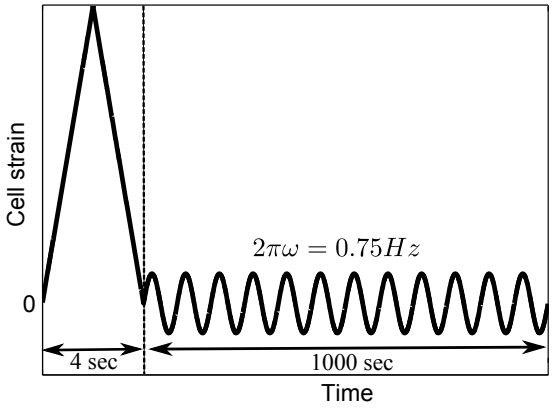

Figure 4.7: Schematic description of cell stretching. Cells were subjected to a single transient stretch during 4 seconds and returning to zero strain and then applying smaller oscillatory strain of 1000 seconds with frequency $\omega = 0.75Hz$.

The plots in Figure 4.8 show the evolutions of the resting length and the porosity. While the trend of the former follows the evolution of the imposed displacement, the latter has a much slower decreasing curve. Indeed, according to equation (4.13), the resting length adapts to the imposed strain, while in view of equation (4.6), the porosity P tends to decrease and equalise the reference value $P_0 = 1$ when $J^a = 1$. However, due to the smaller value of c_2^-, at much lower rate than during the approximately first 2 seconds, where c_2^+ is used and

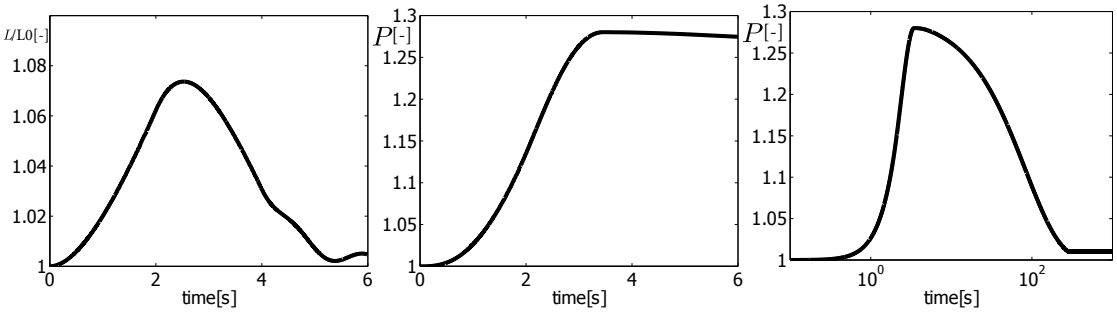

(a) (b) (c)

Figure 4.8: (a) Evolution of resting length L. (b)-(c) Evolution of porosity P in unscaled time units (b) and logarithmic units (c) after stretch application on a single element of $\varepsilon = 10\%$.

$\dot{P} > 0$.

After cessation the transient stretch, the phase angle δ and the stiffness G' are computed as follows,

$$\delta = \tan^{-1}(G''/G') \qquad G' = \frac{\sigma_0}{\varepsilon_0}\cos(\delta) \tag{4.23}$$

with G' and G'' the storage and loss modulus, respectively, and with σ_0 and ε_0 the maximum values of the stress and strain signals. Figure 4.9 illustrates the experimental data of the phase angle δ (Figure 4.9, a) and the stiffness G' (Figure 4.9, b) related to 5% (red circles) and 10% (green circles) of the strain.

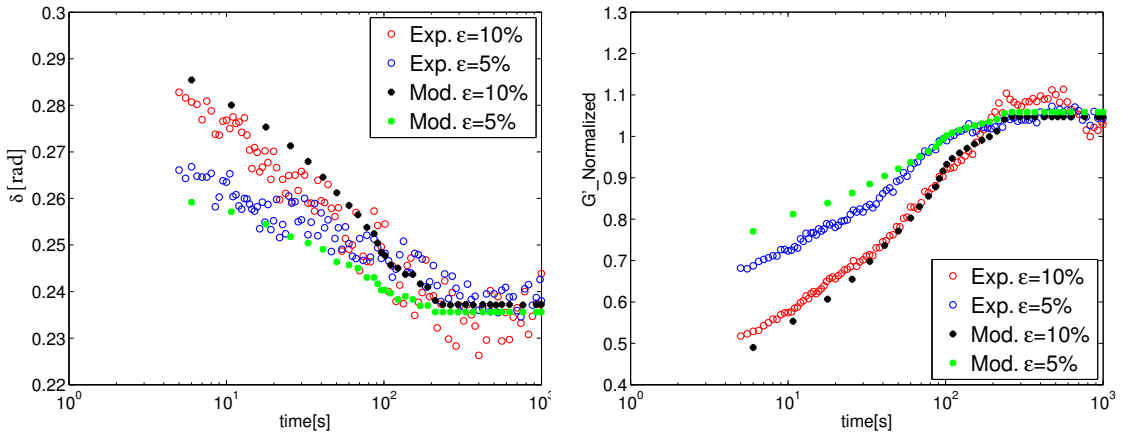

(a) (b)

Figure 4.9: Evolution of the (a) phase angle δ and (b) stored modulus G' after stretch application on a single element of $\varepsilon = 10\%$ and $\varepsilon = 5\%$. Circles depict the experimental data, while $\times$ and $+$ crosses represent the results of the numerical simulation.

4.5.2 Fitting material parameters

The parameters of the model $\boldsymbol{p} = (k, \gamma_0, c_1, c_2^{\pm}, c_3)$ have been fitted using a least square procedure adapted from the Matlab function `lsqcurvefit`, for the 5% and 10% of the strain, by minimising the following error E,

$$E = \min_{\boldsymbol{p}} \sum_i (\delta_{num10\%}(\boldsymbol{p})_i - \delta(exp_{10\%})_i + (G'_{num10\%}(\boldsymbol{p})_i - G'(exp_{10\%})_i + (\delta_{num5\%}(\boldsymbol{p})_i - \delta(exp_{5\%})_i + (G'_{num5\%}(\boldsymbol{p})_i - G'(exp_{5\%})_i,$$

where $\delta_{num10\%}(\boldsymbol{p})$ and $G'_{num10\%}(\boldsymbol{p})$ are numerical values of phase angle δ and stiffness G' for 10% of strain, respectively and $\delta(exp_{10\%})$ and $G'(exp_{10\%})$ are experimental values of phase angle δ and stiffness G' for 10% of strain. The values of $\delta_{num5\%}(\boldsymbol{p})$ and $G'_{num5\%}(\boldsymbol{p})$ are numerical values of phase angle δ and stiffness G' for 5% of strain, respectively and $\delta(exp_{5\%})$ and $G'(exp_{5\%})$ are experimental values of phase angle δ and stiffness G' for 5% of strain.

As shown in Figure 4.9, the model predictions using the fit values (k, γ_0, c_1, c_2^+, c_2^-, c_3)=(1.13, 1.119, 2.02, 0.012, 0.0012, 4.75) follow the same trends of the experimental data. The phase angle δ increased after the single transient stretch and then slowly recovered. Instead, stored modulus G' decreased after the single transient stretch and then slowly recovered after 20 minutes, approximately. The damage-like variable D in equation (4.8), which depends on the porosity P, is responsible for modulating this fluidisation effect.

4.5.3 Multicellular system

The same stretch history was applied to the multicellular system shown in Figure 4.10, where the bottom side was kept fully constrained, while the up side followed a displacement history producing the strain evolution in Figure 4.7. The initial positions of the nuclei, which is shown in Figure 4.10, was obtained by pre-stressing a regular mesh of cells.

The phase angle δ and the stiffness G' were computed after cessation of the single transient stretch. As in the single element, G' was defined as the cell stiffness after stretch relative to the initial stiffness. It can be observed in Figure 4.11 that using a similar set of parameters, in this case (k, γ_0, c_1, c_2^+, c_2^-, c_3)=(0.97, 1.17, 2.13, 0.012, 0.0012, 4.00), the two curves corresponding to 5% and 10% stretch can be recovered. The trends of the porosity and resting length were similar to those of the single element, but remarkably so on the vertical elements of the network, which are those most affected by the stretching.

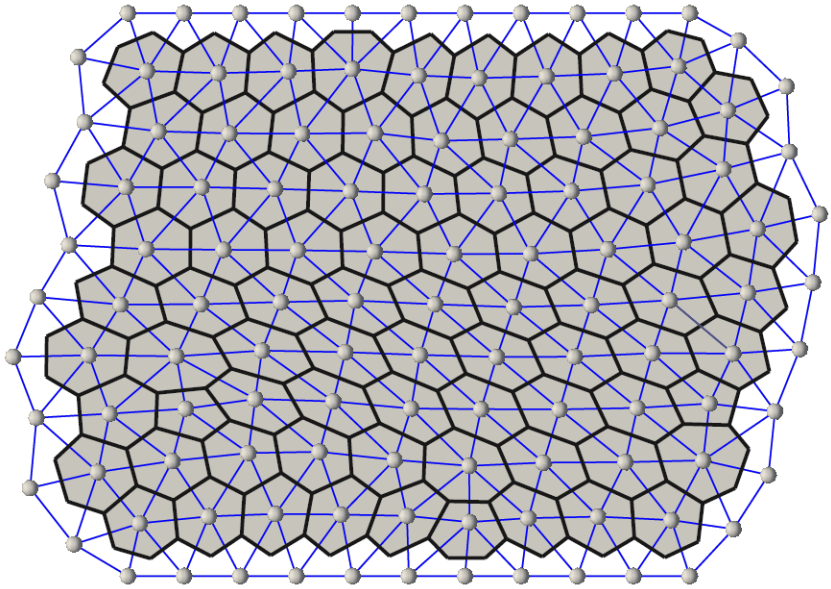

Figure 4.10: Multicellular system: spheres represent cell centre and thin lines cell-cell contacts. Thicker lines show associated cell boundaries.

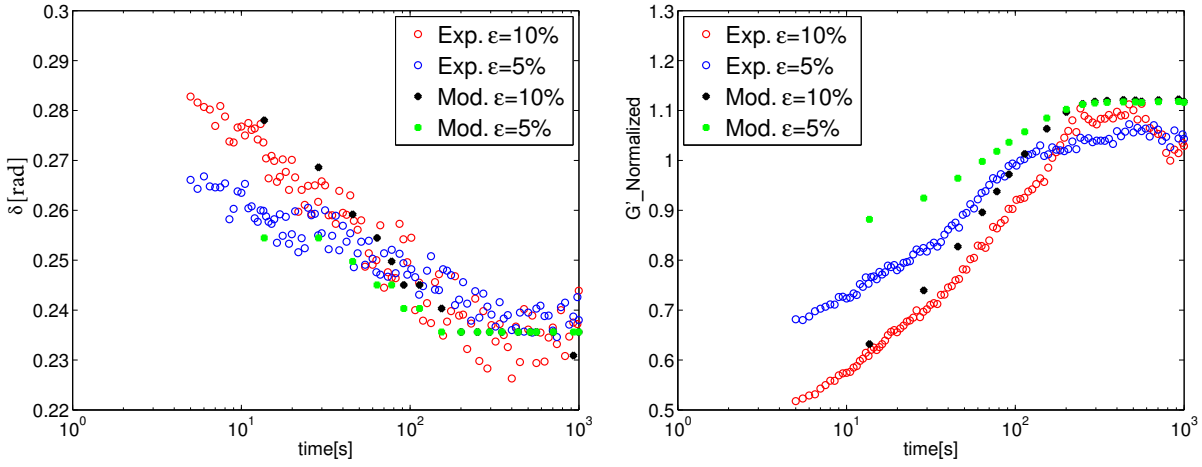

(a) (b)

Figure 4.11: The response of the multicellular system to a transient stretch of $\varepsilon = 10\%$ and $\varepsilon = 5\%$. Circles depict the experimental data, and circles represent our simulation of 10% and 5% of the strain, respectively. (a) Evolution of phase angle δ. (b) Evolution of stored modulus G'.

Chapter 5

Rheological model for cell relaxation

The cytoplasm is the largest part of the cell and hence its rheology sets the rate at which cellular shape changes can occur. Recent experimental evidence suggests that cytoplasmic rheology can be described by a poroelastic model, in which the cytoplasm is treated as a biphasic material consisting of a porous elastic solid meshwork (cytoskeleton, organelles, macromolecules) bathed in an interstitial fluid (cytosol), where the water redistribution through the solid phase of the cytoplasm (cytoskeleton and macromolecular crowders) plays a fundamental role in setting cellular rheology at short timescales [Moeendarbary et al., 2013].

In this chapter we introduce generalised Maxwell model and generalised active model in order to simulate the biphasic behaviour of cells undergoing stress relaxation that has been experimentally observed in bio-mechanical test performed by Guillaume Charras and his group at University College London. We explain this experimental work in the next section.

5.1 Experimental set-up

To investigate the mechanics of cells, a new device was developed [Harris et al., 2013], where MDCK cells are grown between two rods, one fixed and one flexible (see Figure 5.1). Then, MDCK cells were stretched at a strain rate $\dot{\varepsilon} = 30\%/s$ with a force transducer connected to a motorised manipulator. The force relaxation was monitored while cells are left stretched for 2.5 minutes.

Figure 5.2a shows the force relaxation for MDCK cells, with a rapid decay in the first 5 seconds followed by slower decay afterwards. In Figure 5.2b, we see that force relaxation clearly exhibited two separate regimes. They reported that the first phase observed in cellular force relaxation may correspond to poroelastic behaviour due to water redistribution in cytoplasm and the second phase is due to ATP dependent processes. Rheological models for tissues range from those that treat the cytoplasm as a single-phase material are not able to capture the

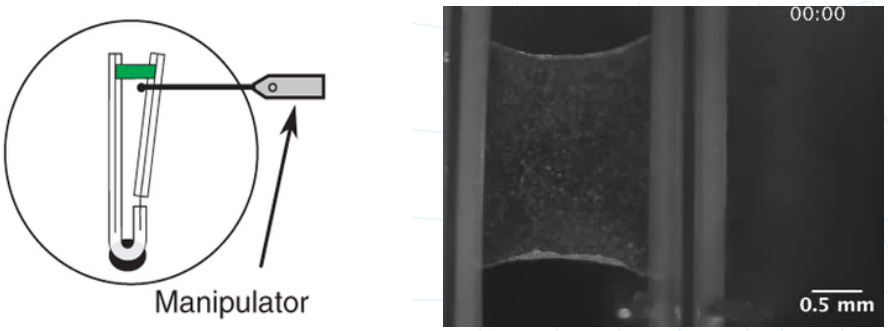

(a) (b)

Figure 5.1: (a) A profile view schematic of the device after application of a constant extension, showing the interaction of the manipulator with the rods adapted from [Harris et al., 2013]. (b) Image of MDCK cells between two rods.

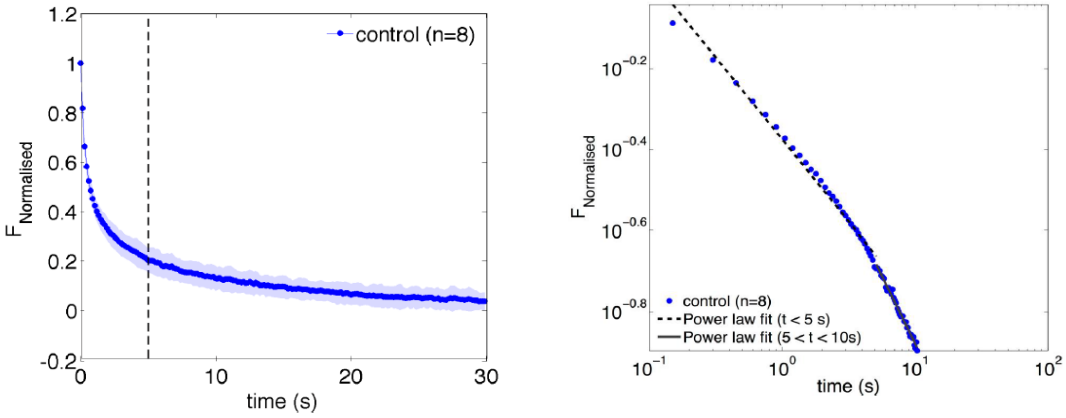

(a) (b)

Figure 5.2: (a) Representative force relaxation curve for MDCK cells. After the application of a 30% strain, the tissue relaxes to equilibrium in $\sim$ 10 second. (b) log-log scale of the plot in (a) showing the two regimes of force relaxation.

first phase observed in this experiment at short time scale. Therefore, we present a Generalised Maxwell and Generalised active models to simulate the biphasic behaviour of cells in this experiment.

5.2 Material fitting

The material parameters of the model, $\boldsymbol{p} = (p_1, p_2, ..., p_N)$, will be fitted by minimising the error of the numerical stress resultant σ with respect to the experimental values. More specifically, the following error function

$$E = \min_{\boldsymbol{p}} \sum_i (\sigma(\boldsymbol{p})_i - \sigma(exp)_i)^2, \tag{5.1}$$

is minimised using a least square procedure adapted from the Matlab function `lsqcurvefit`, and where $\sigma(exp)_i$ is the experimental stresses resultant at time t_i.

5.3 Constant strain test

5.3.1 Generalized Maxwell and Generalized active models (two branches)

Analytical solutions for the Maxwell and active model under a constant displacement is presented in Section 3.5.3. We here recast the resulting stress evolution in equations (3.37) and (3.38),

$$\sigma(t)_{Active} = k\frac{(L_1 - L_0)e^{-\gamma t}}{L_1 - (L_1 - L_0)e^{-\gamma t}} \tag{5.2}$$

$$\sigma(t)_{Maxwell} = \varepsilon_0 k e^{-\frac{k}{\eta}t}. \tag{5.3}$$

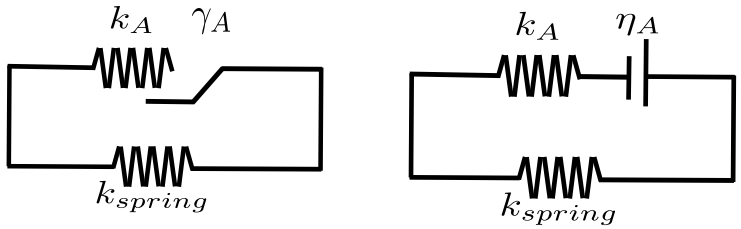

(a) (b)

Figure 5.3: (a) Active element connected to a spring in parallel. (b) Maxwell element connected to a spring in parallel.

In order to obtain the biphasic behaviour of cells during stress relaxation experiment described in the previous section, first, we test an active element connected to a spring in parallel (see Figure 5.3a). These models with two branches aim to represent the combined mechanical response of tissues, which exhibit an elastic behaviour at short time scales and a viscous component at longer time-scales [Wolff et al., 2012]. The total stress $\sigma_{tot,GA}$ of the Generalized active rheology will be the sum of the stress in active and elastic component and can be computed as,

$$\sigma_{tot,GA} = k_A\frac{(L_1 - L_0)e^{-\gamma_A t}}{L_1 - (L_1 - L_0)e^{-\gamma_A t}} + k_{spring}\varepsilon^e \tag{5.4}$$

The total stress $\sigma_{tot,GM}$ of the Generalized Maxwell rheology shown in Figure 5.3b will be the sum of the stress in Maxwell and elastic component and given by,

$$\sigma_{tot,GM} = \varepsilon_0 k e^{-\frac{k}{\eta}t} + k_{spring}\varepsilon^e. \tag{5.5}$$

In this test, a bar element is subjected to a stretch by 30% of the strain and then is left stretched approximately for 2.5 minutes. The total stress of the bar element is monitored after cessation the step strain.

Figure 5.4 shows the stress relaxation curve obtained from the experimental and numerical stresses. Figure 5.5 shows a logarithm plot of the total stress for 30 seconds. In this plot it is clear that the active rheological model with two branches is not able to simulate the first phase observed in stress relaxation experiment. The fitting of the material parameters (k_A, γ_A and k_{spring}) are not attempted in this experiment, since the two branches model can not capture changes of trend (see Figure 5.5). As we discussed in Section 3.5.3 Maxwell and active models have a similar trend in a stress relaxation test, so the Maxwell element connected to a spring in parallel of the Generalised Maxwell element was neither fitted in this case. Instead, the three branch model explained in the next Section was employed.

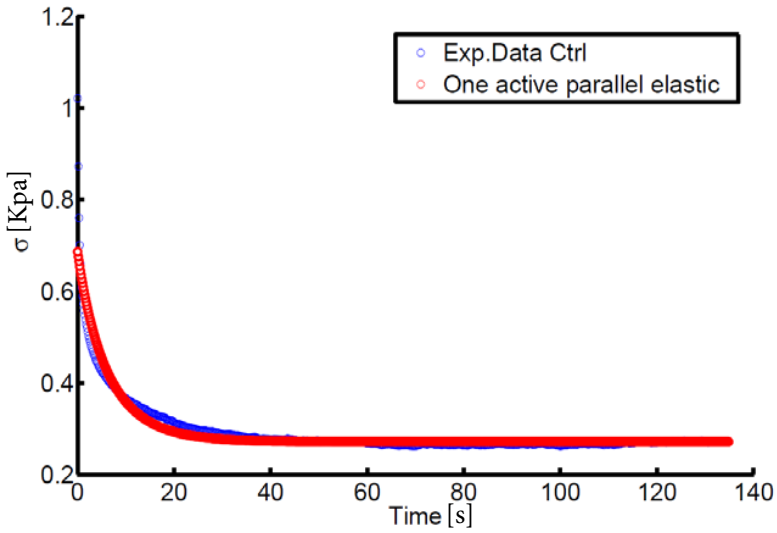

Figure 5.4: Stress relaxation curve for experimental and numerical stresses (kilopascal).

5.3.2 Generalized Maxwell and Generalized active models (three branches)

Here, in order to simulate the change of characteristic time in the experimental results, we test a Generalized Maxwell and a Generalized active models with three branches, where two Maxwell/active elements are connected to a spring in parallel. Figure 5.6 shows the Generalised Maxwell and Generalized active models with the three branches, and also indicates the material constants being employed. The total stress of this model will be the sum of the stresses in each

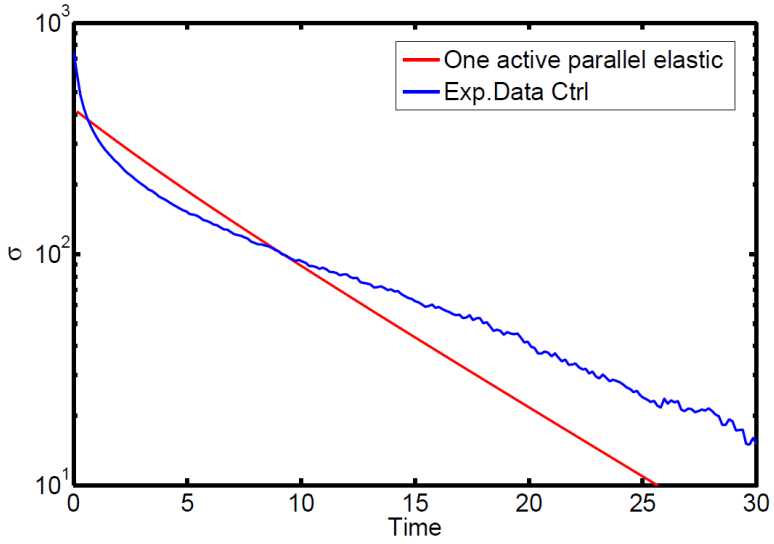

Figure 5.5: Logarithm σ (pascal) plot for the first 30 seconds.

Maxwell/active branch plus the elastic component of the spring component.

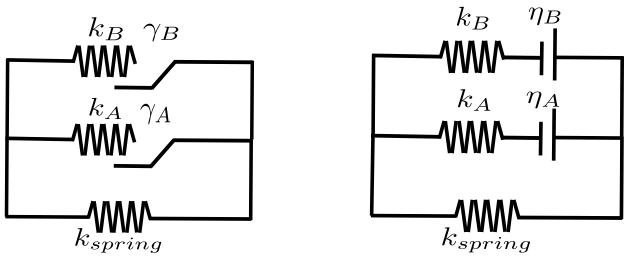

(a) (b)

Figure 5.6: (a) Generalized active model (three branches). (b) Generalized Maxwell model (three branches).

The same test is applied to a bar element with the rheology shown in Figure 5.6. Figure 5.7 shows the stress relaxation curve obtained by the experimental data, and the Generalized Maxwell and Generalized active models. It can be observed that the numerical results show a good agreements with experimental stresses. Figure 5.8 is the log-log plot of the stress relaxation, where the first phase of stress relaxation clearly captured by the Generalized Maxwell and Generalized active models with three branches.

As shown in Figure 5.7, the model predictions are used the fit values (k_{spring}, k_A,k_B,γ_A,γ_B)=(0.27, 0.97, 0.73, 0.98, 0.08) and (k_{spring}, k_A, k_B, η_A,η_B)=(0.29, 0.69, 0.78, 6.91, 0.76) for the Generalized active and Generalized Maxwell, respectively. The difference in the values of the two remodelling rates γ_A and γ_B, which is one order of magnitude approximately, or the different values of the vis-

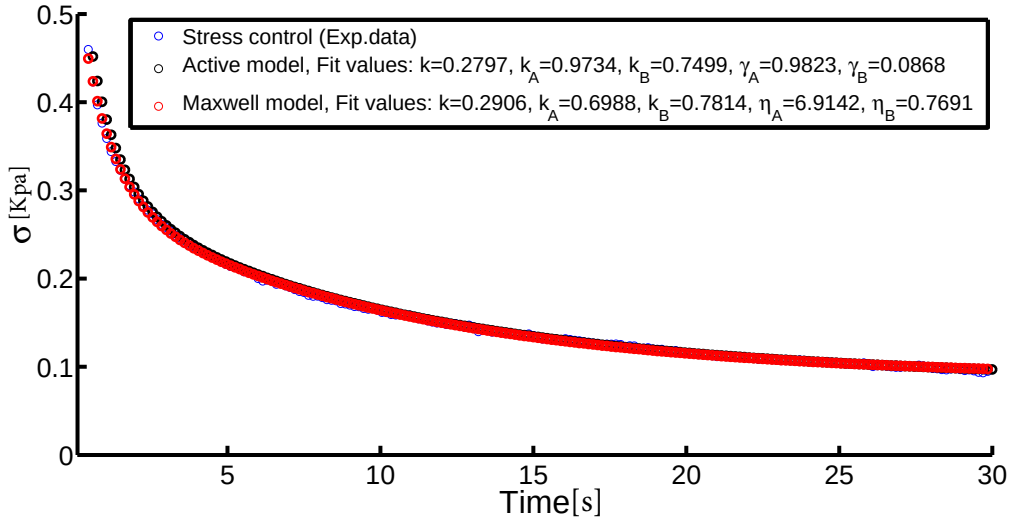

Figure 5.7: Stress relaxation curves obtained by experimental data and numerical results.

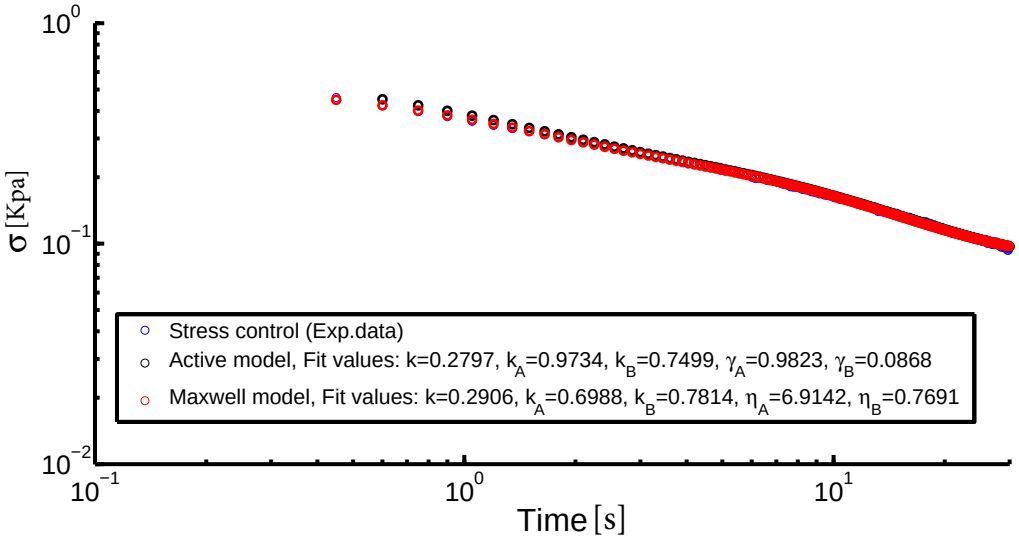

Figure 5.8: Log-log scale of stress relaxation plot.

cosity coefficient reflects the clear biphasic nature of the response. The specific physical sources of this change of characteristic time are as yet undetermined, but are clearly visible and can be quantified with the models.

5.3.3 Multicellular system

Here we aim to simulate the stress relaxation of MDCK cells described in Section 5.1 using a multicellular system. Figure 5.9 shows the tissue obtained from the MDCK cells image using a barycentric method (see Section 2.6).

In this simulation, first Generalized active model with three branches is ap-

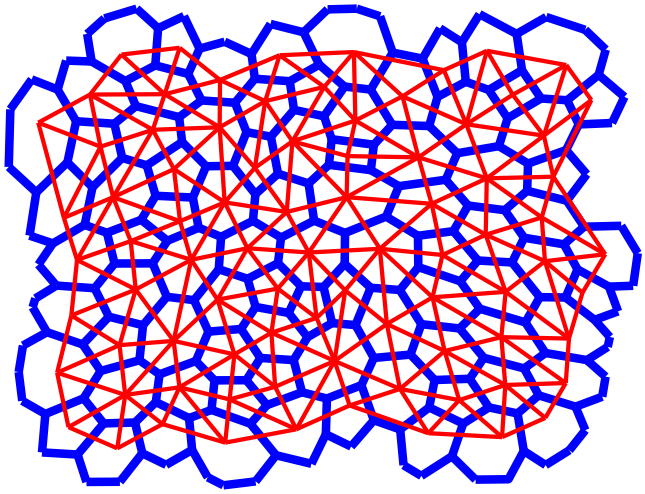

Figure 5.9: Multicellular system obtained from an MDCK phase contrast image. Thin lines represent cell-cell connectivity and thick lines the cells boundaries obtained from a barycentric method.

plied on each cell-cell connectivity (thin lines in Figure 5.9). The tissue is subjected to a stretch by 30% of the strain and then is left stretched approximately for 2.5 minutes, similarly to the test in the previous Section. The total stress of the tissue is monitored after cessation the step strain.

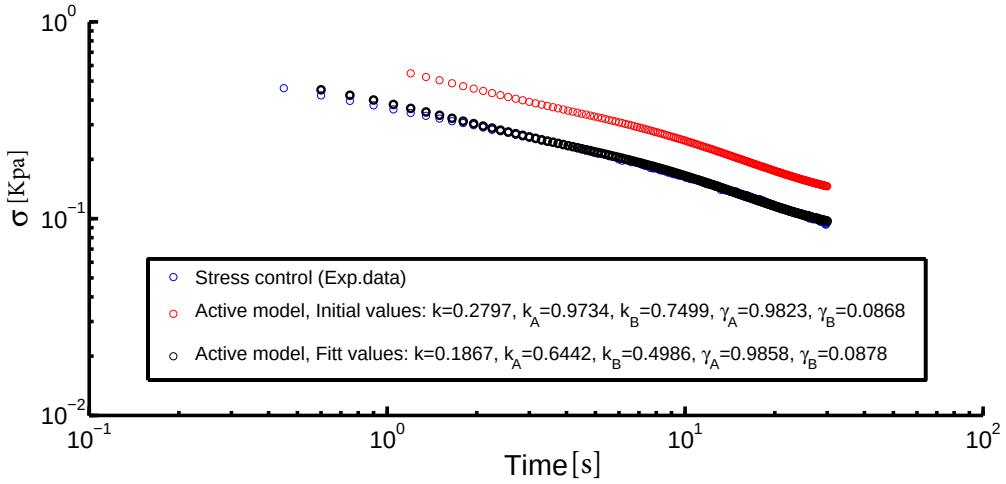

Figure 5.10: Stress relaxation curve for multicellular system. Red cycles are the numerical results obtained from a arbitrary set of material parameters. Black cycles are the numerical results after fitting material parameters with experimental data.

The stress relaxation curve using the set of material parameters $\boldsymbol{p}_0$ =(k_{spring},k_A,k_B, γ_A,γ_B)=(0.27, 0.97, 0.74, 0.98, 0.08) of the Generalized active model with three branches obtained for the one element test shown with red cycles in Figure 5.10.

After fitting the material parameters, the fit values (k_{spring}, k_A,k_B, γ_A,γ_B)=(0.18, 0.64,0.49, 0.98, 0.08) are used to predict the stress relaxation experimental data (see black cycles in Figure 5.10). Although the elastic constants of the branches differ, the remodelling rates in each branches are almost identical, and with the same difference of one order of magnitude. The distribution of the elastic forces on the network makes the stiffness coefficients k, k_A and k_A very dependent on the cell topology and sizes, as it is customary in cell-centred models [Hahn et al., 2010]. An homogenisation of the forces is required in order to remove this dependence. Importantly, the remodelling rates are independent of such topology, despite the resting length rates depend on the bar orientation with respect to the applied strain.

5.4 Incremental strain test

In order to test the differences on Maxwell and active rheological laws, we have compared the numerical and experimental results when the monolayer is subjected to a monotonically increasing strain, with a constant strain rate. Indeed, it is in this case that both models differ in their response. Although the results in this section are not conclusive, we include it for completeness reasons.

The analytical solution of Maxwell and active model under an increasing strain $\varepsilon(t) = \varepsilon_0 + at$ with a an arbitrary constant, is given by,

$$\sigma(t)_{Maxwell} = a\eta(1 - e^{-\frac{k}{\eta}t}) \tag{5.6}$$

$$\sigma(t)_{active} = k\left(\frac{l_0 + at}{l_0 + at + \frac{a}{\gamma}(e^{-\gamma t} - 1)} - 1\right). \tag{5.7}$$

In this test, the Generalized Maxwell and active models with three branches (see Figure 5.6) are applied to the bar element. Then, the bar element is subjected to an increasing strain up to the value $\varepsilon_{max} = 100\%$. The stresses-strain curve of both models are shown in Figure 5.11.

Figure 5.12 shows the evolution of the stresses for the MDCK cells under a continuous stretch obtained by Guillaume Charras and his group. When comparing the evolution of stresses in Figure 5.11 with the experimental stresses in Figure 5.12, the distinct trend of the stress evolution can be clearly observed. While the experimental curve undergoes a hardening process, the numerical models miss to simulate this process, in fact the general trends of the curves, with no delayed stiffening, are independent are independent of the material parameters. This fact has suggested a slight modification of the resting length evolution.

We will resort to the same active model with two branches, as shown in Figure 5.3a, but with the evolution law in (3.24) redefined as,

$$\dot{L} = \gamma(\varepsilon^e - \varepsilon_c), \tag{5.8}$$

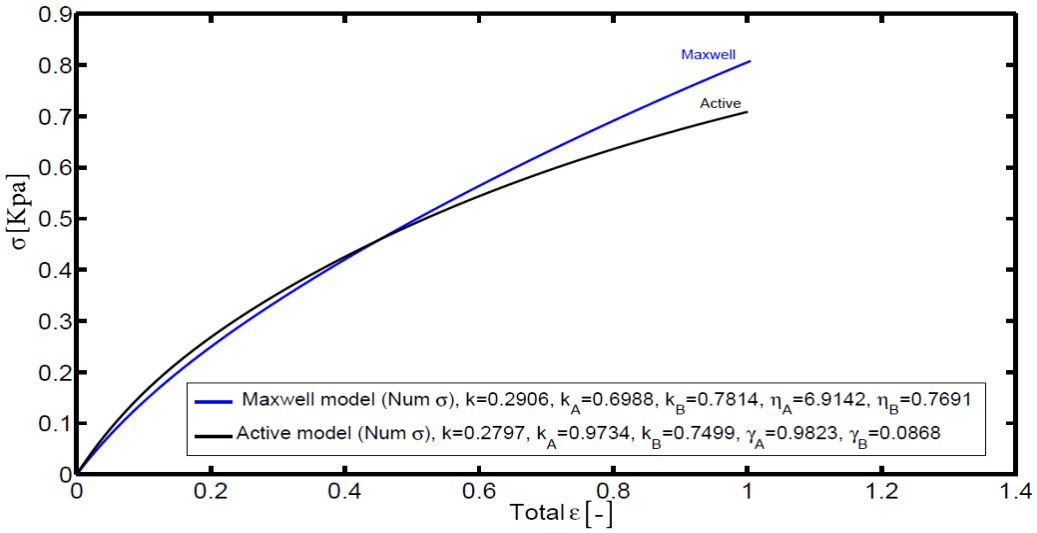

Figure 5.11: Response of the Generalized Maxwell model and Generalized active model with three branches under an increasing strain.

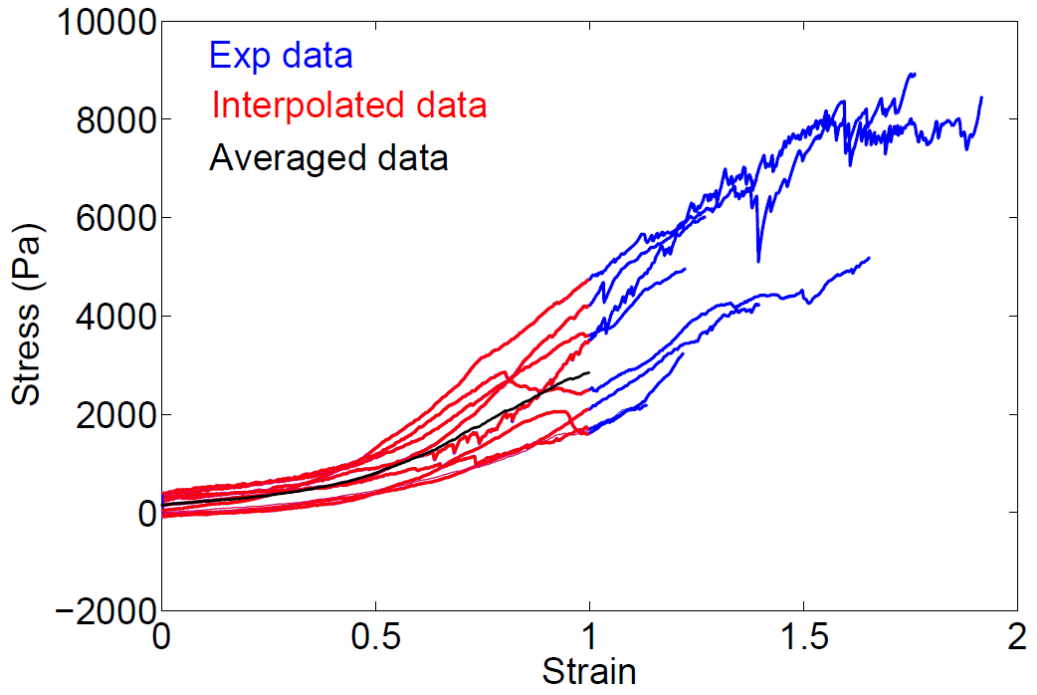

Figure 5.12: Stress-strain plot of the MDCK cells under a continuous stretching.

where ε_c is contractility strain that aim to mimic the contractile stress state of cells. This modification aims to reproduce the homoeostatic contractile stress that tissues exhibit, as the early retraction of cells demonstrate when tissues are subjected to a wound process [Brugués et al., 2014].

Also, we apply a quadratic elasticity on active branch as follows,

$$\sigma_{active} = k_A(\varepsilon^e)^2. \tag{5.9}$$

A bar element and a 10 by 10 Cartesian mesh are tested with the modifications explained above, and subjected to a continuous stretch. Their mechanical response is characterised by the stress evolution shown in Figure 5.13. This figure and the evolution of the experimental stress in Figure 5.12 have the same trend, but are quantitatively different, since magnitudes and slopes differ for different strain values. In summary, by adding a contractility strain constant to the active evolution law and using a quadratic elasticity, the hardening observed in experimental data is qualitatively recovered.

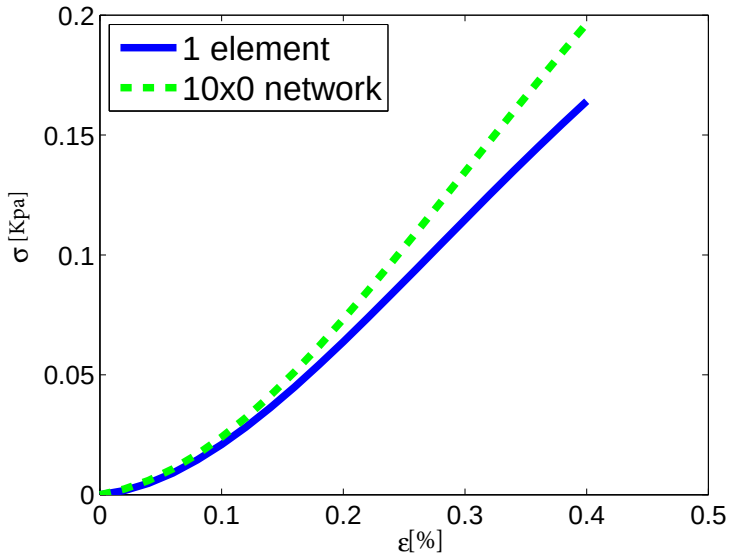

Figure 5.13: Evolution of the stress for a bar element and a 10 by 10 Cartesian mesh.

We point out that this early hardening of the numerical results is lost whenever no contractility is applied or no quadratic stress is employed. Interestingly, the coupling between hardening and contractility has already been previously established in adherent cells [Wang et al., 2002]. We finally remark that in order to fit the actual experimental curves, which show a significant degree of variability (see Figure 5.12), strain dependent contractility factors and more sophisticated elastic potentials seem to be required.

Chapter 6

Concluding remarks and future work

6.1 Conclusions

This thesis is motivated by the non-linear response of biological tissues, which exhibit softening and fluidisation process [Trepat et al., 2007, Wolff et al., 2012]. In order to include this response, and at the same time model the tissue by explicitly representing the individual cells, a cell-centred model has been developed which can include any arbitrary rheological law while undergoing large deformations and rotations.

The cell-centred model is based on Delaunay representations and suitable tessellations of the domain, which represent the cell regions. Such triangulation and tessellation employ modified Delauany and Voronoi algorithms, which are applied in a staggered manner with respect to the equilibrium equations. This two-step process has consequences on the tessellation, which is modified due to the equilibrium conditions, and thus may not fully comply with the definition of the Voronoi algorithm. For this reason, an alternative barycentric interpolation has been tested.

The cell rheology proposed here adapts classical viscoelastic laws, which is implemented in one-dimensional bars that form the cellular tissue. In order to extend these linear viscoelastic laws to the non-linear case, an alternative implementation based on null space projection and static condensation is presented. These extension allows us to test elastic softening and non-linear viscosity. Although the response of this modified rheology shows similar trends than the experimental results [Trepat et al., 2007], the time scale of the response is much shorter in the numerical models. This mismatch has motivated the porous based model presented in Chapter 4. Despite this pitfall, the methodology has been presented because it can handle arbitrary combinations of non-linear elastic an viscous laws.

This thesis also presents a viscoelastic law that is based on an evolution law of the resting length. It has been shown that this alternative phenomenological interpretation gives very similar results to the classical Maxwell model. In order to capture the delayed recovery of the mechanical properties of the tissue in the fluidisation experiments, this resting length evolution has been extending with a new porosity variable, which modulates the cell stiffness and that also has associated an unsymmetrical evolution law.

The rheological laws are also used to match the laboratory results of strained suspended monolayers. The experimental results required to implement multiple branches for the Delaunay network, and fit the multiple parameters. Although this fitting and the tests with different cultivating conditions are still an ongoing work, the promising results obtained so far are encouraging for testing these different conditions, and further extending the mechanics to the Voronoi network.

6.2 Future work

The methodology for handling cell-cell remodelling has been briefly explained in this thesis. The numerical tests carried out though do not numerically analyse this methodology. Nonetheless, some examples can be found in [Mosaffa et al., 2015] where it is shown that the remodelling phenomena further adds a plastic like behaviour to the monolayers. Also, the stability and robustness of the barycentric and Voronoi tessellation needs to be analysed in a more detailed manner when this remodelling takes place. Some work on smoothing this cell-cell contact transitions are being investigated. Although the barycentric interpolation seems so far better suited for visualising the cells, and therefore transferring mechanics to the cell boundaries, this fact should be further tested in the future with more examples.

The theory presented here is also valid for three-dimensional analysis. However, this case needs to be further tested, overall when remodelling takes place, and with the rheological models proposed here. In addition, the differences between the Maxwell and the active length model needs to be experimentally contrasted and verified with further experimental tests.

The experimental results of the stress relaxation tests in Chapter 5 reveal that monolayers behave in a non-linear manner, and that they respond with different phases. The linear evolution law of the resting law, and the simple elastic potential employed showed similar stiffening profiles, but with different timescales. This mismatch motivates the design of more sophisticated evolution laws and rheological models where the contributions of fluid and different polymeric constituents are explicitly coupled.

6.3 List of publications and conference presentations

As a result of this thesis, the following articles have been published.

- Mosaffa P., Asadipour N., Millán D., Rodríguez-Ferran A., Muñoz J J. **Cell-centred model for the simulation of curved cellular monolayers**. *Comp. Particle Mechanics.*, 2(4):359-370, 2015.

- Muñoz J J., Conte V., Asadipour N., Miodownik M. **On the modelling of reversible softening in tissues with truss elements**. *Mech. Res. Comm.*, 49:44-49, 2013.

The following article has been submitted.

- Asadipour N., Trepat X., Muñoz J J. **Porous-based rheological model for tissue fluidisation**. *J. Mech. Phys. Solids*, submitted.

The following works have been presented at international conferences.

1. Mosaffa P., Asadipour N., Millán D., Rodríguez-Ferran A., Muñoz J J. **Cell-centred model for the simulation of curved cellular monolayers**. IV International Conference on Particle-Based Methods (Particles), 28-30 Septembre 2015. Barcelona, Spain.

2. Muñoz J J., Mosaffa P., Asadipour N., Millán D., Rodríguez-Ferran A. **Hybrid Cell-Centred / Vertex Model for Three-Dimensional Monolayers**. IV International Conference in Computational Bioengineering (ICCB), 14-16 Septembre 2015. Barcelona, Spain.

3. Asadipour N., Muñoz J J. **Rheological model for cell fluidisation process**. II International Conference on Computational Plasticity (COMPLAS), 1-3 Septembre 2015. Barcelona, Spain.

4. Mosaffa P., Asadipour N., Millán D., Rodríguez-Ferran A., Muñoz J J. **Cell-centred model for the simulation of curved cellular monolayers**. XII International Conference on Computational Plasticity (COMPLAS), 1-3 Septembre 2015. Barcelona, Spain.

5. Mosaffa P., Asadipour N., Millán D., Rodríguez-Ferran A., Muñoz J J. **Hybrid cell centred/Vertex model for Cellular Monolayers**. Computational and Mathematical Biomedical Engineering (CMBE), 29 Juny - 1 Juliol 2015, Cachan, France.

6. Asadipour N., Mosaffa P., Muñoz J J. **Cell-centred model for nonlinear tissue rheology and active remodelling**. 11th World Congress on Comp. Mechanics (WCCM), 20-25 July 2014, Barcelona, Spain.

7. Muñoz J J., Albo S., Conte V., Asadipour N. **Predictive model for cell softening and hardening**. 5th International Conference on Mechanics of Biomaterials and Tissues (ICMOBT), 5-12 December 2013, Sitges, Spain.

8. Asadipour N., Albo S., Muñoz J J. **Cell-centred truss model for the analysis of cell rheology and remodelling**. COMPLAS XI, 3-5 September 2013, Barcelona, Spain.

9. Muñoz J J., Asadipour N., Albo S. **Cell activity versus cell viscoelasticity**. MetNum 2013, 25-28 June 2013, Bilbao, Spain.

10. Asadipour N., Conte V., Muñoz J J. **Computational model for active cell mechanics** . Quantissue, 10-11 April 2013, Barcelona, Spain.

Appendix A

Proof of the uniqueness of active length tensor $\mathbf{L}^i$

We will here proof that the solution of the system of equations in (3.28) at a given node i is unique if the vectors $\boldsymbol{n}_j$ that define the cell-cell connectivities at node i and that form matrix $\mathbf{A}$ span $\mathbb{R}^{n_{sd}}$.

By definition, matrix $\mathbf{A}$ is semi-positive definite (SPD) and symmetric. We will here proof that matrix $\mathbf{A}$ is in fact positive definite (PS), and hence gives a unique solution. Matrix $\mathbf{A}$ is PS if the following implication holds:

$$\bar{\mathbf{L}}^{iT}\mathbf{A}\bar{\mathbf{L}}^i = 0 \Rightarrow \bar{\mathbf{L}}^i = 0 \tag{A.1}$$

But, by setting $\boldsymbol{l}^{ij} = \mathbf{L}^i\boldsymbol{n}_j$, we have that,

$$\bar{\mathbf{L}}^{iT}\mathbf{A}\bar{\mathbf{L}}^i = \sum_{j=1}^{n} \mathbf{L}^i\boldsymbol{n}_j \cdot \mathbf{L}^i\boldsymbol{n}_j = \sum_{j=1}^{n} ||\boldsymbol{l}^{ij}||^2$$

So,

$$\sum_{j=1}^{n} \mathbf{L}^i\boldsymbol{n}_j \cdot \mathbf{L}^i\boldsymbol{n}_j = 0 \Rightarrow \boldsymbol{l}^{ij} = \mathbf{0}, \forall j \tag{A.2}$$

i.e., implication in (A.1) may be also expressed as,

$$\sum_{j=1}^{n} \mathbf{L}^i\boldsymbol{n}_j \cdot \mathbf{L}^i\boldsymbol{n}_j = 0 \Rightarrow \mathbf{L}^i\boldsymbol{n}_j \cdot \boldsymbol{e}_k = 0, \forall j, k.$$

Setting $\boldsymbol{n}_j = \alpha_j^l \boldsymbol{e}_l$ we have that,

$$\mathbf{L}^i\boldsymbol{n}_j \cdot \boldsymbol{e}_k = \alpha_j^l \mathbf{L}^i\boldsymbol{e}_l \cdot \boldsymbol{e}_k = \sum_l \alpha_j^l L_{kl}^i$$

with $L_{kl}^i = \mathbf{L}^i\boldsymbol{e}_l \cdot \boldsymbol{e}_k$ component kl of tensor $\mathbf{L}^i$. Therefore, equation (A.2) is equivalent to,

$$\sum_l \alpha_j^l L_{kl}^i = 0, \forall k, j.$$

By denoting by $\mathbf{L}^i_k$ the k-th row of the tensor $\mathbf{L}^i$, this condition may be also expressed as,

$$\boldsymbol{n}_j \cdot \mathbf{L}^i_k = 0, \forall k, j,$$

that is, the vectors $\boldsymbol{n}_j$ are orthogonal to each one of the rows of $\mathbf{L}^i$. If the vectors $\boldsymbol{n}_j$ span the whole space $\mathbb{R}^{n_{sd}}$, this is only possible when $\mathbf{L}^i_k = 0$, as we wanted to proof.

Appendix B

Proof of the uniqueness of nodal stresses $\hat{\boldsymbol{\sigma}}$

In Section 3.4, it is shown that the unknown stress $\hat{\boldsymbol{\sigma}}$ is defined by minimization of the stress error E, which gives,

$$\boldsymbol{A}\hat{\boldsymbol{\sigma}} = \boldsymbol{b}$$

with

$$\boldsymbol{A} = \sum_j \boldsymbol{N}_j^T \boldsymbol{N}_j$$
$$\boldsymbol{b} = 2\sum_{i=1}^{n} \boldsymbol{N}^{i^T} \boldsymbol{t}^i$$

By definition, vector A is semi positive definite. Therefore, the uniqueness of the solution is equivalent to the following condition,

$$\boldsymbol{\sigma}^T \boldsymbol{A}\boldsymbol{\sigma} = \sum_j \boldsymbol{\sigma}\boldsymbol{n}_j.\boldsymbol{\sigma}\boldsymbol{n}_j = 0 \Rightarrow \boldsymbol{\sigma} = 0 \tag{B.1}$$

where,

$$\sum_j \boldsymbol{\sigma} n_j.\boldsymbol{\sigma}\boldsymbol{n}_j = \sum_j ||\boldsymbol{t}_j||^2. \tag{B.2}$$

$$\boldsymbol{\sigma}^T \boldsymbol{A}\boldsymbol{\sigma} = 0 \Rightarrow \boldsymbol{t}_j = 0, \forall j \tag{B.3}$$

i.e., condition B.1 implies that,

$$\boldsymbol{t}_j \cdot \boldsymbol{e}_i = 0, \forall i, j. \tag{B.4}$$

Setting $\boldsymbol{n}_j = \alpha_j^k \boldsymbol{e}_k$ we have that,

$$\boldsymbol{t}_j \cdot \boldsymbol{e}_i = \alpha_j^k \boldsymbol{\sigma} e_k.e_i = \sum_k \alpha_j^k \boldsymbol{\sigma}_{ik} \tag{B.5}$$

Therefore, equation (B.3) is equivalent to,

$$\sum_k \alpha_j^k \boldsymbol{\sigma}_{ik} = 0, \forall i, j. \tag{B.6}$$

By denoting $\boldsymbol{\sigma}_i$ the $i-th$ column of the tensor $\boldsymbol{\sigma}$, this condition may be also expressed as,

$$\boldsymbol{n}_j \boldsymbol{\sigma}_j = 0, \forall j, \tag{B.7}$$

that is, the vectors $\boldsymbol{n}_j$ are orthogonal to each one of the columns of $\boldsymbol{\sigma}$. If the vectors $\boldsymbol{n}_j$ span the whole space $\mathbb{R}^d$, this is only possible when $\boldsymbol{\sigma}_i = 0$, as we wanted to proof.

Bibliography

"B Aigouy, R Farhadifar, D B Staple, A Sagner, J C Röper, F Jülicher, and S Eaton". Cell flow reorients the axis of planar polarity in the wing epithelium of drosophila. *Cell*, 142(5):773–786, 2010.

H Altenbach, G Maugin, and V Erofeev. *Mechanics of generalized continua*. Advanced Structured Materials. Springer-Verlag, Berlin, 1st edition, 2011.

D Azevedo, M Antunes, S Prag, X Ma, U Hacker, GW Brodland, M S Hutson, J Solon, and A Jacinto. DRhoGEF2 Regulates Cellular Tension and Cell Pulsations in the Amnioserosa during Drosophila Dorsal Closure. *PLOS ONE*, 6(9):e23964, 2011.

CB Barber, DP Dobkin, and H.T. HT Huhdanpaa. The Quickhull algorithm for convex hulls. *ACM Trans. Math.. Soft.*, 22(4):469–483, 1996. http://www.qhull.org.

T Belytschko, W K Liu, and Brian Moran. *Nonlinear Finite Elements for Continua and Structures*. Wiley and Sons, 2000.

P Betsch. The discrete null space method for the energy consistent integration of constrained mechanical systems. Part I: Holonomic constraints. *Comp. Meth. Appl. Mech. Engng.*, 194:5159–5190, 2005.

J Bonet. Large strain viscoelastic constitutive models. *Int. J. Solids Struct.*, 38 (17):2953–2968, 2001.

A Brugués, E Anon, V Conte, JH Veldhuis, M Gupta, J Collombelli, JJ Muñoz, GW Brodland, B Ladoux, and X Trepat. Forces driving epithelial wound healing. *Nature Physics*, 10:683–690, 2014.

B Calvo, E Peña, M A Martinez, and M Doblaré. An uncoupled directional damage model for fibred biological soft tissues. formulation and computational aspects. *Comm. Num. Meth. Engng.*, 7(9), 2011.

O Chaudhuri, SH Parekh, and DA Fletcher. Reversible stress softening of actin networks. *Nature*, 445:295–298, 2007.

C Chen, R Krishnan, E Zhou, A Ramachandran, D Tambe, K Rajendran, R M Adam, L Deng, and J J Fredberg. Fluidization and Resolidification of the

Human Bladder Smooth Muscle Cell in Response to Transient Stretch. *PLOS ONE*, 5:16–21, 2010.

M Costa, D Sweeton, and E Wieschaus. *The development of drosophila melanogaster. Chapter 8: Gastrulation in drosophila: cellular mechanisms of morphogenetic movements*. Cold Spring Laboratory Press, 1993.

B N Cox and D W Smith. On strain and stress in living cells. *J. Mech. Phys. Solids.*, 71(14):239–252, 2014.

C J Cyron and W A Wall. Consistent finite-element approach to Brownian polymer dynamics with anisotropic friction. *Phys. Rev. E*, 82(066705), 2010.

M. de Buhan and P Frey. A generalized model of non-linear viscoelasticity: numerical issues and applications. *Int. J. Num. Meth. Engng.*, 86:1544–1557, 2011.

D Drasdo and S Holme. A single-cell-based model of tumor growth in vitro: monolayers and spheroids. *J. Pathology. Bacteriology.*, 2:133–47, 2005.

G Eaves. The invasive growth of malignant tumours as a purely mechanical process. *J. Pathology.*, 109, March 1973.

H Edelsbrunner, D G Kirkpatrick, and R Seidel. On the shape of a set of points in the plane. *IEEE Transactions on Information Theory*, 29(4):551–559, 1983.

J Escribano, M T Sánchez, and J M García-Aznar. A discrete approach for modeling cell-matrix adhesions. *Comp. Part. Mech.*, 1:117–130, 2014.

G E Fantner, E Oroudjev, L S Golde, G Schitter, P Thurner, M M Finch, P Turner, T Gutsmann, D E Morse, H Hansma, and P K Hansma. Sacrificial bonds and hidden length: Unraveling molecular mesostructures in tough materials. *Bioph. J.*, 90(4):1411–1418, 2006.

P Fernández and A Ott. Single cell mechanics: stress stiffening and kinematic hardening. *Phys. Rev. Letters*, 100:238102, 2008.

P Fernández, p A Pullarkat, and A Ott. A master relation defines the nonlinear viscoelasticity of single fibroblasts. *Bioph. J.*, 90:3796–3805, 2006.

W N Findley, K Onaran, and W J Lai. *Creep and Relaxation of Nonlinear Viscoelastic Materials: With an Introduction to Linear Viscoelasticity*. Dover Publications, 1989.

Y C Fung. *Biomechanics : mechanical properties of living tissues*. Springer, New York, 2nd edition, 1993.

M L Gardel, J H Shin, F C MacKintosh, L Mahadevan, P Matsudaira, and D A Weitz. Elastic behavior of cross-linked and bundled actin networks. *Science*, 304:1301–1305, 2004.

M Hahn, T Wallmersperger, and B H Kröplin. Discrete element representation of continua: Proof of concept and determination of the material parameters. *Comp. Mat. Sc.*, 50:391–402, 2010.

A R Harris, J Bellis, N Khalilgharibi, T Wyatt, B Baum, A J Kabla, and G T Charras. Generating suspended cell monolayers for mechanobiological studies. *Nature*, 8:2516–2530, 2013.

G Helmlinger, P A. Netti, H C Lichtenbeld, R J Melder, and R K Jain. Solid stress inhibits the growth of multicellular tumor spheroids. *Nature*, 15:778–783, 1997.

G A Holzapfel. *Nonlinear solid mechanics. A continuum approach for engineers.* J Wiley & Sons Ltd, Chichester., 2000.

G A Holzapfel and T C Gasser. A viscoelastic model for fiber-reinforced composites at finite strains: continuum basis, computational aspects and applications. *Comp. Meth. Appl. Mech. Engng.*, 190:4379–4403, 2001.

H Honda, M Tanemura, and T Nagai. A three- dimensional vertex dynamics cell model of space-filling polyhedra simulating cell behavior in a cell aggregate. *J. Theor. Biol.*, 226:439–453, 2004.

TJR Hughes and RL Taylor. Unconditionally stable algorithms for quasi-static elasto/viscoplastic finite element analysis. *Comput. Struct.*, 8:169–173, 1978.

E Isaacson and H B Keller. *Analysis of numerical methods.* Dover publications, Inc, 1966.

C E Jamison, R D Marangoni, and A A Glaser. Viscoelastic properties of soft tissue by discrete model characterization. *J. Biomechanics*, 1:33–36, 1968.

T Kim, W Hwang, H Lee, and R D Kamm. Computational analysis of viscoelastic properties of crosslinked actin networks. *PLOS Comp. Biol.*, 5(7):1–13, 2009.

P Kollmannsberger and B Fabry. Active soft glassy rheology of adherent cells. *Soft Matter*, 5:1771–1774, 2009.

R Krishnan, C Y Park, Y C Lin, J Mead, R T Jaspers, X Trepat, G Lenormand, D Tambe, A V Smolensky, A H Knoll, J P Butler, and J J Fredberg. Reinforcement versus fluidization in cytoskeletal mechanoresponsiveness. *PLOS ONE*, 4:e5486, 2009.

T Lecuit and P F Lenne. Cell surface mechanics and the control of cell shape, tissue patterns and morphogenesis. *Nature Reviews*, 8:633–644, 2007.

M Leptin and B Grunewald. Cell shape changes during gastrulation in *Drosophila*. *Development*, 110:72–84, 1990.

O Lieleg, KM Schmoller, CJ Cyron, Y Luan, WA Wall, and AR Bausch. Structural polymorphism in heterogeneous cytoskeletal networks. *Soft Matter*, 5: 1796–1803, 2009.

J Lubliner. *Plasticity theory*. Dover Publ., 3rd edition, 2008. Dover edit. Mcmillan ed. in 1990.

X Ma, H E Lynch, P C Scully, and M S Hutson. Probing embryonic tissue mechanics with laser hole drilling. *PB*, 6:036004, 2009.

P Macklin, M E Edgerton, J S Lowengrub, and V Cristini. *Multiscale Modeling of Cancer*. Cambridge University Press, Cambridge, England, 2010.

A Malandrino, J Noailly, and D Lacroix. The effect of sustained compression on oxygen metabolic transport in the intervertebral disc decreases with degenerative changes. *PLOS Comp. Biol.*, 7(8), 2011.

JE Marsden and TJR Hughes. *Mathematical foundations of elasticity*. Dover Publications, 1994.

R M H Merks and J A Glazier. A cell-centered approach to developmental biology. *Physica A: Stat. Mech. Appl.*, 352(6):113–130, 2005.

GR Mirams, C J Arthurs, M O Bernabeu, R Bordas, J Cooper, A Corrias, Y Davit, S J Dunn, A G Fletcher, D G Harvey, M E Marsh, J M Osborne, P Pathmanathan, J Pitt-Francis, J Southern, N Zemzemi, and D J Gavaghan. Chaste: An open source c++ library for computational physiology and biology. *PLOS Comp. Biol.*, 9(3):e1002970, 2013.

E Moeendarbary, Léo Valon, M Fritzsche, AR Harris, DA Moulding, AJ Thrasher, E Stride, L Mahadevan, and GT Charras. The cytoplasm of living cells behaves as a poroelastic material. *Nature*, 12:253–261, 2013.

P Mosaffa, N Asadipour, D Millán, A Rodríguez-Ferran, and J J Muñoz. Cell-centred model for the simulation of curved cellular monolayers. *Comp. Part. Mech.*, 2(4):359–370, 2015.

J J Muñoz and S Albo. Physiology-based model of cell viscoelasticity. *Phys. Rev. E*, 88(1):012708, 2013.

J J Muñoz and G Jelenić. Sliding contact conditions using the master–slave approach with application on the geometracally non-linear beams. *Int. J. Solids Struct.*, 41:6963–6992, 2004.

J J Muñoz, K Barrett, and M Miodownik. A deformation gradient decomposition method for the analysis of the mechanics of morphogenesis. *J. Biomechanics*, pages 1372–1380, 2007.

J J Muñoz, V Conte, N Asadipour, and M Miodownik. On the modelling of reversible softening in tissues with truss elements. *Mech. Res. Comm.*, 49: 44–49, 2013.

T Nagai and H Honda. A dynamic cell model for the formation of epithelial tissues. *Phil. Mag. Part B*, 81:699–719, 2001.

A Okabe, B Boots, and K Sugihara. Spatial tessellations: concepts and applications of voronoi diagrams. *Wiley New York*, 1992.

S Okuda, Y Inoue, M Eiraku, Y Sasai, and T Adachi. Modeling cell proliferation for simulating three-dimensional tissue morphogenesis based on a reversible network reconnection framework. *Biomech. Model. Mechanobiol.*, 12:987–996, 2013.

J M Osborne, A Walter, S K S K Kershaw, G R Mirams, A G Fletcher, P Pathmanathan, D Gavaghan, O E Jensen, P K Maini, and H M Byrne. A hybrid approach to multi-scale modeling of cancer. *Phil. Trans. Royal Soc. London A*, 368:5013–5028, 2010.

P Pathmanathan, J Cooper, A Fletcher, G Mirams, P Murray, J Osborne, J Pitt-Francis, A Walter, and S J Chapman. A computational study of discrete mechanical tissue models. *J. Pathology. Bacteriology.*, 6:036001, 2009.

E Peña. Damage functions of the internal variables for soft biological fibred tissues. *Mech. Res. Comm.*, 38:610–615, 2011a.

E Peña. Prediction of the softening and damage effects with permanent set in fibrous biological materials. *Eur. J. Mech. A/Solids*, 59(9):1808–1822, 2011b.

M A Puso and J A Weiss. Finite element implementation of anisotropic quasi-linear viscoelasticity using a discrete spectrum approximation. *J. Biomech. Engin.*, 120:62–70, 1998.

H J Qi and MC Boyce. Constitutive model for stretch-induced softening of the stress-stretch behavior of elastomeric materials. *J. Mech. Phys. Solids.*, 52 (10):2187–2205, 2004.

A Ramasubramanian and L A Taber. Computational modeling of morphogenesis regulated by mechanical feedback. *Biomech. Model. Mechanobiol.*, 7:77–91, 2008.

J Ranft, M Basan, J Elgeti, JF Joanny, J Prost, and F Jülicher. Fluidization of tissues by cell division and apoptosis. *Proc. Nat. Acad. Sci. USA*, 107(49): 20863–8, 2008.

C Semmrich, T Storz, J Glaser, R Merkel, A R Bausch, and K Kroy. Glass transition and rheological redundancy in F-actin solutions. *Proc. Nat. Acad. Sci. USA*, 104(51):20199–20203, 2007.

C Semmrich, R J Larsen, and A R Bausch. Nonlinear mechanics of entangled F-actin solutions. *Soft Matter*, 4:1675–1680, 2008.

J C Simo. On a fully three-dimensional finite-strain viscoelastic damage model: Formulation and computational aspects. *Comp. Meth. Appl. Mech. Engng.*, 60:153–173, 1987.

P Spahn and R Reuter. A vertex model of Drosophila ventral furrow formation. *PLOS ONE*, 8(9):e75051, 2013.

C Storm, JJ Pastore, F C MacKintosh, TC Lubensky, and PA Janmey. Nonlinear elasticity in biological gels. *Nature*, 435:191–194, 2005.

X Trepat, L Deng, SS An, D Navajas, DJ Tschumperlin, WT Gerthoffer, JP Butler, and JJ Fredberg. Universal physical responses to stretch in the living cell. *Nature*, 447(3):592–596, 2007.

X Trepat, MR Wasserman, TE Angelini, E Millet, DA Weitz, JP Butler, and JJ Fredberg. Physical forces during collective cell migration. *Nature Physics*, 5(3):426–430, 2009.

KC Valanis. *Irreversible thermodynamics of continuous media, Internal variable theory*, volume 77 of *CISM Courses and Lectures*. Springer-Verlag, Internatinal center for mechanical sciences, Wien, 1972.

V Vogel and M Sheetz. Local force and geometry sensing regulate cell functions. *Nature Reviews Mol. Cell Biol.*, 7:265–275, 2006.

N Wang, I Tolic-Norrelykke, J Chen, SM Mijailovich, and JP Butler. Cell prestress. I. Stiffness and prestress are closely associated in adherent contractile cells. *American Journal of Cell Physiology*, 282:606–616, 2002.

X Wang and W Hong. A visco-poroelastic theory for polymeric gels. *Proc. Royal Soc. London*, 486:3824–3841, 2012.

E W Weisstein. Inradius. *MathWorld*, 2016a. http://mathworld.wolfram.com/Inradius.html.

E W Weisstein. circumradius. *MathWorld*, 2016b. http://mathworld.wolfram.com/Circumradius.html.

L Wolff, P Fernández, and K Kroy. Resolving the Stiffening-Softening Paradox in Cell Mechanics. *PLOS ONE*, 7(7):e40063, 2012.

J Xu, Y Tseng, and D Wirtz. Strain hardening of actin filament networks. regulation by the dynamic cross-linking protein alpha-actinin. *J. Biol. Chem.*, 275:35886–35892, 2000.

M Yang and L A Taber. The possible role of poroelasticity in the apparent viscoelastic behavior of passive cardiac muscle. *J. Biomechanics*, 24(7):587–597, 1991.

J S Young. The invasive growth of malignant tumours: An experimental interpretation based on elastic-jelly models. *J. Pathology. Bacteriology.*, pages 321–339, 1959.

O C Zienkiewicz. *Computational Mechanics, Ed: J T Oden*, chapter Viscoplasticity, plasticity, creep and viscoplastic flow (problems of small, large and continuing deformation). TICOM Lecture Notes on Matehmatics, 461. Springer-Verlag, Heidelberg, 1975.